Millimeter Interferometric Polarimetry of Magnetic Field Structure in Protostellar Condensations

Thesis by

Rachel L. Akeson

In Partial Fulfillment of the Requirements
for the Degree of
Doctor of Philosophy

California Institute of Technology
Pasadena, California

1997
(Submitted July 19, 1996)

Acknowledgements

The implementation of polarization observing at OVRO would not have been possible without David Woody who designed the polarimeters and supervised the production. In addition to the entire OVRO staff, the efforts of Steve Scott (observing software), Tony Phillips (gain calibration software), Stan Hudson and Steve Miller are particularly appreciated. I would also like to thank Nick Scoville and Anneila Sargent for their support of the project and the generous amounts of engineering and observing time allocated. Polarization observing at OVRO is supported by a NASA Origins grant.

Conversations about polarization with Alyssa Goodman, David Schleuning and Roger Hildebrand were particularly enlightening. David S. and Geoff Blake kindly gave me figures for Orion and IRAS 4 respectively. The mm group was a constant source of help and advice in data reduction: thank you Claire, Eugene, Min and Peter.

My adviser, John Carlstrom, first proposed polarization observing at OVRO and was a constant source of help and advice in the initial observations. More importantly, he allowed me to make my own mistakes and was an excellent mentor.

Graduate school would not be bearable without the comeraderie of fellow sufferers. Thanks to Chris, Janet, Rebecca, Laura, and many others.

I can not say enough about the support from my family and Oliver, and so I will not even try.

This thesis is dedicated to the memory of Dr. Richard Akeson.

Abstract

Images of the linearly polarized emission from magnetically aligned dust grains have been used to investigate the magnetic field structure in the dense environments of young stellar objects. These observations provide constraints for theoretical modeling on scales relevant to protostellar disks, envelopes and outflows. Adjustable reflecting polarizers were installed at the Owens Valley Radio Observatory millimeter array to allow observations of polarized emission.

Polarized emission was detected toward two young stellar objects NGC 1333/ IRAS 4A and IRAS 16293-2422. Both sources are highly embedded and considered among the youngest objects known. The strong sub-millimeter and millimeter fluxes indicate a large amount of circumstellar material which may correspond to the magnetically supported envelopes predicted by theoretical models. Toward IRAS 4A, the magnetic field direction implied by the polarization position angle is parallel to the bipolar molecular outflow. Radiative transfer models were calculated and the offset of the polarized emission toward red-shifted outflow is consistent with an hourglass field morphology in the envelope.

The polarized emission toward IRAS 16293 is located between the two binary components. The magnetic field direction coincides with directions seen in one of the four outflow lobes. However, the field direction is perpendicular to the rotation axis of the circumbinary disk. Given the complicated outflow and circumbinary disk structure of the source, a simple model can not explain the implied magnetic field direction or the offset of the polarized emission from the total intensity.

Observations were also made of the Orion KL region, though no polarization was detected. The upper limit to the polarized emissions suggests that the decrease in polarization seen by single-dish surveys toward the high mass young stellar object IRc2, is not due to field tangling.

The implications of significant polarized emission as detected in the envelopes of IRAS 4A and IRAS 16293 are considered for several alignment mechanisms. Alignment by paramagnetic relaxation of thermally rotating grains will not be efficient in these dense, warm regions, and some mechanism for suprathermal grain rotation may be necessary to explain the observations.

These observations clearly demonstrate the power of interferometric millimeter polarimetry in the study of the role of magnetic fields in protostellar condensations.

Contents

List of Figures

List of Tables

Chapter 1 The role of magnetic fields in star formation

1.1 Introduction

The process by which a star forms has been the topic of much theoretical and observational work (see review by Shu, Adams and Lizano, 1987). The current paradigm of star formation includes gravitational attraction triggering the collapse of a molecular gas core into a dense envelope and protostar. A bipolar outflow is formed along the axis and at the same time, material flows onto the protostar through an accretion disk. In the final stage, the infall is terminated leaving the star and a remnant disk.

Magnetic fields are influential during all of these stages (Mouschovias, 1995, and references therein). The magnetic field can support the molecular cloud against gravitational collapse. As resistance to collapse along field lines is less than for collapse perpendicular to the field lines, a uniform field can define a preferential direction for the collapse leading to an alignment of the axis of the envelope, disk and outflow. This alignment is also expected from conservation of angular momentum in the collapse of a rotating core. Most theories of star formation require magnetic fields to remove excess angular momentum and to form energetic bipolar outflows (Shu et al., 1987).

1.2 Cloud and core collapse

The energetics of molecular clouds are governed by gravitational, magnetic, and turbulent forces. Both magnetic fields and turbulence act to support the cloud against gravitational collapse. The relation between these quantities can be expressed by the

virial theorem,

$$\frac{1}{2}\frac{D^2 I}{Dt^2} = 2 * \mathcal{T} + \mathcal{M} + \mathcal{W}, \tag{1.1}$$

where I is the generalized moment of inertia, $\mathcal{T}$ is the kinetic energy (which includes a term for the external pressure), $\mathcal{M}$ is the net magnetic energy and $\mathcal{W}$ is the gravitational energy (Spitzer, 1978). For the case of an isothermal, spherical cloud in approximate virial equilibrium with no velocity field, mass M, and a uniform magnetic field, B, equation [1.1] reduces to

$$4\pi R^3 p_0 = \frac{3MkT}{\mu} - \frac{1}{R}\left(\frac{3}{5}GM^2 - \frac{1}{3}R^4 B^2\right), \tag{1.2}$$

where p_o is the pressure in the external medium. If the core has a density profile $\rho \propto 1/r^2$, more appropriate for cores close to collapse, a factor of 0.066 is included in front of the gravitational energy term (McKee et al., 1993). If the field is frozen into the material in the core, then the magnetic flux ($\Phi = \pi R^2 B$) is constant as the core contracts and the magnetic energy is proportional to Φ^2/R. The gravitational energy for an isolated core is proportional M^2/R, thus the ratio of gravitational to magnetic energy is constant as the core collapses. This has the important consequence that if the magnetic flux can not support the cloud against collapse, then it will never support the cloud at any size. These clouds are termed magnetically supercritical. A cloud in which the magnetic energy is large enough to support the cloud against collapse will never collapse unless the magnetic flux to mass ratio is decreased. These clouds are magnetically subcritical. Detailed model calculations for the critical mass of an isothermal, constant density cloud by Mouschovias & Spitzer (1976) give

$$M_{cr} = 5 \times 10^5 \left(\frac{B}{3\mu G}\right)^3 \left(\frac{n}{\mathrm{cm}^{-3}}\right)^{-2} \quad M_\odot, \tag{1.3}$$

which is independent of the cloud size, as expected. For magnetic flux freezing in a constant density cloud, the magnetic field strength will scale as B $\propto n^{2/3}$, but models of clouds with more realistic density structures found a scaling of B $\propto n^{1/2}$

(Mouschovias and Spitzer, 1976).

Observations of the magnetic field structure over scales as large as kiloparsecs reveal a generally uniform structure within the galaxy (Heiles, 1986). Thus the assumption of a uniform field used above is applicable on large scales. The field strength as measured by OH Zeeman splitting in giant molecular clouds is in the range 10-100 μG (Heiles, 1986). Further evidence for the presence of magnetic fields in molecular cores is found in the shapes of dark cores studied by Myers et al. (1991). Several of the sources in their survey are consistent with prolate rather than oblate geometries. If these clouds are in equilibrium, rather than collapsing, the pressure is lower along the magnetic field lines, and the cloud will be prolate.

Evidence for magnetic support of molecular clouds has been found in the relations between cloud properties. By compiling data for 10's of molecular cloud regions varying in size from $R \sim 0.1$ to 100 pc (Larson, 1981) found scaling relations between the density n, velocity dispersion, σ and the size, R,

$$\sigma \propto R^{0.5}, n \propto R^{-1}. \tag{1.4}$$

From these relations, Larson concluded that most of the regions were gravitationally bound and in approximate virial equilibrium. If the observed velocity dispersions were due entirely to thermal motion, there should be no dependence on size. These relations can be explained if the non-thermal velocity dispersion is due to magnetic energy. Setting the kinetic energy of the non-thermal velocity equal to the magnetic energy, the relation is

$$v_{nt}^2 = \frac{B^2}{2\pi mn}, \tag{1.5}$$

where v_{nt} is the non-thermal velocity. Using data from over 100 clouds with sizes ranging from 0.1 to 100 pc, Myers and Goodman (1988) derived a magnetic field strength in the range 15-40 μG. In their model, the magnetic field provides a significant fraction of the support against gravitational collapse of the cloud.

1.2.1 Ambipolar diffusion

As stated in the previous section, the ratio of gravitational to magnetic energy does not change as the core begins to contract if the field is frozen into the material. Cores which are initially subcritical must lose enough magnetic energy such that gravitational energy dominates before collapse can begin. In a molecular core only the charged particles (gas and dust) are directly constrained by the field lines. If the charged and neutral particles are not completely coupled, the neutral material can collapse through the field lines, forming a supercritical core. This process by which the magnetic flux to mass ratio is decreased during the collapse is called ambipolar diffusion.

The ions and the neutrals are coupled by collisions, and any motion of the ions relative to the neutrals will produce a drag force. The ion drift velocity, v_d, can be calculated by balancing this drag force with the Lorentz force on the ions from the magnetic field,

$$\frac{1}{4\pi}(\bigtriangledown \times \mathbf{B}) \times \mathbf{B} = \rho_n \rho_i \gamma v_d, \tag{1.6}$$

where γ is the drag coefficient. An ambipolar diffusion time scale can be defined as the time for the core to lose magnetic flux and collapse. In models of magnetized cores (Mouschovias, 1976), this time scale is roughly

$$t_d \simeq 10^{14}\ x_i \quad \text{years}, \tag{1.7}$$

where x_i is the ionization fraction. Calculations by McKee (1989) utilizing chemical models appropriate for dense cores ($n > 10^3$ cm^{-3}) produced a scaling for the ionization fraction of

$$x_i \simeq 10^{-5} \left(\frac{n}{\text{cm}^{-3}}\right)^{-1/2}. \tag{1.8}$$

These calculations used cosmic ray ionization at a rate of 10^{-17} sec^{-1} cm^{-3}. Substituting equation [1.8] into equation [1.7], the time scale can be expressed as a function

of the neutral density,

$$t_d \sim 10^9 \left(\frac{n}{10^3 \quad \mathrm{cm}^{-3}}\right)^{-1/2} \quad \text{years.} \tag{1.9}$$

The magnetic field will 'decouple' from the neutrals when the drift velocity becomes comparable to the free fall velocity. Due to a lack of consensus on the relative importance of magnetic reconnection, a wide range for the density at which the field decouples ($10^7 - 10^{12}$ cm^{-3}) has been calculated by several authors (see discussion in Ciolek and Mouschovias, 1993).

Magnetic flux can also dissipate through magnetic reconnection. The time scale for ohmic diffusion is $\sim L^2/\eta$, where the resistivity η is proportional to the electron-neutral collision rate. For this process to occur on the same time scale as ambipolar diffusion, some calculations estimate that the densities must be $> 10^{12}$ cm^{-3} (Umebayashi and Nakano, 1990). However, this density depends critically on geometry and dynamics and is not well determined (McKee et al., 1993). For densities $< 10^8$ cm^{-3}, ohmic diffusion is less important in the formation of supercritical cores than ambipolar diffusion.

1.2.2 Removal of angular momentum

Comparing the rotation rates of molecular clouds, dense cores and stars, it is clear that some process must act to remove angular momentum during star formation. This can be seen by comparing the specific angular momentum (J/M) of a molecular cloud to that of a star. A lower limit to J/M for a molecular cloud can be calculated by assuming a rotation rate caused by galactic rotation ($\omega \sim 10^{-15}$ sec^{-1}) and an initial radius of $\sim$1 pc, corresponding to the radius necessary to enclose 1 M$_\odot$ at a density of 10 cm^{-3}. The specific angular momentum for the cloud is $\sim$0.03 km sec^{-1} pc, while for the sun $J/M = 9 \times 10^{-6}$ km sec^{-1} pc. The rotation rate used above is an extreme lower limit, and higher values will only increase the amount of angular momentum which must be dispersed. In a survey of $\sim$10 clouds with R $\sim$ 1 pc,

Arquilla and Goldsmith (1986) found $J/M \sim 0.3$ km sec^{-1} pc while observations by Goodman et al. (1993) of ~40 dark cores (R $\sim$ 0.1 pc) found an average specific angular momentum of $\sim 10^{-2}$ km sec^{-1} pc. These observations suggest that angular momentum is removed during the formation of dense cores which eventually form stars. While the angular momentum observed toward dense cores is still much larger than that of a single star, the formation of a binary or protostar/disk system could in principle account for the angular momentum observed in dense cores. If angular momentum is conserved during the collapse, the radius at which centrifugal and gravitational forces are balanced is

$$r_c = \frac{(\Omega R_o^2)^2}{GM}, \tag{1.10}$$

where R_o and M are the radius and mass at the beginning of the collapse. Using typical values of $\Omega R_o^2 = 6 \times 10^{20}$ cm^2 sec^{-1} and $M = 20$ M$_\odot$ from Goodman et al. (1993) for a 0.1 pc core, this radius is 180 AU, roughly equal to the predicted and observed radii of accretion disks around young stellar objects (§ 1.3).

Magnetic braking, in which the magnetic field acts to regulate the angular momentum of a rotating cloud was first proposed by Mestel and Spitzer (1956). If a cloud with a magnetic field is rotating faster than the surrounding material, Alfvén waves are generated. These waves transport angular momentum and act to bring the cloud back into corotation with the surrounding material. The time scale for this process is approximately the time for the Alfvén waves traveling through the ambient medium to propagate through a volume of material with the same moment of inertia as the cloud (McKee et al., 1993). Thus, this time scale is highly dependent on the cloud and field geometry. Mouschovias (1995) derived the magnetic braking time for several configurations of field and cloud geometry and concluded that magnetic braking is sufficiently effective to remove angular momentum from cores rotating either parallel or perpendicular to the magnetic field. If the cloud is contracting faster than the magnetic braking time, the angular momentum is nearly constant and centrifugal

forces prevent further collapse perpendicular to the axis of rotation until magnetic braking can remove more angular momentum (Mouschovias, 1995). If the rotation axis and magnetic field are aligned, both will act to limit contraction perpendicular to this axis, leading to an alignment of the field with the minor axis of the core.

1.3 Formation of disks and envelopes

From the balance of gravitational and pressure forces, an isothermal sphere will have a density profile $n \propto 1/r^2$. As the central core becomes supercritical and begins to collapse, the outside mass looses pressure support. Thus, contraction of an isothermal sphere leads to inside-out collapse, in which the infall wave travels outward at the sound speed (Shu, 1977). If the core is rotating, a disk forms naturally. Tereby et al. (1984) calculated the exact solutions for rotation as a perturbation on the inside-out collapse. Recently, several groups have considered the collapse of a core with a uniform magnetic field (Galli and Shu, 1993; Fiedler and Mouschovias, 1993). In this case, the collapse propagates as a MHD wave perpendicular to the magnetic field lines, which is faster than the sound wave propagating parallel to the field (Galli and Shu, 1993). This leads to a prolate shape immediately inside the expansion wave.

As the collapse continues in the magnetized model, curving field lines force radially infalling material toward the equatorial plane, producing an oblate distribution. This envelope (or 'pseudodisk') is magnetically supported and is roughly 1000 AU in size for a $\sim$ 1 $M_\odot$ protostar. On smaller scales ($\sim$100 AU), a centrifugally supported accretion disk is formed. The radius of the accretion disk depends on the initial rotation rate and grows as t^3 (Tereby et al., 1984). The size of the accretion disk toward objects nearing the end of the accretion phase has been directly confirmed by observations of HL Tau and L1551 (Lay et al., 1995). The radius of the envelope (for the Galli and Shu model) depends on the initial magnetic field strength and increases as $t^{7/3}$. They give values for the specific example of a 0.7 $M_\odot$ protostar after $\sim 10^5$ years. At a radius of 250 AU, the density is 10^7 cm^{-3} and the magnetic field strength

is ~1 mG. The radius of the envelope has grown to 350 AU, while the accretion disk is more than an order of magnitude smaller. These values are considerably smaller than envelopes and disks around observed young stellar objects; however, both the disk and envelope radius are very sensitive to the age of the object.

In the collapse of an unmagnetized core, the infall rate is dependent only on the ambient sound speed (Shu, 1977). Galli and Shu (1993) found that the mass infall rate for their model of a magnetic core was modified only slightly from the isothermal case. The magnetic effects, a reduction in the infall velocity due to the Lorentz force and an increase in the collapsing mass, are opposite is sign and very nearly cancel. However, Ciolek and Mouschovias (1995) calculated that for a supercritical core surrounded by a magnetically supported envelope, the mass infall rate is exceedingly small outside the radius of the core if UV ionization from the external radiation field is included for low optical depths in the envelope. This limits the mass available to the forming protostar to that in the supercritical part of the condensation.

There are several pieces of observational evidence which support the existence of large envelopes around young stellar objects. Calculations by Bastien and Menard (1988) required a flattened dust distribution with size ~1000 AU to reproduce the observed polarization structures surrounding young stellar objects. Millimeter interferometers provide a good method of detecting the mass surrounding young stellar object (see review by Beckwith and Sargent, 1993). Observations of molecular line emission tend to trace distributions that are ~1000 AU (corresponding to the envelopes). The millimeter continuum emission traces only extremely dense gas (the accretion disk) and is unresolved for most sources, implying accretion disk radii < 100 AU.

1.4 Outflows

The number of outflows detected from young stellar objects has greatly increased over the last several years (Bachiller and Gomez-Gonzalez, 1992). Observed outflow

components include fast ionized jets, Herbig-Haro objects, neutral winds and molecular outflows. It is now widely believed that all protostars pass through an outflow stage. In most models, the outflow is necessary to remove angular momentum from material in the centrifugally supported accretion disk. The theoretical models range from collimated stellar winds to magnetohydrodynamic (MHD) winds either from the disk or the star/disk boundary (Konigl and Ruden, 1993).

The magnetic field is important in all of these models. In the stellar wind models, the spherical wind forms a jet through interaction with the magnetically collimated neutral outflow (Konigl and Ruden, 1993). In the MHD models the gas is accelerated by magnetic field lines originating in the disk or star and is flung out by the centrifugal force. Discriminating between the different MHD models on the basis of the magnetic field structure would require resolving the field in the accretion disk.

If the rotation axis of the collapsing system is parallel to the magnetic field lines, the outflow and the field will be parallel. In a comparison of outflow direction and large scale magnetic field direction by Strom et al. (1987), alignment within 30° was found for 70% of the young stellar objects. However, this represents alignment on the sky, rather than in three dimensions, and the actual correlation of directions may be much weaker.

1.5 Summary

As discussed in this chapter, magnetic fields play a significant role in molecular cloud dynamics and the formation of stars. While theoretical models incorporate magnetic fields, observational constraints on these models are difficult to obtain. Most observations of the magnetic field structure and strength pertain to diffuse regions of molecular clouds. The methods that were used for these observations (discussed in Chapter 2) are not suited to the dense regions in which stars are currently forming. This thesis describes a project to investigate the magnetic field structure in the protostellar environment. Techniques of observing magnetic fields and a basic motivation

for interferometric polarimetry are given in Chapter 2. The hardware and software designed specifically for the project are described in Chapters 3 and 4. The data and results are discussed in Chapters 5 and 6. Chapter 7 contains future plans and the project is summarized in Chapter 8.

Chapter 2 Observations of the magnetic field in molecular clouds

2.1 Methods of observing the magnetic field

Magnetic fields are generally detected by observing polarized radiation. At millimeter wavelengths, the emission towards low-mass star forming regions is dominated by thermal emission from dust grains and rotational transitions of molecules. In the following discussion of methods for observing magnetic fields in star formation regions, I do not include polarization of synchrotron emission. While observations of polarized emission from accelerated electrons (synchrotron emission) are important for studying the magnetic fields of highly energetic objects such as quasars, young stellar objects are not significant sources of energetic electrons. In section 2.6, I discuss why Faraday rotation is not important for observations of the magnetic field in the dense regions where stars form. Thus, for molecular clouds, the relevant techniques are Zeeman splitting, selective absorption/emission by magnetically aligned dust grains and polarization of line emission. In section 2.7, I will discuss why millimeter interferometric polarimetry imaging is an ideal method to examine the magnetic field structure in protostellar condensations.

2.2 Zeeman splitting

If an atom or molecule has a magnetic moment (from an unpaired electron or a nuclear magnetic moment), an external magnetic field will remove the degeneracy in states with nonzero angular momentum. The transition is split into one π state which is linearly polarized and two σ states which are elliptically polarized. The emission from

the σ states is shifted in frequency. The frequency difference between the σ states and the unshifted π state is given by

$$\pm \Delta\nu_Z = \frac{g\mu_o}{h} B, \tag{2.1}$$

where g is the Lande g-factor, μ_o is the Bohr magneton, and B is the magnetic field strength. For a molecule with a nuclear magnetic moment, μ_o is replaced by the nuclear magneton, and the frequency shift (referred to as the Zeeman splitting) is reduced by a factor of 1836. For most astronomical conditions, except for maser lines, the Zeeman splitting is much smaller than the line width, $\Delta\nu$. If the splitting can be measured directly, the magnetic field strength is given by equation [2.1]. For the usual case of $\Delta\nu_Z << \Delta\nu$, Zeeman splitting is detected by measuring the circular polarization. The amplitude of the Stokes parameter V (right circular – left circular) depends on the line-of-sight component of B, as the elliptical polarization of the σ components appears completely circular if viewed parallel to the magnetic field. The relation between the total intensity, I, and the circular polarization is derived by Crutcher et al. (1993) as

$$V(\nu) = \frac{dI(\nu)}{d\nu} \frac{2g\mu_o}{h} B_{||} = \frac{dI(\nu)}{d\nu} b B_{||}. \tag{2.2}$$

The amplitude of V depends linearly on b, which ranges from 2.8 Hz μG^{-1} for neutral hydrogen (unpaired electron) to 2.9×10^{-3} μG^{-1} for H_2O (nuclear magnetic moment).

Most successful detections of Zeeman splitting are from HI observations. However, in molecular clouds, most of the hydrogen is molecular and the HI emission arises primarily from the edge of the cloud or near a strong UV source. The 1.6 GHz transitions of OH are most often used to look for Zeeman splitting in molecular clouds. Magnetic field strengths (line-of-sight) measured for large, dense regions range from 10 to 100 μG, for densities $\sim 10^{3-4}$ cm^{-3} (Troland, 1990). Zeeman splitting has also been detected in OH masers, such as those associated with the Orion KL region,

where the measured field strength is a few mG in regions with densities of 10^7 cm^{-3} (Johnston et al., 1989).

To probe the magnetic field strength in star forming cores, observations of molecules which trace higher densities are necessary. Proposed candidate species include CN, SO and CCS. Of these molecules, CN has the highest b factor, but traces densities an order of magnitude lower than the other two. Single dish observations of Orion (3′ north of the KL region) and S106 failed to detect Zeeman splitting in CN at 113 GHz with upper limits $\sim$100 μG (Crutcher et al., 1996).

2.3 Aligned grains

The first polarization observations of optical starlight revealed well behaved polarization vectors across large regions of the sky (Hall, 1949; Hiltner, 1949). The correlation of the polarization percentage with reddening and the structure of the polarization directions led Davis and Greenstein (1951) to suggest that the polarization was due to absorption from elongated dust grains aligned by the magnetic field (selective extinction). The proposed mechanism for aligning the grains was the removal of angular momentum perpendicular to the magnetic field by paramagnetic relaxation. Other proposed alignment processes include bulk motion of the gas with respect to the grains, first discussed by Gold (1952) and alignment by the radiation flux incident on the dust grain (Harwit, 1970). Comparison of the magnetic field in the galactic plane from optical selective extinction and synchrotron polarization emission observations demonstrate that the optical selective extinction polarization direction is parallel to the magnetic field direction (Greenberg, 1978), as expected for magnetically aligned grains. While difficulties remain with the efficiency and time scale for alignment by paramagnetic relaxation, it is believed to be the alignment mechanism in many astronomical situations.

2.3.1 Grain properties

In order for any polarization to be present in the emission from or absorption due to a grain, its cross section along the line of sight must be non-spherical. The linear polarization percentage depends on the grain shape and the dielectric constant. The polarized emission is given by

$$P = \frac{\sigma_a - \sigma_b}{\sigma_a + \sigma_b}, \tag{2.3}$$

where σ_a and σ_b are the cross sections along the major and minor axis of the grain. The absorption (and emission) cross sections for elliptical and oblate spheroids are given by Wickramasinghe (1973). For a dielectric constant of $1.6+i0.005$, the emission from an oblate grain with a 1:2 axis ratio is 24% linearly polarized, while the emission from a prolate grain with the same axis ratio is 25%. However, as the mean cross section from a rotating prolate grain with its spin axis aligned in the plane of the sky is only half the geometric cross section, the observed polarization will be only 13% for this example grain.

The observed polarization along one line of sight for an ensemble of grains will depend on the alignment efficiency and the angle of the magnetic field from the plane of the sky. This reduction factor is given by

$$\Theta = R cos^2 \phi \tag{2.4}$$

where R is the Rayleigh reduction factor, which accounts for the alignment efficiency, and ϕ is the angle of the magnetic field to the plane of the sky. A reduction factor of 1 corresponds to perfect alignment.

Hildebrand and Dragovan (1995) used recent far-infrared polarization data to derive limits on the grain shapes. The maximum polarization percentage in their observations was 9%, which requires a grain axis ratio of 0.9 if the grains are oblate (0.82 for prolate) and the alignment is perfect. They also compared the shape of the 9.7 μm polarization absorption feature with the spectra expected from silicate grains

of different shapes and calculated a best fit for oblate grains with an axis ratio of 2:3. If the grains are oblate with a axis ratio of 2:3, then the reduction factor to produce a polarization percentage of 9% is ~0.25.

2.3.2 Barnett effect

The Barnett effect refers to the process by which the rotational axis of a grain is aligned with the axis of largest moment of inertia by internal dissipation and was first discussed by Purcell (1979). If the dust grain temperature is lower than that of the surrounding gas, the gas will transfer energy to the grain through collisions. This rotational energy is dissipated into thermal energy by the grain. The rotational energy and the angular momentum are related by the moment of inertia

$$E_{rot} = \frac{J^2}{2I}. \tag{2.5}$$

As the dissipation is an internal process, the angular momentum is conserved and the grain will rotate about the largest moment of inertia. For a spheroidal grain, the largest moment of inertia corresponds to rotation about the smallest axis. If the grains are warmer than the gas, the energy transfer occurs in the opposite direction and the rotation axis is aligned with the smallest moment of inertia. Thermal fluctuations prevent perfect alignment of the angular momentum with the largest moment of inertia axis if $T_{dust} > 0$ (Roberge, 1996).

2.3.3 Paramagnetic relaxation

As dust grains have a magnetic moment, $\mathbf{M}$, an external magnetic field will produce a torque in the direction $\mathbf{M} \times \mathbf{B}$. This torque produces a precession of the axis of angular momentum about $\mathbf{B}$. The magnetic susceptibility of paramagnetic material in an oscillating (or rotating) magnetic field is complex (Spitzer, 1978). The imaginary component produces a magnetic moment $\mathbf{M}'' = \chi''\omega^{-1}(\omega \times \mathbf{B})$, where χ'' is the

imaginary component of the complex susceptibility. The torque produced by the interaction of the magnetic field and this magnetization is in the direction $M'' \times B$. This torque acts to align the rotational axis, $\hat{\omega}$, along the direction of the magnetic field.

Alignment of $\hat{\omega}$ and **B** by paramagnetic relaxation is somewhat analogous to the Barnett effect. Grains are spun-up by collisions with gas and this rotational energy is dissipated into internal energy in the grains. Therefore, one condition for effective alignment is that the gas kinetic temperature is greater than the dust internal temperature.

The Barnett effect will cause the grain to rotate about the major axis of inertia on a much shorter time scale (< 1 year) than the magnetic alignment time (Purcell, 1979). Thus, aligning the rotational axis with the magnetic field means the long axis of the grain, either prolate or oblate, is perpendicular to the magnetic field direction (for a dust temperature less than the grain temperature). Emission from these grains will be linearly polarized, with the direction of the polarization perpendicular to the field direction in the plane of the sky, while the polarization for selective absorption will be parallel to the magnetic field direction.

The efficiency of alignment by paramagnetic relaxation depends on the time scales involved. The alignment time for the Davis-Greenstein mechanism is roughly

$$t_r = \frac{I_z}{B^2 V \chi'',} \tag{2.6}$$

where I_z is the moment of inertia about the spin axis, V is the volume of the grain, and a typical value for the imaginary component of the susceptibility is $2.5 \times 10^{-12}\ \omega/T$ (Spitzer, 1978). The numerical coefficient is calculated by estimating the percentage of paramagnetic atoms (those with unpaired electrons) and is therefore dependent on the assumed grain composition. For a dust grain at 10 K with a radius of 0.1 μm and density of 1 gm cm^{-3} in a magnetic field of 10 μG, the alignment time is $\sim 10^5$ years. The alignment can be disrupted by collisions with gas or dust particles which

change the rotational velocity. While the collisions are isotropic, a large number of collisions, n, will produce a root mean square change in the angle between the axis of rotation and the magnetic field of $(nm_H/m_d)^{(1/2)}$ (Davis and Greenstein, 1951) for collisions with hydrogen atoms. For a gas to dust mass ratio of 100:1, the time for one dust grain to collide with its own mass in gas is $\sim 10^4$ times shorter than the time to collide with another dust grain (for grains with $r = 0.1$ μm) so only gas collisions are considered. If the gas damping time is less than the paramagnetic relaxation time scale, there should be no uniform alignment. The gas damping time is approximately the time for the grain to collide with its own mass of gas or $\sim a\rho/nmv$, where a and ρ are the grain radius and density and n, m, v are the gas density, mass and velocity. A minimum magnetic field strength necessary for alignment can be estimated by equating these two time scales, and is given by

$$B = 13\mu G \left(\frac{n}{100\ \mathrm{cm}^{-3}}\right)^{1/2} \left(\frac{T}{10\ K}\right)^{3/4}. \tag{2.7}$$

The proportionality of B to n agrees roughly with Zeeman observations spanning a range of densities (Heiles et al., 1993), thus if this process works at one density, it should work at all densities (assuming all other variables remain constant). However, the magnetic field strengths required by equation [2.7] are an order of magnitude larger than those observed.

Good alignment efficiency by paramagnetic relaxation requires both a dust temperature less than the gas temperature and a magnetic alignment time less than the gas damping time. Given the discrepancy in the magnetic field strength required to meet the second condition for the assumed grain parameters, the efficiency of paramagnetic relaxation alone is not sufficient to explain the observations of well ordered fields if gas damping limits the alignment.

2.3.4 Superparamagnetic grains

The paramagnetic relaxation alignment time can be reduced if the value of the imaginary component of the susceptibility is increased. If molecules including iron are present in the grain, it can be superparamagnetic. In these grains, the value for the imaginary component of the susceptibility can be increased by as much as 10^6 (Jones and Spitzer, 1967). The alignment time is then decreased by the same factor, and is subsequently much less than the gas damping time. Recently, it has been suggested that glass with embedded metal and sulfides (GEMS) could be the source of superparamagnetic inclusions in grains (Goodman and Whittet, 1995; Martin, 1995). GEMS have been studied in samples of dust particles collected in the Earth's stratosphere and contain FeNi and Fe(Ni)S (Martin, 1995). Larger grains may have a higher probability of containing a superparamagnetic inclusion, and will have a higher alignment efficiency. However, these grains were probably processed in the pre-solar nebula and their properties may not be representative of the properties of grains in the ISM.

2.3.5 Suprathermal rotation

Another proposed solution to the alignment time scale problem is suprathermal rotation of the dust grain. The kinetic energy from absorption of energetic photons or the ejection of H_2 molecules from the grain surface is much larger than the kinetic energy corresponding to the gas or grain temperature. As first proposed by Purcell (1979), if these events take place only on specific sites on the grain, the rotation rate can greatly exceed the thermal rotation rate. The alignment time scale for suprathermally rotating grains by paramagnetic relaxation is still given by equation [2.6]. However, the de-alignment time is now set by the time the grain continues to rotate in the same direction rather than the gas damping time (Hildebrand, 1988). This is because the magnitude of the torques driving the suprathermal rotation is much larger than the de-aligning torques due to gas-grain collisions. Thus, alignment of suprathermally rotating grains does not require $T_{dust} < T_{gas}$.

The accretion of gas onto the surface of the grain may be sufficient to change the sites of H_2 formation and thus reverse the spin direction. If the accelerating torques change sign, the rotational velocity will be zero at some moment, and the axis of rotation can be de-aligned from the magnetic field direction. Spitzer and McGlynn (1979) found that the grain will be completely de-aligned after two or three reversals. For cosmic abundance values and a dust density of 1 gm cm^{-3}, the time to accrete one layer is

$$t_a = \frac{1.1 \times 10^{12} \text{ s}}{n(\text{cm}^{-3})\xi}, \tag{2.8}$$

where ξ is the sticking parameter (Spitzer, 1978). For a density of 100 cm^{-3} and a sticking parameter of 0.1, the accretion time is 4×10^3 yr. This time is less than the paramagnetic relaxation time given above for a field strength of 10μG. However, the sticking parameter is quite sensitive to the grain surface and may be as low as 5×10^{-5} for silicate grains (Leitch-Devlin and Williams, 1985), in which case the accretion time is increased to 8×10^6 years.

Another process that may change the location of preferential H_2 formation sites is the formation of ice mantles on the grains. Grain chemistry models by Hasegawa et al. (1993) calculated a mantle thickness of 10 to 100 monolayers after 10^5 years in a cloud with $n = 10^4$ cm^{-3}. If the accretion of monolayers scales linearly with time, a few monolayers will have accreted after $\sim 10^4$ years. If the accretion time scale limits the alignment by paramagnetic relaxation, then the field strength must scale as $n^{1/2}$ in regions where polarization is observed, the same density dependence given for the gas damping time limiting the alignment. Suprathermal rotation may not have as large an effect in dense molecular cores where the abundance of atomic hydrogen is low and mantle accretion is faster.

2.3.6 Other alignment mechanisms

Gold (1952) considered alignment by bulk motion of the dust with respect to the gas. Random impacts with streaming gas particles align the largest average projection of

the grains along the streaming direction. The same effect can be accomplished by an energetic, anisotropic radiation flux. In a recent study of alignment by a supersonic gas flow, Lazarian (1995) found grains can be efficiently aligned by radiative fluxes or Alfven waves even if the random torques are dominated by the formation of H_2 molecules.

A specific case of grain alignment through gas-grain collisions is the ion-neutral drift produced by ambipolar diffusion, studied in detail by Roberge, Hanany, & Messinger (1995). The velocity drift is perpendicular to the magnetic field direction, so for the grain to present the minimum cross section to the gas flow, the long axis will be perpendicular to **B**. Roberge et al. (1995) calculated the 100 μm polarization percentage versus ion-neutral drift speed. The density and magnetic field strength used in their calculations (n=10^4 cm^{-3} and B = 30 μG) are appropriate for dense molecular clouds. These values correspond to a drift velocity of 0.1 km sec^{-1} for a region 0.01 pc in size, for which the polarization calculated by Roberge et al. (1995) is less than 0.2%. The polarization percentage will increase with higher ambipolar diffusion velocities. While mechanical alignment due to ambipolar diffusion may operate in some astronomical situations, it can not explain the large scale uniformity over 10's of parsecs in the polarization vectors observed toward molecular clouds.

2.4 Polarization of line emission

Polarization of molecular line emission can occur if the magnetic sub-levels of a molecule are unequally populated and there is a magnetic field present (Goldreich and Kylafis, 1981). The field will align the quantization axis of the molecule. This alignment causes different emissivities perpendicular and parallel to the magnetic field direction. Thus, the resulting emission will be linearly polarized. The amount of polarization depends on the relative populations in the sub-levels and is proportional to $sin^2\alpha$ where α is the angle between the direction of propagation and the magnetic

field. The polarization percentage will be highest when the optical depth is near 1, as the radiation will be more isotropic for high optical depths and the population difference will be small at low optical depths. Effects that may produce the necessary unequal level populations include anisotropic radiation fields or anisotropic optical depths due to velocity gradients.

Until recently, attempts to detect this effect with single-dish millimeter observations were unsuccessful (Wannier et al., 1983; Lis et al., 1988). In part, this may be due to averaging over magnetic field structure and velocity gradients in the large beams. A detection of this effect in the sub-millimeter has recently been reported by Greaves et al. (1996) in the JCMT newsletter. Polarization levels of 0.4-2.5% were claimed for observations towards high mass star forming regions and the Galactic center. The angular resolution of these observations was considerably higher than previous studies, because of the higher frequencies used, and may suggest that this effect is observable on the smaller scales probed by interferometers. For many low mass star forming regions the molecular line emission is considerably brighter than the continuum emission from dust; therefore, this effect could be an important tool in probing the magnetic field structure in these regions.

2.5 Faraday rotation

Electrons in a magnetic field will change the position angle of an incident linearly polarized wave. This shift is called Faraday rotation. The electrons are rotating either clockwise or counter-clockwise depending on the direction of the magnetic field. Thus, the index of refraction will be different for right and left circularly polarized waves. As any linearly polarized wave can be described as the combination of two circularly polarized waves, this effect rotates the position angle of a linearly polarized wave. The phase shift, which depends on the electron density, n_e, and magnetic field

strength along the line of sight, $B_{||}$, is proportional to

$$\Delta\phi \propto \lambda^2 \int n_e B_{||} dl. \tag{2.9}$$

While this effect has been used to measure the Galactic magnetic field (Heiles, 1986), its magnitude is much smaller within a molecular cloud. For a 0.1 pc cloud with $n = 10^4$ cm^{-3}, B= 30μG, and $n_e/n = 10^{-3}$, the angle rotation at 3 mm is only 10^{-2} degrees. For the interstellar medium along the line of sight to a star forming region, typical values are B = 1 μG, $n_e = 0.03$ cm^{-3} and d=100 pc. These values give a phase shift of 10^{-3} degrees at 3 mm, thus Faraday rotation will not affect observations of polarized dust emission. Faraday rotation of background source emission is also unsuitable as a method for observing the field within a dense core, as the shift is given by the entire field along the line of sight. Even if an appropriately placed background source was present, the contribution from the dense core could not be separated from that of the molecular cloud and the interstellar medium.

2.6 Why interferometric polarimetry?

Molecular core properties such as non-spherical core shapes and non-thermal line widths can be explained through the presence of magnetic fields; however, these properties can be explained by non-magnetic processes as well. Observations of polarized emission are a better method for investigating the magnetic fields in star forming regions. Observations of optical and infrared selective extinction are not possible because the extinction toward protostars are much too high ($A_v > 100$) to see background sources. For some objects the young stellar object itself is too embedded to be visible at wavelengths shorter than the far-infrared. However, this same dust will emit polarized radiation in the far-infrared through millimeter wavelengths. Observations of this emission directly trace the magnetic field structure of this dense material.

The dust emission from protostellar disks and envelopes is very strong at far-

infrared and sub-millimeter frequencies. Unfortunately, the resolution of the current generation of far-infrared and sub-millimeter telescopes is much larger than the size of the objects themselves. High resolution is necessary to resolve the field structure even in near-by star forming regions. For example, a 1000 AU envelope subtends only 3″ on the sky at the distance of the Perseus cloud (∼350 pc). At millimeter wavelengths, interferometers are available which provide the necessary resolution. At 1 mm, the highest resolution currently available at existing millimeter interferometers is ∼1″. An additional advantage of using an interferometer is that emission from large, smooth structures (such as the larger molecular core surrounding the protostar) is spatially filtered. Accordingly, we have implemented polarization capabilities at the Owens Valley Radio Observatory millimeter array in order to image the polarized emission and determine the magnetic field structure in protostellar condensations.

Chapter 3 Polarization hardware and calibration

3.1 Owens Valley mm array

The Owens Valley Radio Observatory (OVRO) millimeter array is located near Big Pine, California, at an elevation of approximately 4000 feet. The interferometer consists of six 10.4-meter dishes on north-south and east-west baselines. The current maximum spacing (1995-6 observing season) is 235 meters north-south and 200 meters east-west. The receivers are located at the Nasymth focus and each telescope has two receivers, one operating in the 80 to 116 GHz band and one operating in the 210 to 270 GHz band. Continuum emission is measured with a 1 GHz broadband analog correlator. The spectrometer consists of four independent modules of 64 channels each with a resolution range of 16 kHz to 4 MHz.

3.2 Polarization receivers

Polarized emission is generally described by the four Stokes parameters: I, the total intensity, V, the circular polarization, and Q and U, the linear polarization. The linearly polarized intensity is given by $\sqrt{Q^2 + U^2}$ and the position angle of the plane of polarization is $\frac{1}{2}tan^{-1}(U/Q)$. For interferometric observations of polarized emission, two orthogonal polarization states, such as right and left circular or vertical and horizontal linear, must be received. All four Stokes parameters are then calculated from the four cross correlations of the two polarization states. Each cross correlation contains both amplitude and phase information. Using circular correlations (here

designated as R and L), the Stokes parameters are given by:

$$\begin{aligned} I &= RR + LL, \\ V &= RR - LL, \\ Q &= RL + LR, \\ U &= i(LR - RL). \end{aligned} \tag{3.1}$$

For crossed linears, the Stokes parameters are given by:

$$\begin{aligned} I &= HH + VV, \\ V &= i(HV - VH), \\ Q &= VV - HH, \\ U &= HV + VH. \end{aligned} \tag{3.2}$$

The linear polarization is measured by combining Q and U. As seen in eq. [1] and [2], for small linear polarizations Q and U are the sum and difference of two small quantities for crossed circulars, but Q depends on the difference of two large quantities in crossed linears, and is therefore sensitive to calibration errors. For observations of weak linear polarization, it is better to cross-correlate circular polarizations rather than linear.

The receivers on the OVRO mm array currently contain only one channel, so two polarizations can not be detected simultaneously. However, all four correlations can be measured by time-multiplexing the polarization detected by each telescope. To convert the linear polarization of the receiver to circular polarization on the sky, a quarter-wave plate is placed in the optical path. A quarter-wave plate is any device which converts linearly polarized emission to circularly polarized emission. Generally, this is accomplished by splitting the linearly polarized signal into two equal components, adding a phase delay of 90° to one component, and recombining the components. One type of quarter-wave plate commonly used at millimeter frequencies

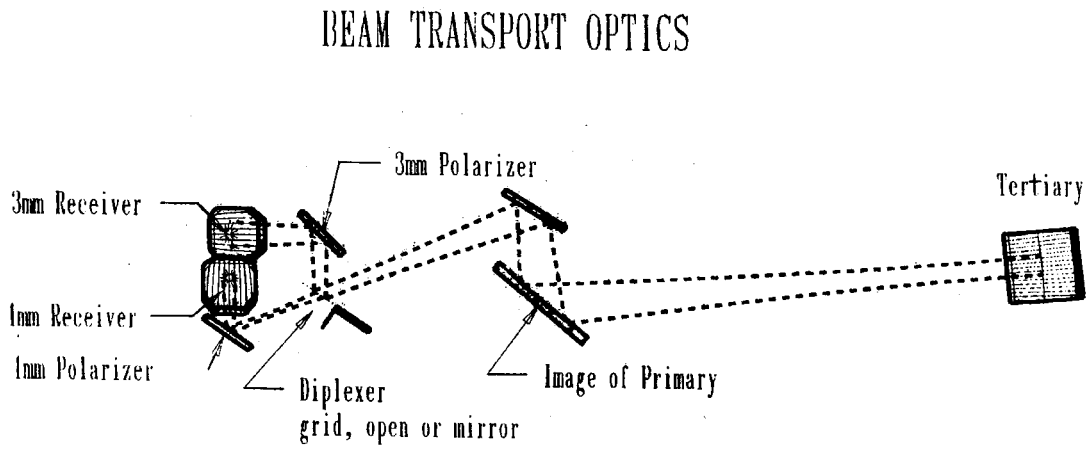

Figure 3.1: The beam transport optics from the tertiary to the receiver window. The polarizer replaced a flat mirror in the optics. Drawing provided by D. Woody.

is a dielectric plate with parallel grooves. The depth of the grooves is chosen so that a 90° phase shift is added to an incident wave polarized parallel to the grooves. While these transmission quarter-wave plates are easily constructed, they are true quarter-wave plates at only one frequency. There can also be difficulties with reflections and absorption by the dielectric material. Since the material is chosen to have different indices of refraction for different polarizations, it can be difficult to equalize the reflections losses for the two polarizations. Because of these problems, we chose to construct reflecting polarizers for use on the OVRO mm array, replacing a flat mirror

in the optical path (Figure 3.1).

3.3 Reflecting polarizers

3.3.1 General design

The reflecting polarizers at OVRO were designed by David Woody. The main components of the reflecting polarizers are a wire grid, which splits the incoming signal by polarization and a flat mirror (Figure 3.2). In this context 'grid' refers to parallel wires in a plane. Both the angle of the wire grid and the spacing between the grid and the mirror are controlled by stepper motors. The angle range spans 135° and includes the positions for vertical, horizontal, left and right circular polarization. Because of the independence of the wire grid angle and the grid-mirror spacing, these devices can convert any polarization state to any other polarization state. Thus, it should be possible to compensate for any non-linearities in the polarization of the feeds, another advantage over transmission quarter-wave plates.

The basic frame of the polarizers is a perpendicular mounting plate (Figure 3.3). The base bolts to the mounting structure in the elevation tube which holds all the telescope optics after the tertiary. The plate extending down into the optical path holds the mounting wheel for the mirror and grid. The rotation axis for the assembly is a differential screw micrometer[1]. The micrometer is clamped into a small (~3 inch) plate. The mirror is attached to this plate through holes in the grid mounting wheel, which is attached to the mounting plate with a ball bearing ring. Thus, the grid and mirror rotate together. The grid angle is measured by a potentiometer attached to the gear which turns the assembly. The distance between the mirror and the grid is measured by a linear voltage transducer[2].

The Gaussian beam at the position of the polarizer has a beam waist of 1.1 inch.

[1] Part # 110-112, Mitutoyo
[2] model D5/40GB with s7AC amplifier, RDP Electrosense

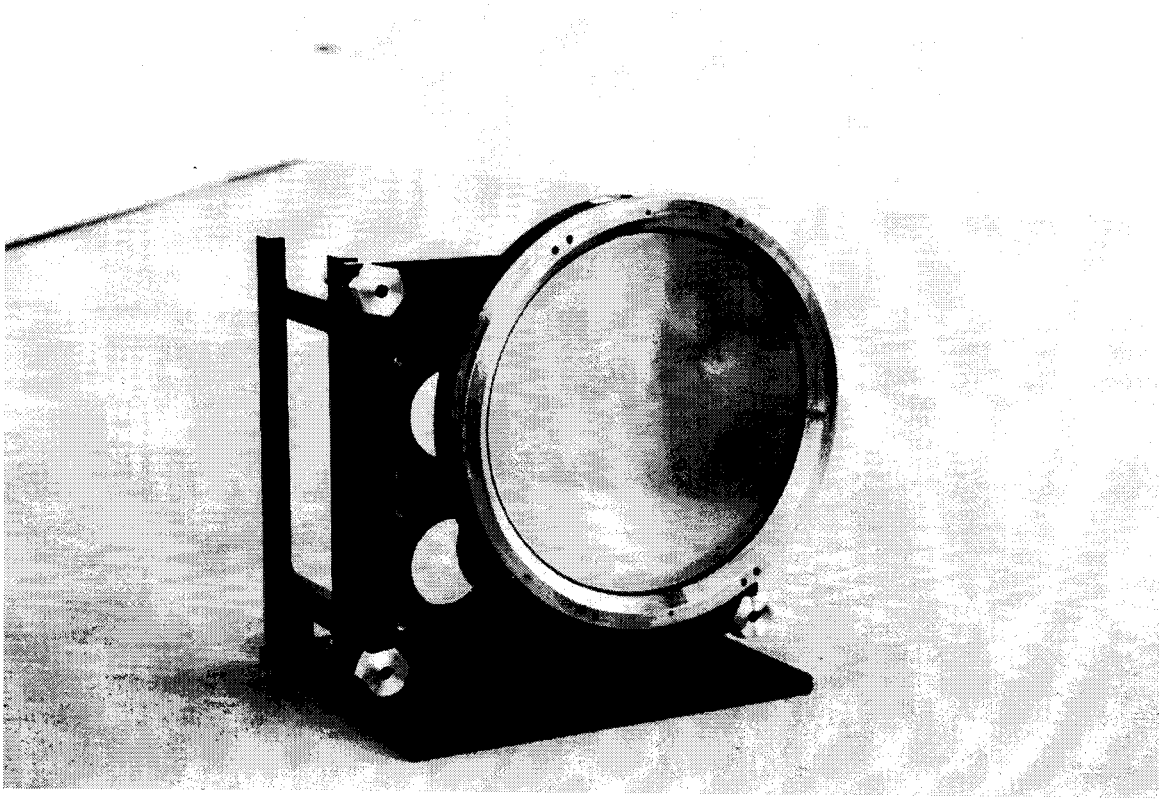

Figure 3.2: An assembled polarizer.

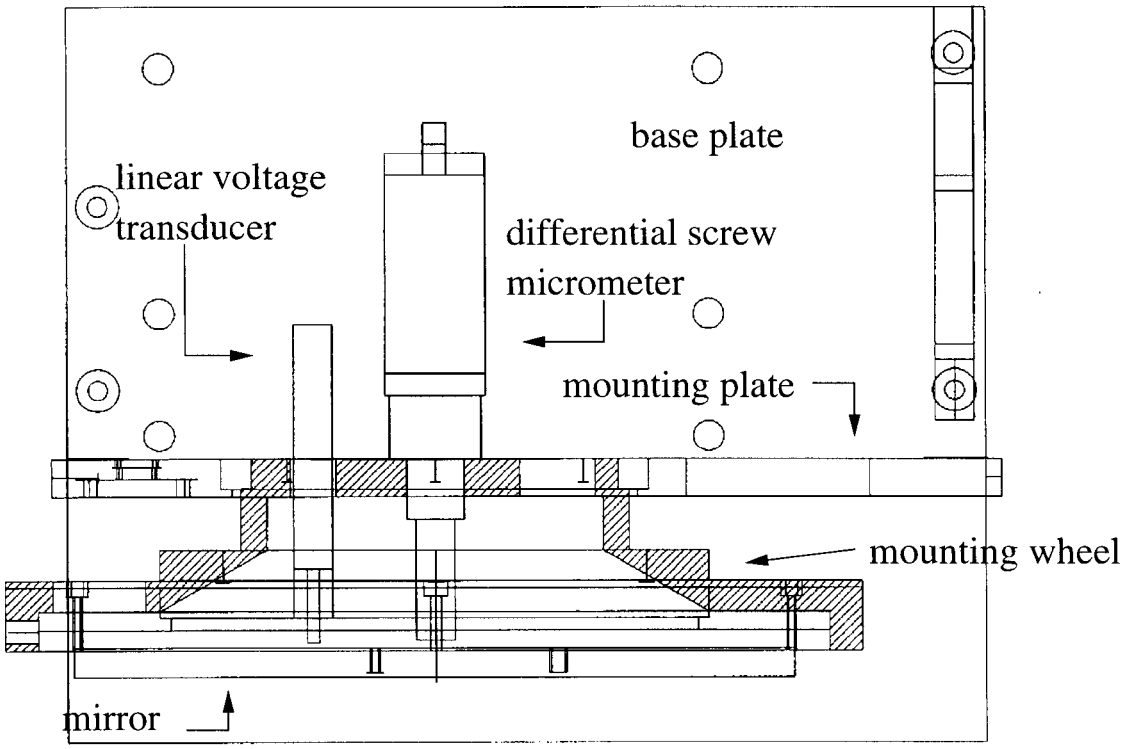

Figure 3.3: Top view of the polarizer design.

The inside diameter of the wire grid is 6 inches, or 5.45 times the beam waist. The angle of incidence is 45° (33.96° for the 1 mm polarizers).

3.3.2 Wire grids

To separate the incoming radiation into orthogonal linear polarizations, we have constructed wire grids, composed of parallel wires attached to a circular frame. This frame is fastened onto the outer rim of the rotating hub on the polarizer. The frames are machined and ground to a parallel and flatness tolerance of ± 0.0005 inches (13 μm). The wire grids are constructed using the winder developed by the sub-millimeter receiver group at the Harvard-Smithsonian Center for Astrophysics (Shapiro and Bloemhof, 1990). One frame is placed in a holder and the tensioned wire is wrapped around the frame as it rotates. For the wire diameter used, the tension was set to ~100 grams. Simultaneous translation of the winder spaces the wire at regular intervals across the frame. The wires are epoxied to the lower frame and fastened with a matching top frame. The top and bottom half of each frame are machined as a pair, so any stresses should be symmetric.

The best surface for reflection is a solid plane, while the best transmission is achieved for empty space. Thus, a grid of wires will have slightly imperfect reflection and transmission. The power reflection coefficients for a grid with wire diameter a and spacing p at wavelength λ if $a \ll p \ll \lambda$ are

$$R_{\|} \simeq \frac{1}{1 + \left(\frac{2p\cos\phi}{\lambda} ln \frac{p}{\pi a}\right)^2}, \tag{3.3}$$

$$R_{\perp} \simeq \left(\frac{\pi^2 a^2}{2\lambda p}\right)^2 \tag{3.4}$$

where ϕ is the angle of incidence (Prigent et al., 1988). The wire diameter and spacing were chosen by balancing the losses from reflection and transmission components for the wire diameters available (15 and 25 μm). At 3 and 1 mm, the best combination of diameter and spacing are 25 μm diameter wire spaced at 125 μm intervals. We have

used 25 μm gold-plated tungsten wire[3]. The ellipticity of the wire is specified to be less than 5%, and I assume the wire is perfectly circular in the following calculations.

Assuming the wire is a perfect conductor, the reflected power for an incident wave polarized perpendicular to the wires is 6.8×10^{-5} at a frequency of 100 GHz. The quantity the interferometer measures is voltage rather than power. The percentage of the signal that is in the wrong state (shifted by 90° instead of 0°) is called the cross polarization voltage and is 0.8% for the perpendicular component. The reflected power for an incident wave polarized parallel to the wires is 0.99925. This corresponds to 2.7% of the voltage being transmitted; however, for the reflecting polarizer the resulting cross polarization is only 0.1%, since the wave must pass through the grid twice before reaching the receiver. So there will be a 3% reduction in the amplitude of the reflected component, but only a very small cross polarization error. At a frequency of 230 GHz, the transmitted and reflected cross-polarizations for a single grid are 1.9% and 7.4% in voltage. However, as explained above, the cross-polarization from the reflected wave is only 0.5%.

There will be some loss from absorption by the metal wires. The gold plating on the wire is 4% by mass, which corresponds to a layer of 0.48 μm for the 25 μm wire. At 100 GHz, the skin depth for gold (resistivity = 2.3×10^{-8} Ω·m) is 0.2 μm, so the radiation does not interact with the tungsten. The reflection coefficient for gold at this frequency is 0.9989. This corresponds to 0.3% loss in voltage due to the absorption. At 1 mm, the loss is 0.4%.

The standard deviation in the spacing using the winder at the CfA was measured to be < 7 μm for a mean spacing of 103 μm (Shapiro and Bloemhof, 1990). At the frequencies for which these grids were designed (80-270 GHz) the degradation in performance due to this error could not be measured with their experimental set-up and is less than 0.5%.

[3]25 μm wire, straightness grade 1, specification # 821/60, Luma, Sweden

3.3.3 Design tolerances

In the design of the polarizers, all tolerances were set to have a cross-polarization voltage of 1% or less. For the grid angle, an error of 0.57° will result in an cross-polarization voltage of 1%. The step size for the grid angle motor is 0.068°. However, in the stepper motor positioning algorithm the typical error is ±1 count. To determine the actual precision of the angle, I analyzed the statistics of the angle position for a track which contained 400 integrations. The average offset from the nominal position ranged from −0.4 to 1.0 counts (0.03 to 0.07°) for the six polarizers. Over both right and left positions for all 6 polarizers, the average error is 0.3 counts. The scatter varies from 0 to 1.9 counts, with an average of 0.65 counts. Thus, the repeatability of the angle position is well within the specified tolerance.

The phase delay added to the transmitted component of the incident radiation is $2\pi(\sqrt{2}d/\lambda)$, where d is the spacing between the grid and the mirror. For a phase error of 1° (1% in cross-polarized voltage), the necessary spacing accuracy in the offset spacing is 3.4 μm. The precision with which the mirror position can be set is 1 μm. At 1.4 mm, this requirement becomes more difficult to achieve, as an error of only 1.6 μm in the spacing will cause a cross-polarized voltage of 1%.

If the grid and the mirror are not parallel, different parts of the beam will be delayed by different amounts. If the spacing at the center is correct, the net phase error will be 0, but there will be a small loss in the transmitted signal from decorrelation. The machining specifications for flatness and parallelness were ±0.0005 inch for the grid frames and ±0.001 inch for the mounting wheel. In the assembly process for the polarizers, the three adjustment screws are set such that the mirror and the mounting wheel are parallel to within ±0.0002 inch. Thus, an estimate for the maximum spacing difference across the grid is 0.0015 inch (3.8 μm). An upper limit to the power lost from this tilt can be simply calculated by assuming the incoming signal is distributed evenly across the grid. The loss in voltage from this effect is only 1.5×10^{-5} at 3 mm and 7×10^{-5} at 1.4 mm.

There will also be a small error in the phase of the transmitted component due to the changing frequency over the continuum correlator. At any one frequency the phase difference from the nominal frequency is $\Delta\phi = \pi\Delta f/2f$, where Δf is the frequency offset. As the cross-polarized voltage is proportional to $sin(\Delta\phi)$, the total phase error across the band will be 0. Though we do not know the exact shape of the continuum passband, any deviation which changes the average frequency is taken into account, as this is the same signal used in the calibration of the polarizer. However, the loss in signal is

$$V_{loss} = 1 - \frac{1}{2\Delta f}\int_{-\Delta f}^{+\Delta f} cos(\frac{\pi f}{2f_o})df \tag{3.5}$$

At 100 GHz, this loss is 0.4%, while at 220 GHz it is 0.005%.

Adding up all the losses detailed in this section, the total loss (in voltage) for the reflected component is 1.1%, while the total loss for the transmitted component is 3.1%. So, neglecting the known sources of cross polarization, the response on the sky of each telescope will be slightly elliptical rather than perfectly circular. At 100 GHz, the ellipticity (1 - b/a) of the response is 0.020. However, as explained in §3.3.1, given the design of the reflecting polarizers it is possible to correct for this factor.

3.3.4 Assembly and control

The grid mounting wheel is attached to the perpendicular mounting plate with a ball bearing ring. The flat mirror is attached to its mounting hub with screws and held at a fixed distance by springs. The flat mirror hub is attached to the micrometer shaft, separated by bent washers, through the center of the ball bearing ring. The distance from the rim of the grid mounting wheel to the polarizer base is set to 5.50 $\pm$ 0.01 inch. The three screws on the mounting plate gussets are used to level the rim with respect to the perpendicular mounting plate to $\pm$0.0002 inch with a precision indicator. Then the flat mirror is adjusted to be parallel to the rim with a tolerance of $\pm$0.0002 inch. The springs and washers were added to the design after the first season of observing (1993-4) to stiffen the polarizer to correct for changes in the grid-mirror

spacing when the polarizer assembly was rotated.

The linear voltage transducer (LVT) is clamped to the back of the grid mounting wheel and passes through a hole to contact the back side of the flat mirror. The gain and offset of the LVT are set to 5 Volt/mm and zero offset. First, the micrometer is set halfway through its range of travel (750 μm) and the LVT is positioned to read 0 when the offset is removed. The gain is then adjusted to 5 Volt/mm, relative to the reading on the micrometer. The offset is reset such that 0 V corresponds to the flat mirror and the grid touching. The linearity tolerance of the linear voltage transducer was given as 0.7% by the company. I measured the linearity directly by comparing the output of the LVT against a digital micrometer. The non-linearity over a large range (1000 μm) was less than 1%. The non-linearity over ranges of 100μm was typically near 1%, but was as large as 3% for a few of the LVT's at some micrometer positions.

3.4 Calibration of polarizers

3.4.1 Astronomical calibration

During the assembly of the polarizers, the micrometer is roughly set to read the spacing between the grid and the mirror. However, this is not accurate enough for polarization observing. An ideal method of finding the correct mirror-grid spacing would be to set one telescope in right circular and one in left circular and adjust the polarizer to null the signal from an unpolarized point source. However, quasars are known to be linearly polarized and the outer planets (Neptune and Uranus) which are unpolarized are resolved on long baselines. Also, a null signal can be achieved on one baseline with crossed ellipticals, rather than true circular polarization.

One alternate method we used was to observe a bright quasar with the polarizers configured as half-wave plates. One telescope was chosen as a reference and the polarization plane on that telescope was defined on the sky with the wire grid that is normally used for frequency diplexing. This procedure ensures the measurements are

using crossed linear polarization rather than crossed ellipticals. The position of the reference grid was set with a digital level. As the polarizers on the other telescopes are rotated with respect to the reference telescope, there will be nulls at 45° and 135° (Figure 3.4). The depth of the nulls depends on how close the grid-mirror spacing is to exactly half a wavelength. The received visibility (normalized) is

$$V = cos\theta cos(\theta + \theta_o) + \epsilon^{i\varphi} sin\theta sin(\theta + \theta_o), \tag{3.6}$$

where θ is the angle of the moving grid, θ_o is the offset between the measured and the actual grid angle, and φ is the phase delay of the transmitted component.

The calibration data were taken with one telescope as a reference and rotating the wire grid angle of all other telescopes. A one minute integration was taken at each grid position. Near the position of the nulls, the spacing between points was less than 2° and a spacing of 5° was used for the rest of the curve. The phase and amplitude calibration was done by taking one integration with all grids parallel to the reference telescope every five integrations. These integrations are used only for calibration, and not in the analysis of the instrumental polarization. The resulting curves are fit to determine the position of the nulls, which are the angles for right and left circular, and the grid-mirror spacing (Figure 3.4). The conversion between potentiometer counts on the grid angle motor and the actual grid position had to be added as a parameter to adequately fit the observed curves. As the errors in the measured phase increase when the amplitude decreases near the nulls, only the amplitudes were fit. The fitting program calculates models with a range of values for all four parameters and finds the one with the highest probability, using a Rice distribution for the amplitudes. The process was repeated with smaller model parameter ranges until the parameter steps were below the mechanical precision in controlling the grid angle and grid-mirror spacing. The quarter-wave grid-mirror spacings are calculated as offsets from the half-wave spacings and any non-linearities in the linear voltage transducer will directly translate to errors in the quarter-wave spacing.

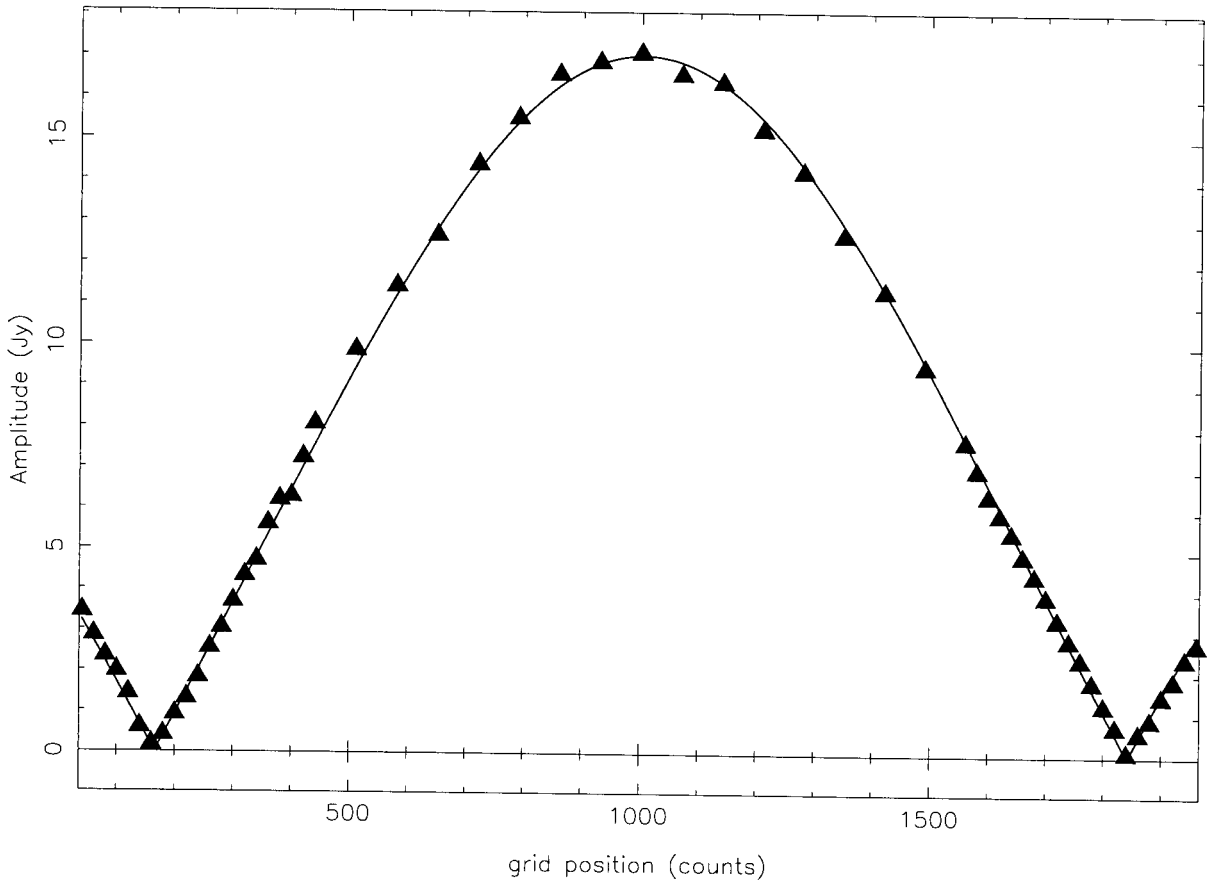

Figure 3.4: A calibration curve for the source 3c273 with one polarizer set as a half-wave plate which is rotated through 135° and the second telescope defined as linear polarization on the sky. The fit curve plotted corresponds to an error in the grid-mirror spacing of 1 μm.

3.4.2 Laboratory calibration

While the calibration method described in the previous section works extremely well in determining the correct grid-mirror spacings for half-wave plates, there are some difficulties. Good atmospheric phase stability is required for the observations and the precision of the derived quarter-wave plate settings depends on the linearity of the linear voltage transducers. While the linearity was checked between the half-wave settings at 86 and 106 GHz, the extrapolation to quarter-wave settings is much larger. The calibration at 1 mm is much more difficult, as the atmospheric conditions must be $\sim$2 times better and the necessary precision for the spacing is 1.6 μm.

We have developed a method of calibrating the grid-mirror spacing in the lab. The phase difference between a signal reflected from the grid and a signal reflected from the mirror will be exactly 90° if the the added path difference is exactly a quarter-wave. The layout of the calibration set-up is shown in Figure 3.5. A phase-locked oscillator transmits through a scalar feed horn, which reflects from the polarizer and is received by an identical feed. Elliptical mirrors are used to transform the beam emitted/received by the feed horns to a beam waist at the polarizer that is the same size as the beam on the polarizer in the telescope. Two wire grids are used to define the polarization of the transmitted and received signal, as the polarization purity of the scalar feed horns is not good. The receiver is a harmonic mixer, which mixes the received signal with the same 6 GHz signal that phase locks the transmitting oscillator (Figure 3.6). The 61 MHz output of the receiving harmonic mixer is then compared to the reference 61 MHz of the phase locking harmonic mixer with a vector voltmeter. The absolute phase difference between the two signals depends on the path length between the transmitter and the receiver. Thus, if we change the path length, the phase difference will change. Specifically, the phase difference between reflection from the polarizer wire grid and reflection from the mirror will be exactly 90° if the spacing is a quarter-wave. A circularly polarized transmitter can be constructed by setting the polarizer using the above procedure and removing the second focusing

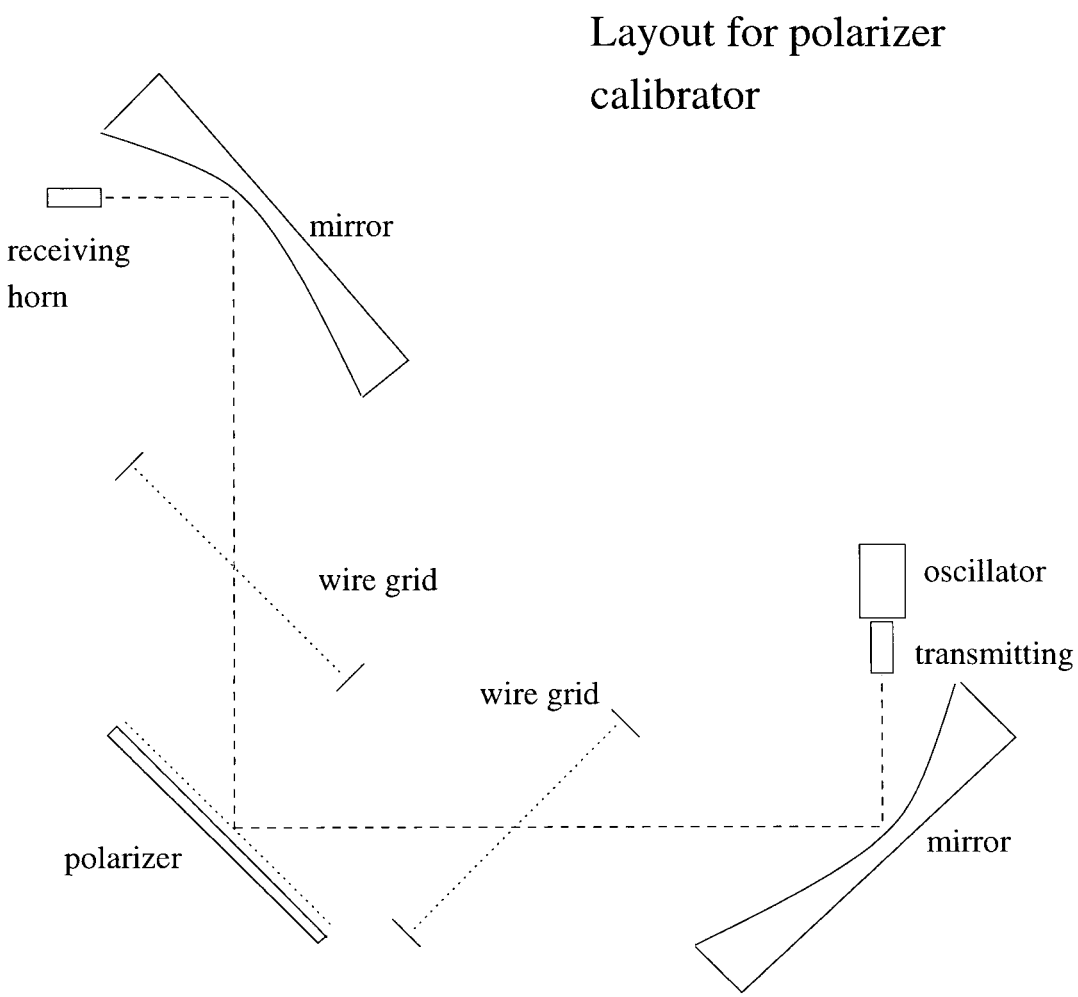

Figure 3.5: The physical layout for the polarizer calibrator.

mirror/receiving horn.

The components for the laboratory calibrator have been machined and the entire assembly has been tested using one of the polarizers (Figure 3.7). The 61 MHz signals to the two harmonic mixers must be extremely well isolated, or cross-talk on this line will affect the phase of the received signal. There are also some standing waves present in the cavity formed by the two horns. These are minimized by placing 10 dB of attenuation in the optical path, which will attenuate the standing wave by 30 dB as it passes through the attenuator three times. Currently, the phase change measured when the polarizer mirror (without the wire grid attached) is moved behaves

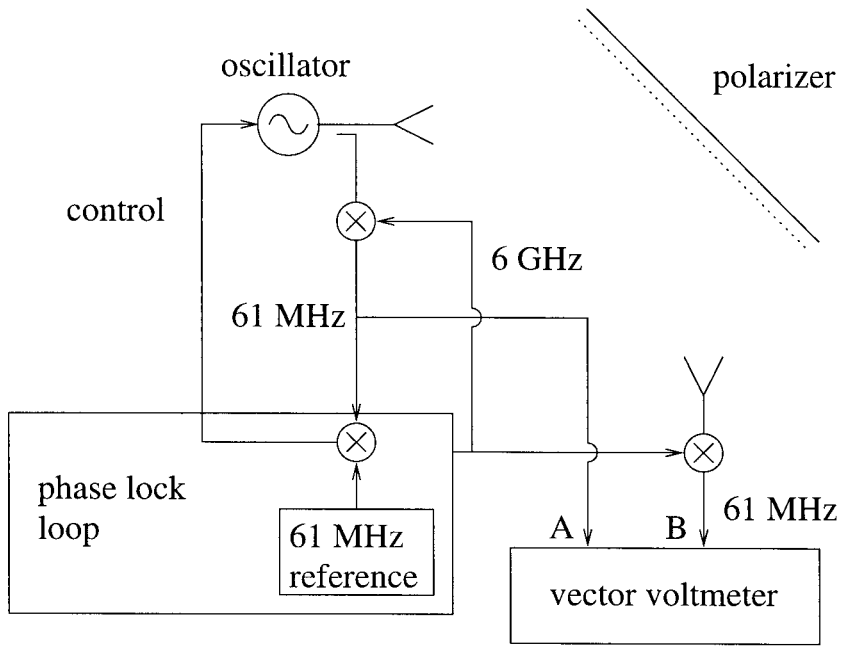

Figure 3.6: The schematic for the polarizer calibrator. The vector voltmeter measures the phase difference between the 61 MHz reference and output signals. If the spacing is set at a quarter-wave, this difference will change by exactly 90° for signal reflected from the grid compared to signals reflect from the mirror.

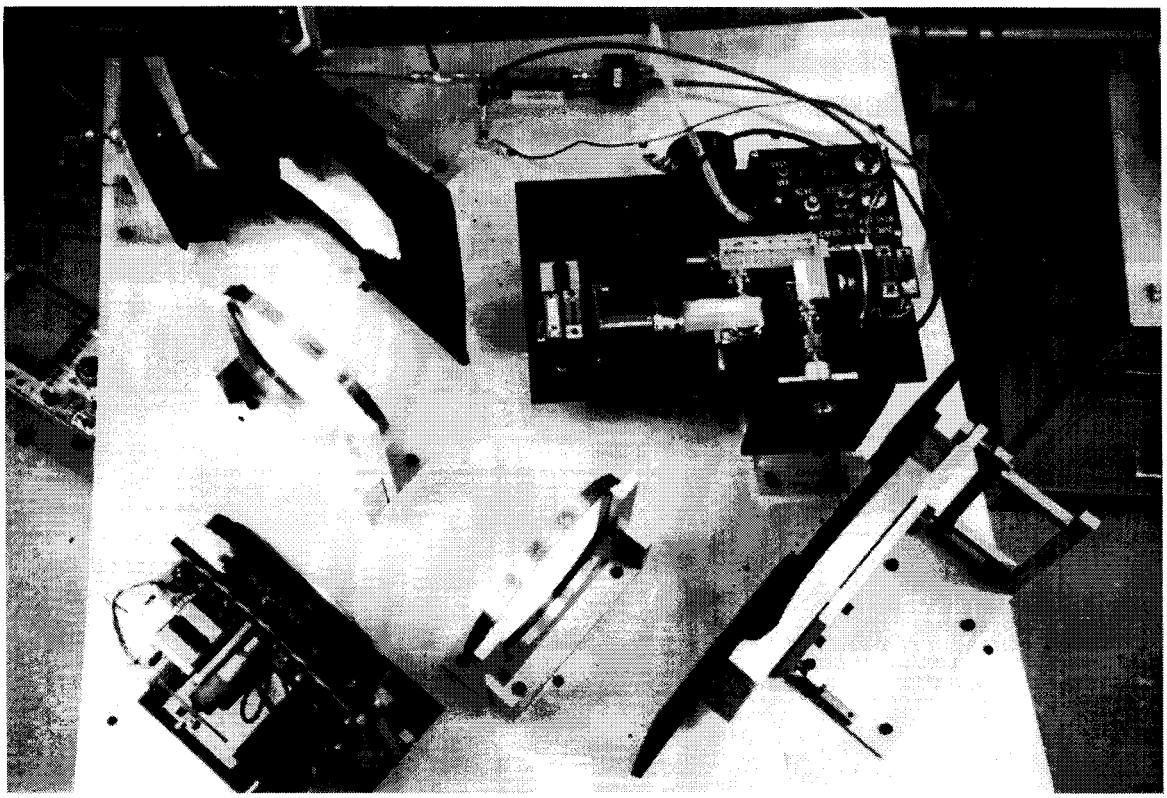

Figure 3.7: The assembled polarizer calibrator.

as expected for the change in the path length. However, when the grid is attached to the polarizer, the phase did not change as expected. This problem must be solved before the polarizers can be fully calibrated with this method.

3.5 Measured IP

As discussed in Chapter 4, the instrumental polarization measured astronomically varies from 1-3%. As the instrumental polarization measured for the same object derived from separate observations at the same frequency varies considerably, I believe that the majority of the instrumental polarization is due to the polarizers themselves, rather than the polarization properties of the telescopes.

Obvious sources of errors from the polarizers include the grid positions used. While the angle setting is repeatable, the error in the right and left circular positions

is probably around $\sim 0.3°$. One known problem is the stability of the grid-mirror spacing. Before the springs and washers were added to the polarizer design, the distance between the grid and the mirror (as measured by the LVT) could change by as much as 10 μm when the polarizer was rotated through the full range of angle. The addition of the springs and washers reduced this effect to less than 5 μm for all the polarizers, and the change between the left and right circular positions was typically 2 μm (0.4% instrumental polarization). As the same shift will occur in the calibration procedure, it is difficult to compensate for this problem. The grid-mirror spacing can not be changed on the integration time scale because the stepper motor and positioning algorithm are too slow, thus the same grid position must be used for right and left circular.

Chapter 4 Polarization software and data reduction

4.1 Observing

Polarization observing at OVRO utilizes the standard array observing program, CMA. The hardware parameters for the polarizers (wire grid angle and grid-mirror spacing offset) are set once and the grid-mirror spacing is calculated for the observing frequency and sideband. The possible observing modes are all polarizers with the wires parallel to the receiver polarization or assigning a circular polarization to each telescope. To completely characterize the polarized emission, the four correlations of right and left circular polarization, RR, LL, RL, and LR must be measured on each baseline. The polarization observing cycle for six antennas was created by randomizing the 64 possible polarization states in such a way that sets of polarizations (one each of RR, LL, RL, and LR) were completed for each baseline in roughly in the same time (Table 4.1). At the end of each cycle there are 16 complete measurements of the Stokes parameters for each baseline. The individual integrations are 1 minute and there are typically 4 integrations on the phase calibrator after every 16 integrations on the source.

4.2 General calibration procedure

The software to measure and correct for instrumental polarization is incorporated into the MMA data reduction package (Scoville et al., 1993) A flow chart for polarization reduction is shown in Figure 4.1 and a detailed description of the procedure, including the Fortran routine names is given in Appendix 1.

	Antenna							Antenna					
State #	1	2	3	4	5	6	State #	1	2	3	4	5	6
1	R	R	L	R	R	R	33	L	L	R	R	L	L
2	R	L	L	L	R	R	34	R	L	R	L	L	L
3	R	L	R	R	R	R	35	L	L	L	R	L	L
4	R	R	L	L	R	L	36	R	R	L	L	L	L
5	L	R	L	L	R	R	37	L	R	R	R	L	R
6	L	L	L	R	L	R	38	R	R	R	R	R	L
7	R	L	R	R	R	L	39	R	L	L	R	R	L
8	L	R	R	R	L	L	40	R	R	R	R	R	R
9	R	L	L	R	L	R	41	R	R	R	L	R	R
10	L	R	L	L	R	L	42	L	L	L	L	L	R
11	L	R	R	R	R	L	43	L	L	R	R	R	L
12	L	L	R	L	R	R	44	R	R	L	L	R	R
13	R	R	R	R	L	L	45	L	R	L	R	R	R
14	L	L	R	L	L	R	46	R	R	L	R	R	L
15	R	R	L	R	L	R	47	R	L	L	L	R	L
16	R	L	L	R	L	L	48	R	L	L	L	L	R
17	R	R	L	L	L	R	49	L	R	R	L	R	L
18	L	R	L	R	R	L	50	R	L	R	L	R	R
19	L	L	R	L	L	L	51	R	L	R	L	R	L
20	L	R	L	R	L	R	52	R	L	L	R	R	R
21	L	R	R	R	R	R	53	L	L	L	R	R	R
22	L	R	L	L	L	R	54	R	L	R	L	L	R
23	L	L	L	R	R	L	55	L	R	R	L	L	R
24	L	L	L	L	R	L	56	L	R	L	L	L	L
25	L	L	R	L	R	L	57	L	L	L	L	L	L
26	R	R	R	L	R	L	58	L	R	L	R	L	L
27	R	L	R	R	L	L	59	L	R	R	L	R	R
28	R	R	R	L	L	L	60	L	L	R	R	R	R
29	R	R	R	R	L	R	61	R	L	L	L	L	L
30	L	L	R	R	L	R	62	R	L	R	R	L	R
31	L	L	L	L	R	R	63	R	R	L	R	L	L
32	L	R	R	L	L	L	64	R	R	R	L	L	R

Table 4.1: The polarization (right or left circular) of each antenna in the randomized cycle of the 64 possible states.

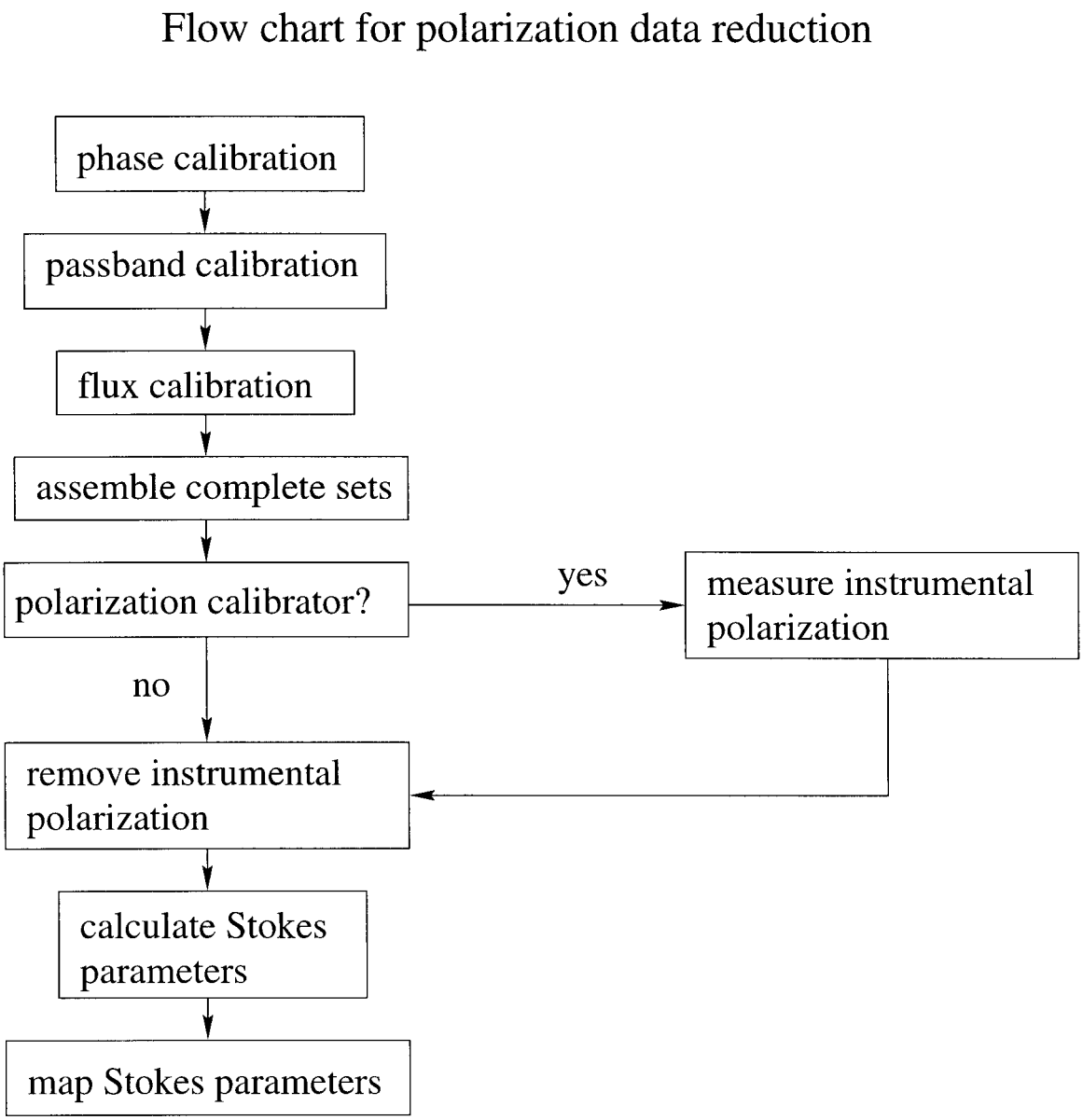

Figure 4.1: Flow chart for polarization data reduction.

The passband and gain calibration are derived and applied before the instrumental polarization is measured. The gain calibration removes the time dependence in the amplitude and phase caused by the atmosphere and gain variations due to changes in elevation. Accurate phase calibration is particularly critical in measuring the instrumental polarization as the fitting routine assumes all changes in the phase of the RL/LR correlations are due to intrinsic source polarization. In the antenna-based gain calibration, there are two available polarization options: 1) assume the source has equal amplitudes in the RR/LL correlations (i.e., no circular polarization) or 2) calibrate the RR/LL correlations separately and then calculate the complex gain calibration for the RL/LR terms from the right and left circular gains of each antenna. No evidence for significant circular polarization in the millimeter emission of the quasars used for gain calibration was found, so the first method was used for all sources. In a survey by Weiler and De Pater (1980) at 650 MHz, no quasars were observed to have circular polarization percentages above 0.5%. Also, circular polarization of synchrotron emission scales as $\nu^{-0.5}$ for constant magnetic field strength (Weiler and de Pater, 1980) and therefore the levels observed will be negligible at 100 GHz. The limits set by comparing the average amplitudes of the RR and LL correlations in my observations are circular polarization levels less than a few percent. The gain calibration can also be calculated from the baseline-based amplitudes and phases. Baseline-based calibration can only be done with the assumption of no circular polarization, as the complex gains for the RL/LR correlations can not be calculated without deriving the individual antenna gains.

To calibrate spectrometer data, the passband calibration was calculated using only the RR/LL correlations from the passband sources. Standard flux calibration using a planet or quasar was used. If a planet was observed in the track, those observations are used to calculate the fluxes of the quasars in the track. If no planet was present, the quasar fluxes are derived by averaging fluxes recorded by other observers. The error in the absolute flux calibration is due to uncertainty in the planet brightness temperatures and scatter in the data and is generally 20%.

After the gain, passband and flux calibrations have been applied, the integrations in each cycle of 64 are rearranged to form complete sets of RR, LL, RL, LR. This unscrambling facilitates deriving and correcting for the instrumental polarization terms. The baseline components (u, v, w), the integration time and the integration length are averaged over the four integrations for each baseline. This averaging is necessary when exporting the data from MMA (§4.5).

4.3 Measuring the instrumental polarization

There are several quantitative methods of describing the instrumental polarization. Using the notation of Conway and Kronberg (1969), I have defined the polarization response on the sky, which is elliptical if the instrumental polarization is non-zero, in terms of the sensitivity to the unwanted polarization, ϵ (the cross-coupling amplitude), and the cross-coupling phase, ϕ. The instrumental polarization terms when the polarizer is set for right circular polarization (i.e., the sensitivity to left circular polarization) will be designated by ϵ_R and ϕ_R. The OVRO telescopes have altitude-azimuth mounts, so the angle of the feed with respect to the sky – the parallactic angle – changes with hour angle. The measured source polarization will change with hour angle, while the instrumental polarization terms should be constant.

The measured voltage response of one telescope for the two circular polarization states in terms of the true electric field, E, and the cross-coupling terms is

$$\begin{aligned} V_R =& \frac{1}{(1+\epsilon_R^2)^{1/2}} E_R e^{i\chi_p} + \frac{\epsilon_R e^{-i\phi_R}}{(1+\epsilon_R^2)^{1/2}} E_L e^{-i\chi_p}, \\ V_L =& \frac{\epsilon_L e^{i\phi_L}}{(1+\epsilon_L^2)^{1/2}} E_R e^{i\chi_p} + \frac{1}{(1+\epsilon_L^2)^{1/2}} E_L e^{-i\chi_p}, \end{aligned} \tag{4.1}$$

where χ_p is the parallactic angle. The four parameters $\epsilon_R, \epsilon_L, \phi_R,$ and ϕ_L completely describe the instrumental polarization for each telescope. The correlations actually measured by the interferometer are $V_R V_R^*, V_L V_L^*, V_R V_L^*$, and $V_L V_R^*$.

As the parallactic angle changes, any linear source polarization will add a varying

amount to the circular correlations. I assume the cross-coupling amplitudes are small, allowing second order terms in ϵ to be ignored, and constant in time. The instrumental terms can be solved for by expressing the real and imaginary components of the circular correlations as functions of the parallactic angle, χ_p,

$$\begin{aligned}
V_{R_1}V_{R_2}^* &= |E_R|^2 + L[(\epsilon_{R_1}cos(\phi_{R_1}+2\phi_{pol}) + \epsilon_{R_2}cos(\phi_{R_2}+2\phi_{pol}))cos2\chi_p \\
&\quad +(-\epsilon_{R_1}sin(\phi_{R_1}+2\phi_{pol}) - \epsilon_{R_2}sin(\phi_{R_2}+2\phi_{pol}))sin2\chi_p] \\
&\quad +iL[(-\epsilon_{R_1}sin(\phi_{R_1}+2\phi_{pol}) + \epsilon_{R_2}sin(\phi_{R_2}+2\phi_{pol}))cos2\chi_p \\
&\quad +(-\epsilon_{R_1}cos(\phi_{R_1}+2\phi_{pol}) + \epsilon_{R_2}cos(\phi_{R_2}+2\phi_{pol}))sin2\chi_p], \\
V_{L_1}V_{L_2}^* &= |E_L|^2 + L[(\epsilon_{L_2}cos(\phi_{L_2}+2\phi_{pol}) + \epsilon_{L_1}cos(\phi_{L_1}+2\phi_{pol}))cos2\chi_p \\
&\quad +(-\epsilon_{L_2}sin(\phi_{L_2}+2\phi_{pol}) - \epsilon_{L_1}sin(\phi_{L_1}+2\phi_{pol}))sin2\chi_p] \\
&\quad +iL[(-\epsilon_{L_2}sin(\phi_{L_2}+2\phi_{pol}) + \epsilon_{L_1}sin(\phi_{L_1}+2\phi_{pol}))cos2\chi_p \\
&\quad +(-\epsilon_{L_2}cos(\phi_{L_2}+2\phi_{pol}) + \epsilon_{L_1}cos(\phi_{L_1}+2\phi_{pol}))sin2\chi_p],
\end{aligned} \tag{4.2}$$

$$\begin{aligned}
V_{R_1}V_{L_2}^* &= (\epsilon_{L_2}cos\phi_{L_2}|E_R|^2 + \epsilon_{R_1}cos\phi_{R_1}|E_L|^2) + (Lcos2\phi_{pol})cos2\chi_p \\
&\quad +(-Lsin2\phi_{pol})sin2\chi_p \\
&\quad +i[(-\epsilon_{R_1}sin\phi_{R_1}|E_L|^2 - \epsilon_{L_2}sin\phi_{L_2}|E_R|^2) + (Lsin2\phi_{pol})cos2\chi_p \\
&\quad +(Lcos2\phi_{pol})sin2\chi_p], \\
V_{L_1}V_{R_2}^* &= (\epsilon_{L_1}cos\phi_{L_1}|E_R|^2 + \epsilon_{R_2}cos\phi_{R_2}|E_L|^2) + (Lcos2\phi_{pol})cos2\chi_p \\
&\quad +(-Lsin2\phi_{pol})sin2\chi_p \\
&\quad +i[(\epsilon_{R_2}sin\phi_{R_2}|E_L|^2 + \epsilon_{L_1}sin\phi_{L_1}|E_R|^2) + (-Lsin2\phi_{pol})cos2\chi_p \\
&\quad +(-Lcos2\phi_{pol})sin2\chi_p],
\end{aligned} \tag{4.3}$$

where $L = |E_R E_L^*|$ is the source linear polarization, ϕ_{pol} is the polarization angle and the numeric subscripts refer to the two telescopes. In the RR and LL correlations, the source linear polarizations terms are multiplied by ϵ, and so the change in these correlations will be quite small for low instrumental polarization. An alternative

way to express the cross terms is to correct for the effect of the parallactic angle, which changes only the phase and not the amplitude. In this case, the instrumental polarization terms will change with parallactic angle,

$$\begin{aligned}
V_R V_L^* = L cos2\phi_{pol} &+ (\epsilon_{L_2} cos\phi_{L_2} |E_R|^2 + \epsilon_{R_1} cos\phi_{R_1} |E_L|^2) cos2\chi_p \\
&- (\epsilon_{L_2} sin\phi_{L_2} |E_R|^2 + \epsilon_{R_1} sin\phi_{R_1} |E_L|^2) sin2\chi_p \\
+i[L sin2\phi_{pol} &- (\epsilon_{L_2} sin\phi_{L_2} |E_R|^2 + \epsilon_{R_1} sin\phi_{R_1} |E_L|^2) cos2\chi_p \\
&- (\epsilon_{L_2} cos\phi_{L_2} |E_R|^2 + \epsilon_{R_1} cos\phi_{R_1} |E_L|^2) sin2\chi_p], \\
V_L V_R^* = L cos2\phi_{pol} &+ (\epsilon_{L_1} cos\phi_{L_1} |E_R|^2 + \epsilon_{R_2} cos\phi_{R_2} |E_L|^2) cos2\chi_p \\
&- (\epsilon_{L_1} sin\phi_{L_1} |E_R|^2 + \epsilon_{R_2} sin\phi_{R_2} |E_L|^2) sin2\chi_p \\
+i[L sin2\phi_{pol} &+ (\epsilon_{L_1} sin\phi_{L_1} |E_R|^2 + \epsilon_{R_2} sin\phi_{R_2} |E_L|^2) cos2\chi_p \\
&+ (\epsilon_{L_1} cos\phi_{L_1} |E_R|^2 + \epsilon_{R_2} cos\phi_{R_2} |E_L|^2) sin2\chi_p].
\end{aligned} \tag{4.4}$$

As expected, the instrumental terms measured with and without the parallactic angle correction are the same, to within the uncertainties in the fitting procedure.

To adequately measure the instrumental polarization, I observed an unresolved linearly polarized source through a wide range of parallactic angle ($> 60°$) or an unpolarized source for a few hours. In the fitting routine, the baseline amplitudes and phases are converted into real and imaginary components as a function of the parallactic angle. In practice, the corruption of the RR and LL correlations by the cross-coupling amplitude multiplied by the source polarization is too small to be measured given the typical amplitude and phase errors. Generally the quasars used have linear polarization percentages less than 10%, so for a cross-coupling amplitude of 0.03, the RR and LL correlations change by less than 0.3%. The scatter in the real component of the data from phase noise and calibration uncertainties is considerably larger than this. In the calibration procedure the real components of the RR and LL correlations are fit by a constant and the imaginary components are not fit at all (Figure 4.2). For the level of millimeter continuum linear polarization measured for quasars, an average imaginary component that is significantly different from zero

would indicate improper phase calibration rather than high source polarization. The RL and LR correlations are fit with a least squares routine to equation [4.3]. The instrumental polarization is solved for in terms of $\epsilon cos\phi$ and $\epsilon sin\phi$ by assuming that $|E_R|^2 = |E_L|^2 = |V_R|^2 = |V_L|^2$. This relies on the assumptions of no circular polarization and that second-order terms in L and ϵ for V_{RR} and V_{LL} are small enough to be set to 0.

For data with no noise, it is possible to accurately fit for both the source polarization and the instrumental terms at the same time. However, for real data, the errors from phase calibration are large enough to affect the fits. The best procedure when using a quasar to measure the instrumental polarization is to run the fitting routine twice. The first time, the measurement of the true source linear polarization is slightly different on each baseline due to the noise. The average of the baseline measurements is taken to be the source polarization for the second pass, and the fitting routine is constrained to fitting only for the instrumental polarization terms. Using an unpolarized source, such as Neptune or Uranus, as the polarization calibrator, L is immediately set to 0. While it is more accurate to measure the instrumental terms using an unpolarized source, the disadvantage in practice is that the planets are weaker than the brightest quasars and are resolved on the longest baselines. Slightly resolved planets can be used if the amplitude is divided by the visibility before the instrumental polarization is measured.

An additional source of polarization calibrators is the linearly polarized emission from SiO masers. However, these masers can be strongly polarized, so the second order terms in equation 2 can become significant. The advantage is that for some sources, particularly the SiO maser in Orion, the polarized emission is much brighter than the brightest quasar. In the calibration procedure the spectrometer channels containing significant polarized emission are combined and fit as above. Using a polarized maser as the calibration source is limited to observations at the maser frequency.

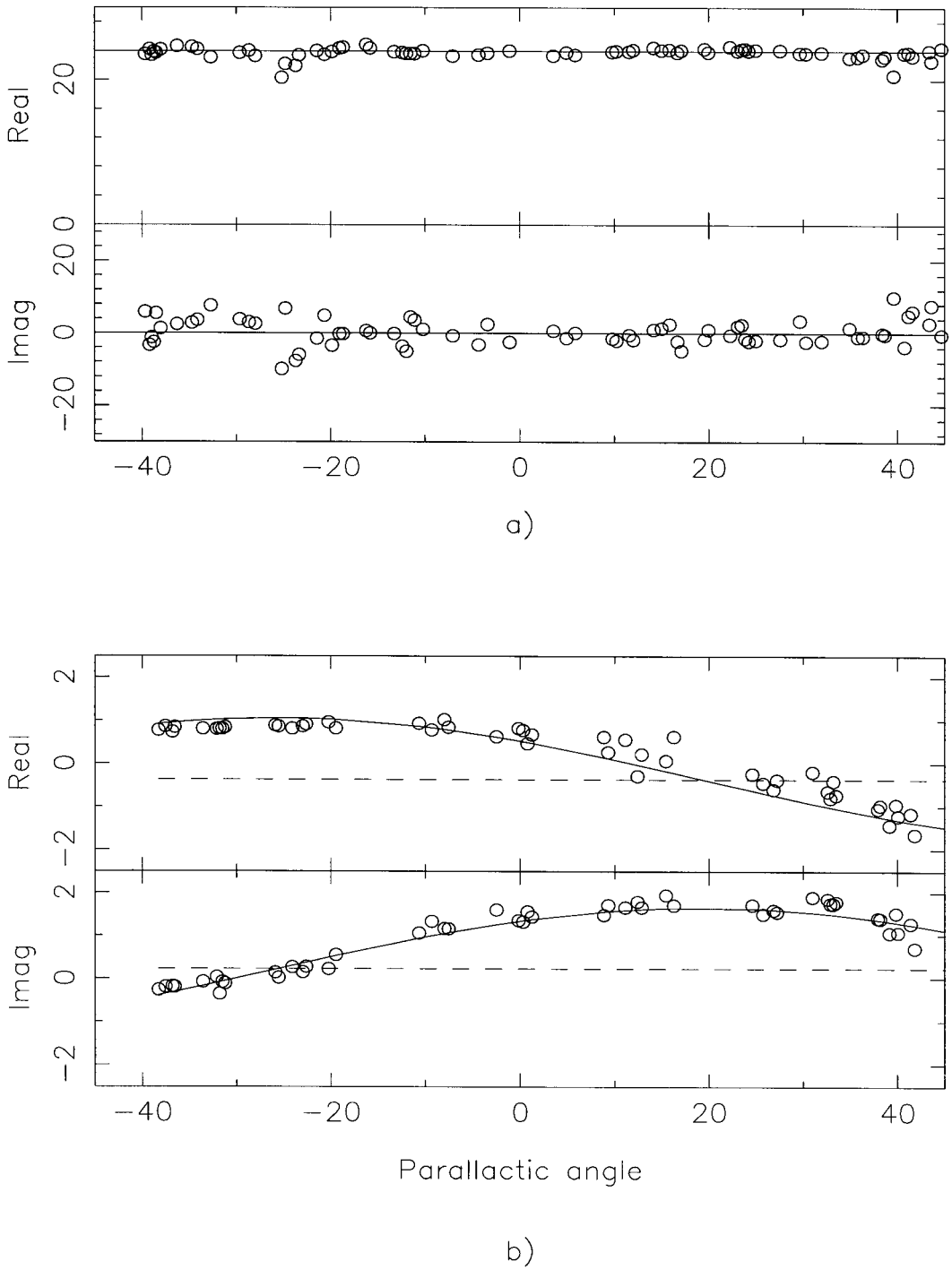

Figure 4.2: Example output from the instrumental polarization fitting routine for the linearly polarized source 3C279. The real and imaginary components of the RR(a) and RL(b) components are plotted along with the fits. For the RL components the contribution from the instrumental polarization is plotted as a dashed line.

4.4 Correcting for the instrumental polarization

After the instrumental terms have been measured using a bright quasar or planet, the source data is corrected for these terms. Generally, the observations of the calibrator are taken immediately before or after the source to reduce the effects of any time varying terms in the instrumental polarization, if they exist. Only the RL and LR correlations are corrected for the instrumental terms using,

$$\begin{aligned} V_{R_1}V_{L_2}^* &= V_{R_1}{}^{*'}_{L_2} - (\epsilon_{R_1}cos\phi_{R_1} + \epsilon_{L_2}cos\phi_{L_2})|E_R|^2 + i(\epsilon_{R_1}sin\phi_{R_1} + \epsilon_{L_2}sin\phi_{L_2})|E_R|^2, \\ V_{L_1}V_{R_2}^* &= V_{L_1}{}^{*'}_{R_2} - (\epsilon_{L_1}cos\phi_{L_1} + \epsilon_{R_2}cos\phi_{R_2})|E_R|^2 - i(\epsilon_{L_1}sin\phi_{L_1} + \epsilon_{R_2}sin\phi_{R_2})|E_R|^2, \end{aligned} \tag{4.5}$$

where the primed quantities are measured correlations. $|E_R|^2$ (assumed equal to $|E_L|^2$) is calculated by averaging the parallel correlations for that baseline over a specified length of time. This smoothing time is chosen such that the effects of changing amplitudes as the baseline length changes are minimized and there are enough individual integrations to accurately measure the total intensity. A typical value for a slightly resolved source is 20 minutes. The data are visually inspected and this averaging time is adjusted accordingly. One method of automating this would be to average until the baseline components u and v have changed by a given amount.

4.5 Stokes parameters and mapping

After the calibration is completed, including removal of the instrumental polarization, the Stokes parameters are calculated using:

$$\begin{aligned} I &= \frac{1}{2}(V_{RR} + V_{LL}), \\ V &= \frac{1}{2}(V_{RR} - V_{LL}), \\ Q &= \frac{1}{2}(V_{RL}e^{-2i\chi_p} + V_{LR}e^{2i\chi_p}), \\ U &= \frac{-i}{2}(V_{RL}e^{-2i\chi_p} - V_{LR}e^{2i\chi_p}). \end{aligned} \tag{4.6}$$

The factor of 1/2 appearing in these equations which is not part of the standard definition of the Stokes parameters is from the convention imposed by receivers with only one polarization state. The usual practice is to assume that whatever correlation is measured, cross-correlated circular or linear, is equivalent to the total intensity. This is true for any source with no polarization, and is approximately true for any source with low levels of either linear or circular polarization. The factor of 1/2 adjusts the true Stokes parameters to the usual total intensity measured by the array, which is used in the gain and flux calibration.

To export the data from MMA, it is converted into FITS format. This can be done for either circular correlations or true Stokes parameters. However, even if circular correlations are used, only maps of Stokes parameters, which are intrinsically real quantities, are made. In the FITS file, the time, integration length, u, v, and w are averaged for each set of circular correlations or Stokes parameters. This is necessary for maps to be made in AIPS or DIFMAP. The averaging in u, v, and w will mimic the smearing effect caused by time averaging in one integration. The data will be slightly smeared, resulting in a loss of amplitude. The typical averaging in u and v corresponds to a time change of approximately 10 minutes. For a source 5″ from the phase center with 3″ resolution, the loss in amplitude is only 0.12% (Perley et al., 1989). A map of each Stokes parameter is made separately. The linear polarization map is made by combining Q and U in the map plane to create L and ϕ_{pol}, where

$$L = \sqrt{Q^2 + U^2} \qquad \text{and}$$

$$\phi_{pol} = \frac{1}{2}\tan^{-1}\left(\frac{U}{Q}\right).$$

The uncertainty in the linear polarization map is a combination of the thermal noise ($\sigma_Q = \sigma_U$) and any uncorrected instrumental polarization.

I estimated the residual instrumental polarization by correcting one observation of Neptune (assumed unpolarized) with the instrumental polarization terms derived from the previous day's observations. The residual instrumental polarization mea-

sured was 0.7% of the total intensity. This residual is due to any time-varying terms in the instrumental polarization and the errors in measuring the instrumental polarization. If the time-varying terms are the dominant component in this residual, then the 0.7% measured will be an upper limit for the residual for most sources, as the calibration data is usually taken within a few hours of the source data and the polarizer settings are not changed. Typical values for the total instrumental polarization at the phase center are 1-3% for the data presented in Chapter 6. The error in the source linear polarization is estimated by combining (in quadrature) the rms error from the Q and U maps and the residual instrumental polarization scaled by the source total intensity.

As the linear polarization is an intrinsically positive quantity, the error distribution will have a Rice distribution, rather than the Gaussian distribution expected for Q and U. Thus, for low signal-to-noise measurements, the measured polarization will be an overestimate of the true polarization. There are several methods to estimate the true polarization from the observations and the measured noise in Q and U (Simmons and Stewart, 1985; Leahy and Fernini, 1989). The estimator utilized by the AIPS task COMB is

$$L_o = \sqrt{L^2 - \sigma^2}, \tag{4.7}$$

where L_o is the estimated polarization, L is the observed polarization, and σ is the standard deviation in Q and U, assumed to be equal. For observed polarizations less than σ, the estimated polarization is set to 0. This method slightly underestimates the polarization for signal to noise ratios of 1 to 3, but is considerably better than no correction (Leahy and Fernini, 1989). For signal to noise ratios of 4 or greater, the estimator and true polarization agree almost exactly.

Chapter 5 Observations

5.1 Sources

The sources observed in this project (aside from Orion IRc2) are low mass young stellar objects. I chose to concentrate on low mass objects rather than high mass objects for several reasons. The millimeter continuum emission from low mass protostars is dominated by emission from dust grains, with no significant contribution from free-free emission. In molecular clouds where primarily low mass stars are being formed, the individual objects tend to be isolated rather than in clusters (Shu et al., 1987). Thus in clouds such as Taurus, Ophiuchus and Perseus, the individual objects can be resolved by the OVRO interferometer, though some systems may be unresolved binaries. At the distances to these clouds (150-350 pc), a ~1000 AU envelope subtends 3-6″. An additional advantage of observing low mass systems is that most of the theoretical work on collapse of a magnetized core is for cores which form ~1 $M_\odot$ stars. The objects observed in this study of the magnetic field structure in young stellar objects are NGC 1333/IRAS4A, IRAS 16293-2422, L1551-IRS 5, and Orion IRc2. The field center coordinates used in the observations and the distance to each object are given in Table 5.1.

Source	distance (pc)	RA (1950)	dec (1950)	L_{bol}	S_ν(3mm)
IRAS4A	350	03:26:04.96	31:03:13.1	15 $L_\odot$	270 mJy
I16293	160	16:29:20.85	-24:22:14.0	30 $L_\odot$	550 mJy
IRc2	450	05:32:47.03	-05:24:23.9	10^5 $L_\odot$	1.1 Jy
L1551	140	04:28:40.20	18:01:41.0	30 $L_\odot$	100 mJy

Table 5.1: Coordinates and distances used for objects discussed in text. The 3 mm fluxes given are from the OVRO observations.

Two of the three low mass objects observed (IRAS 4A and IRAS 16293) fall into the 'Class 0' category proposed by Andre et al. (1993). These sources are characterized by having more mass in the surrounding envelope than in the protostar. Other properties are that the emission from the source can be fit with a single-temperature blackbody and the central source is not visible at optical and near-infrared wavelengths. The strong sub-millimeter fluxes observed from class 0 sources suggest more massive envelopes than those surrounding older objects. These large envelopes may correspond to the magnetically supported 'pseudodisks' discussed in Chapter 1. Thus, the environments of deeply embedded objects are ideal locations in which to study the role of magnetic fields in the star formation process. The Orion KL/IRc2 region is one of the most studied regions of molecular gas and high mass star formation. Orion IRc2 is a high mass young stellar object and has been the object of several polarization studies at far-infrared and sub-millimeter wavelengths (§5.1.3).

5.1.1 NGC 1333/IRAS 4A

The molecular cloud complex L1450 in Perseus contains the active star forming region NGC 1333. Distance estimates for this cloud vary by a factor of 2, with a recent measurement of 220 pc (Cernis, 1990). To be consistent with previous studies, a distance of 350 pc (Herbig and Jones, 1983) is used here. This cloud contains several young stellar objects characterized by compact infrared sources and associated bipolar outflows. IRAS 4 was first detected by H_2O maser emission (Haschick et al., 1980), though no infrared source was identified at this position until the analysis of IRAS (Infrared Astronomical Satellite) data by Jennings et al. (1987). Detection of CO line emission wings, indicating the presence of an outflow, provided further evidence that IRAS 4 was a young stellar object (Liseau et al., 1988). Higher resolution sub-millimeter observations revealed two sources within the IRAS beam (Sandell et al., 1991). IRAS 4A is part of a wide (~10,000 AU) double system, in which both

components power a molecular outflow (Blake et al., 1995). The outflow powered by IRAS 4A is well collimated over scales of 2′. The outflow position angle is ∼45° over large scales, but is directed almost north-south closer to the central source (Figure 5.1).

IRAS 4A has not been detected at wavelengths shorter than the far-infrared and is thus considered a class 0 source. Mass estimates of the envelope surrounding IRAS 4A, derived from sub-millimeter and millimeter continuum fluxes, range from 3 to 9 $M_\odot$ (Sandell et al., 1991; Blake et al., 1995). The bolometric luminosity and effective temperature derived from far-infrared and sub-millimeter fluxes are 15 $L_\odot$ and 37 K (Sandell et al., 1991). The continuum flux at 2 cm and 7 mm is consistent with emission from dust, with no contribution from free-free emission (Mundy et al., 1996). Recent sub-millimeter observations by Lay et al. (1995) with the CSO-JCMT interferometer found that IRAS 4A is a 1.8″ binary at a position angle of 130°.

Single-dish sub-millimeter polarization measurements have been made for both IRAS 4A and 4B at 800 μm by Minchin et al. (1995). They found a continuum polarization for IRAS 4A of 3.2 ± 0.3% in a 14″ beam with a measured polarization angle of 132 ± 3°. Polarization observations have also been made by Tamura et al. (1995) at 1.1 mm with a 19″ beam. Their result of 4.6 ± 0.8% polarization with a position angle of 145 ± 5° is roughly consistent with the 0.8 mm observation given the different beam sizes.

5.1.2 IRAS 16293-2422

IRAS 16293-2422 lies at a distance of 160 pc in the eastern streamer region of the Ophiuchus molecular cloud. Observations of dense molecular gas at the position of the IRAS source and high-velocity CO wings indicative of an outflow suggested this source was a highly embedded young stellar object (Walker et al., 1986; Mundy et al., 1986). Radio continuum observations by Wootten (1989) first detected two distinct sources, separated by ∼5″, within the dense core. The northwestern source, 1629B,

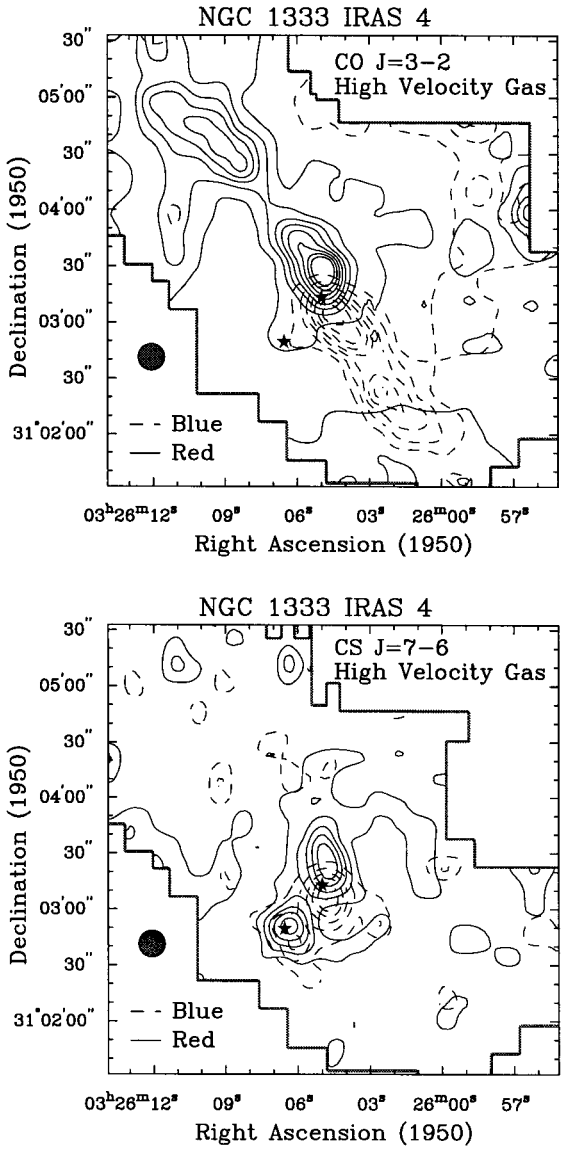

Figure 5.1: The IRAS 4 outflow as traced in high velocity gas from Blake et al. (1995) demonstrating the change in position angle. The stars mark the continuum positions of IRAS 4A (northwest source) and IRAS 4B (southeast).

was unresolved and weaker than the southeastern source, 1629A. High resolution observations at centimeter wavelengths revealed two components toward source A (Wootten, 1989). The radio continuum spectral index of 1629A was observed to be 0.6 $\pm$0.1 and is consistent with an ionized outflow (Estalella et al., 1991). Thus, the two emission peaks in 1629A trace the ionized gas on either side of the outflow.

High resolution millimeter observations resolved the dust continuum emission around the two radio sources (Figure 5.2). An extended envelope with major axis at approximately the position angle of the binary surrounds both sources, though the dust emission peaks on each source (Mundy et al., 1992; Walker et al., 1993). At 3 mm 1629B has a higher continuum flux than 1629A, however stronger molecular line emission is seen toward 1629A (Mundy et al., 1992; Walker et al., 1993). Ammonia maps by Mundy et al. (1990) trace a very extended (8000 AU) elongated structure with the same position angle as the circumbinary disk. As IRAS 16293 is not visible in the optical or near-infrared, it is also considered to be a class 0 source.

Single dish observations of the high velocity CO emission revealed four outflow lobes emanating from the dense core, blue-shifted lobes to the east and southwest and red-shifted lobes to the northeast and west (Walker et al., 1988). If the lobes comprise two separate outflows, the axes are at position angles of 50° and 95°. Walker et al. (1993) observed that 1629A dominated the CS line wing emission and suggested that it is in a later stage of evolution than 1629B and is currently powering the outflow with the 50° position angle. The bolometric luminosity ($\sim$ 30 $L_\odot$) and derived dust masses for each source (0.4–0.8 $M_\odot$) indicate that these sources are forming low mass young stellar objects and that much of the luminosity is derived from accretion (Mundy et al., 1992; Walker et al., 1993).

Two measurements of the 1 mm polarization toward IRAS 16293 have been made with single-dish telescopes. Flett and Murray (1991) observed IRAS 16293 at 0.8 mm and detected a polarization of 1.4% $\pm$ 0.5% at a position angle of 62° $\pm$ 11°. The observations of Tamura et al. (1993) were at a slightly longer wavelength, 1.1 mm, but detected 2.8% $\pm$ 0.5% at a position angle of 144° $\pm$ 5°. With resolutions of 11″

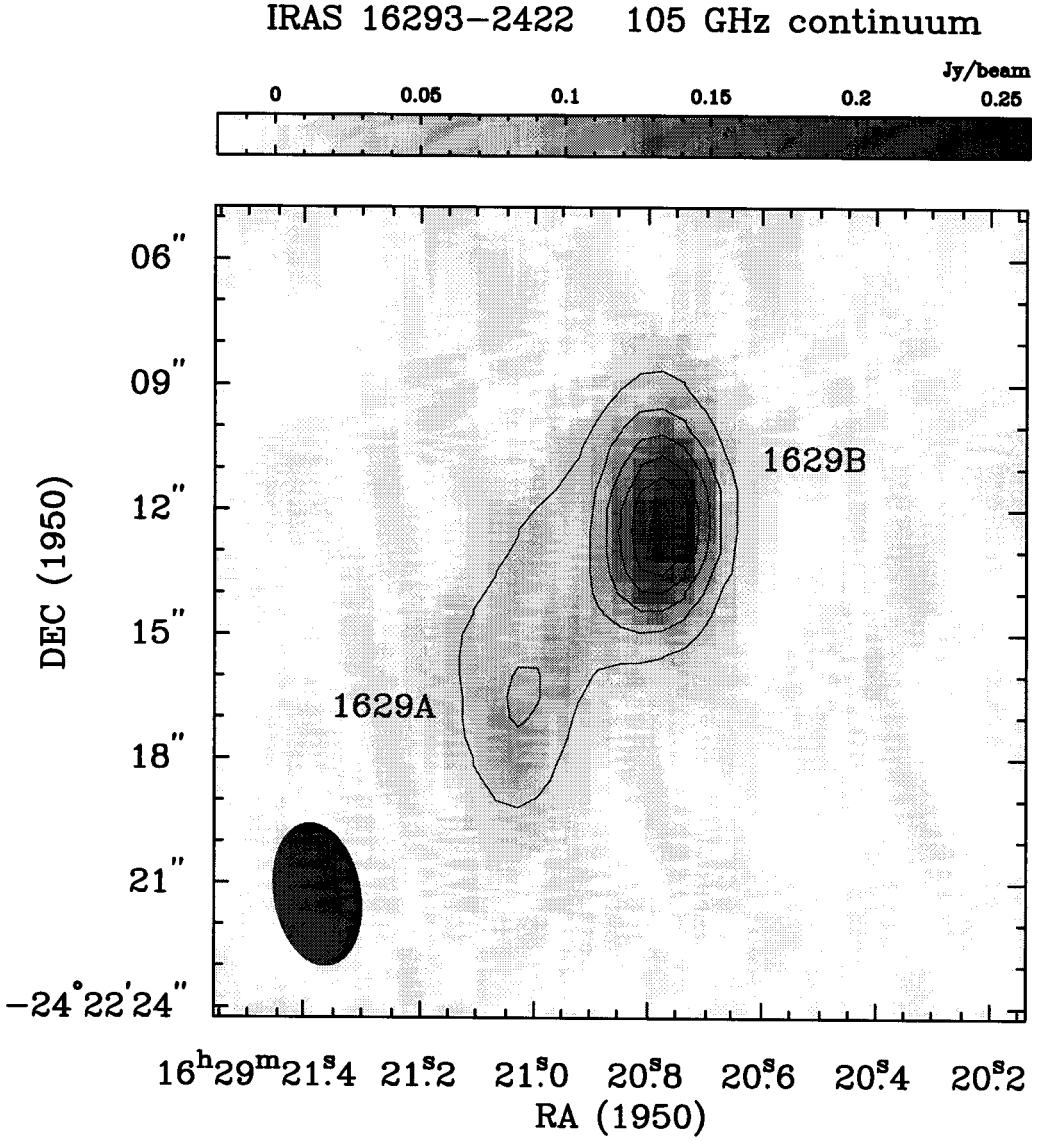

Figure 5.2: The continuum image of IRAS 16293-2422 at 105.6 GHz from my OVRO data. Uniform weighting was used, with a beam size of $3''.5 \times 2''.1$. The contours level are 40 mJy beam^{-1} and the rms noise in the map is 5 mJy beam^{-1}.

and 19″ respectively, both measurements were incapable of resolving the continuum emission from the two sources. If both measurements are correct, the large change in position angle (85°) between the two wavelengths is difficult to explain. The different position angles observed can not be explained by Faraday rotation between the two frequencies used (see Chapter 2). One possible explanation is that if the higher frequency (0.8 mm) observations are tracing absorption by dust and the 1.1 mm observations are tracing emission, a 90° phase difference is expected. However, given the long wavelength and large beam, it is unlikely that the 0.8 mm polarization is due to selective absorption.

5.1.3 Orion IRc2

The Orion molecular cloud is the nearest and most studied site of active high mass star formation (see review by Genzel and Stutzki, 1989). The Orion KL region contains several high luminosity infrared sources and a massive bipolar outflow. The total luminosity of the region is 10^5 $L_\odot$ (Genzel and Stutzki, 1989). A roughly north-south concentration of dense material (the hot core) lies near the most luminous infrared source, IRc2. While IRc2 was proposed as the driving source of the outflow, radio observations revealed radio continuum emission (source I) offset ~1″ from IRc2 (Menten and Reid, 1995). IRc2 is not self-luminous but is a dense clump in the hot core. A schematic of the region is given in Figure 5.3. Further evidence that source I is a high mass young stellar object includes the ring of SiO maser emission that surrounds the central source at a radius of 40 AU (Plambeck et al., 1990). The derived rotation and expansion of the maser emission suggest the presence of a disk. High resolution millimeter observations have constrained the dust mass of any disk around I to be less than 0.4 $M_\odot$ (Plambeck et al., 1995). For convenience, I will continue to use the term IRc2 to refer to the central luminous source and the hot core. The nearby infrared source BN is now thought to be a runaway B star which originated elsewhere in the molecular cloud (Plambeck et al., 1995).

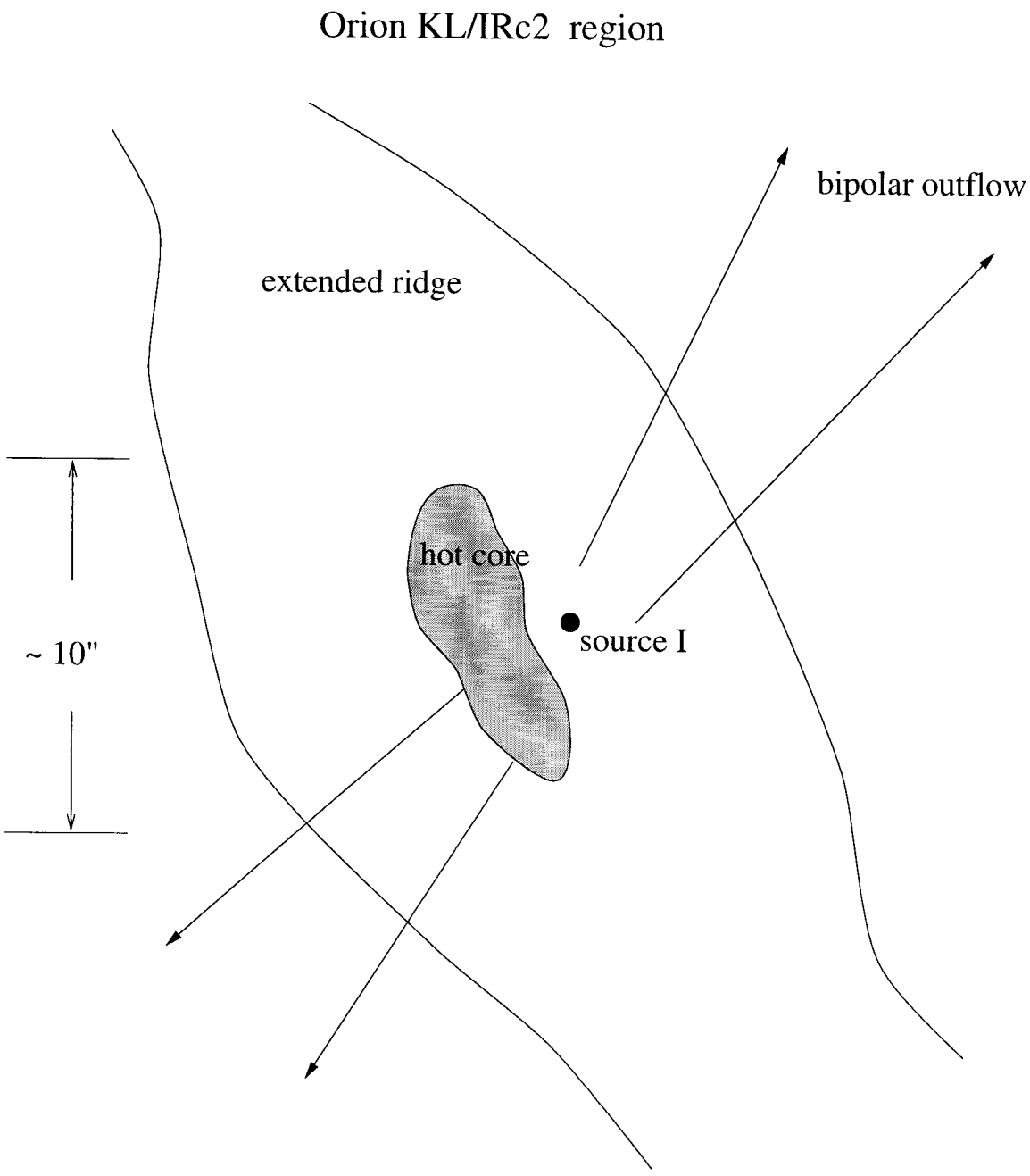

Figure 5.3: Cartoon of the structures in the Orion KL/IRc2 region.

Many polarization observations have been made of the Orion IRc2 region. A list of the far-infrared and submillimeter polarization results is given in Table 5.2. Despite the large range in wavelength and in beam size, there is general agreement about the strength of the polarization and the angle. The position angles measured are roughly perpendicular to the angle of the bipolar outflow. Two of these studies have mapped the polarization over many positions near Orion IRc2. Leach et al. (1991) observed 15 positions at 1.3 mm with a 30″ beam. The average percentage polarization observed was 4.6% and a polarization of 7.9% was measured in one location. However, the polarization at the position centered on Orion IRc2 was only 2.7%, the second lowest value in the sample. This 'polarization hole' was also observed in observations at 100 and 450 μm (Schleuning et al., 1996) and is shown in Figure 5.4. The high levels of polarization seen within 0.1 pc of Orion IRc2 are some of the largest polarization values observed for emission from grains for any source. This suggests that the magnetic field is aligned roughly in the plane of the sky and conditions for grain alignment are nearly optimal.

Wavelength (μm)	telescope	beam (″)	pol. (%)	pol. angle	reference
100	KAO	60	1.7±0.2	22±4	Novak et al. (1989)
100	KAO	35	1.1±0.05	31±2	Schleuning et al. (1996)
270	KAO	60	1.7±0.2	24±6	Dragovan (1986)
350	CSO	14	1.2±0.1	32±2	Schleuning et al. (1996)
450	JCMT	8	0.6±0.2	44±10	Flett and Murray (1991)
800	JCMT	13	1.2±0.2	44±5	Flett and Murray (1991)
1100	JCMT	18	1.3±0.1	35±3	Flett and Murray (1991)
1300	FCRAO	25	2.6±0.8	40±8	Novak et al. (1990)
1300	NRAO	30	2.7±0.3	34±3	Leach et al. (1991)

Table 5.2: List of far infrared and sub-millimeter polarization observations of the Orion IRc2 region.

Proposed explanations for the decreased polarization observed towards the region of greatest activity include collisional de-alignment of grains at high densities, spherical grain growth at high densities, inclination of the magnetic field near Orion IRc2

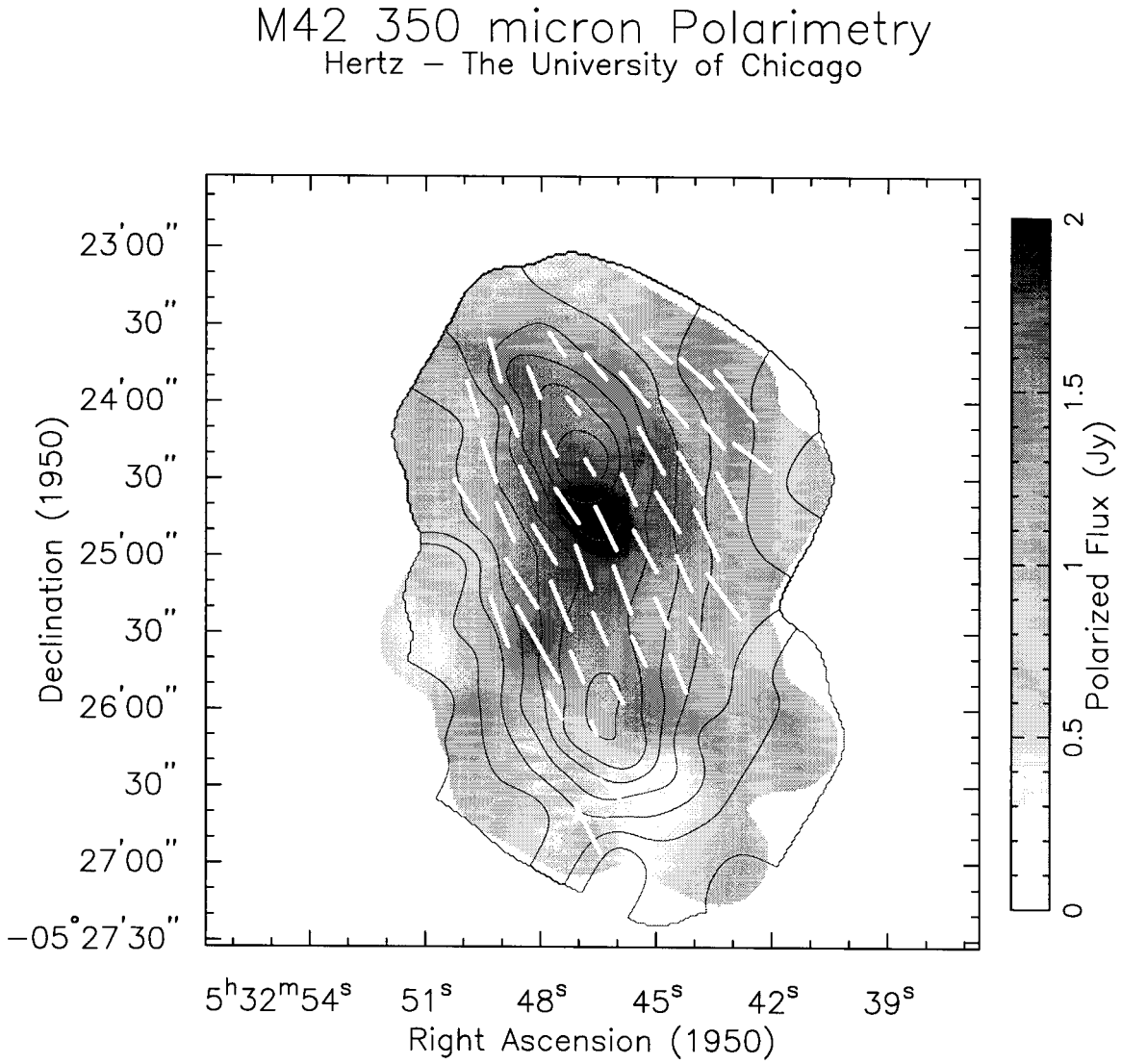

Figure 5.4: The polarization of Orion at 350 μm from Schleuning et al. (1996). The contours are the total intensity, the grey scale is the polarized emission and the vectors represent the polarization position angle and percentage at each position observed. The beam used is 18″.

towards the line of sight, and tangling of the magnetic field on scales small compared to the beam size (Leach et al., 1991). With the resolution provided by the millimeter interferometric observations, I can look for indications of field tangling.

5.1.4 L1551-IRS 5

L1551-IRS 5 is a deeply embedded young stellar object in the Taurus molecular cloud (d $\sim$ 140 pc),but may be more evolved than IRAS 4A and IRAS 16293 as the source is visible in the near infrared. Millimeter continuum observations (Keene and Masson, 1990; Lay et al., 1994) revealed a compact accretion disk with a radius $\sim$ 50 AU. L1551-IRS 5 powers an optical jet and a bipolar molecular outflow. Molecular line observations by Sargent et al. (1988) revealed a large ($\sim$1500 AU) structure perpendicular to the outflow. Tamura et al. (1995) report a detection of linear polarization toward L1551 of $3.3 \pm 0.6\%$ at 1.1 mm which they claim is 'marginal'. However, their observations at 0.8 mm did not detect any linear polarization, with a limit of $0.2 \pm 0.5\%$. The non-detection of the source at 0.8 mm can possibly be explained if it corresponds to the wavelength transition between absorption and emission, at which there will be a null in the polarization. However, given the long wavelengths and extended emission towards this source, this explanation is unlikely. I obtained 3 mm polarization data for L1551 at a resolution of 6″. No linear polarization was detected, and due to the low continuum flux for this source ($\sim$ 100 mJy), the limits set by the interferometric observations ($3\sigma \simeq 5\%$) are higher than the reported single dish measurements. As the upper limit set does not place significant constraints on the polarization of the source, these data are not discussed further.

5.2 Observations

All polarization tracks presented here were taken at the OVRO mm array between October 1994 and May 1996 with six telescopes. The list of tracks discussed in Chapter 6 is summarized in Table 5.3. One track refers to observations of one source

Source	track #	date	configuration	freq(GHz)	# of ints[a]	IP soln #
IRAS 4A	1719	10/25/94	low[b]	86.243	286	6
	2002	3/7/95	eq[c]	86.243	323	19
	2042	3/27/95	eq	86.243	286	18
	2639	2/26/96	high[d]	86.243	309	17
IRAS 16293	2683	2/26/96	eq	105.600	156	21
	2729	3/16/96	high	105.600	153	22
	2814	4/22/96	low	105.600	152	23
	2859	5/9/96	low	105.600	161	24
Orion IRc2	2453	11/19/95	low	105.600	241	14
	2731	3/16/96	high	105.600	233	22
L1551-IRS5	2457	11/20/95	low	105.600	304	15
	2607	1/24/96	low	105.600	169	16

Table 5.3: All polarization tracks.

[a] each integration is 1 minute

[b] telescope positions in meters: 80N, 50W, 50E, 65W, 80N, 30N

[c] 180N, 40N, 100E, 100W, 140N, 60N

[d] 220N, 65W, 100E, 100W, 140N, 30N

transit (usually ~8 hours) including the gain, passband, and flux calibrators. The IRAS 4A tracks were taken with the continuum passband centered on SiO(2-1) at 86.243 GHz because some of the first tracks used an SiO maser as instrumental calibration sources. The remaining data were taken with a center frequency of 105.600 GHz. This frequency was chosen specifically to have as little molecular line emission as possible in the range of frequencies at which the OVRO receivers have low system temperatures and the atmosphere opacity is not too high. The tracks were reduced using the software described in Chapter 4. A detailed description of the reduction of one track is given below.

5.2.1 Reduction details for a single track

The source NGC 1333/IRAS 4A was observed on October 25, 1994, in track 1719. The phase calibrators used were 0234+285 and 3C84. The fluxes derived for 0234+285 and 3C84 were 1.5 and 5.5 Jy, respectively. The phase coherence was generally good except for a period of rapid variation in phase lasting 30 minutes on antenna 6; these data were removed. Antenna based phase calibration was used.

The polarization calibrator used for these observations was Neptune, observed immediately before IRAS 4A in track 1718. The data on Neptune were phase calibrated using 1921-293. The quality of the data were sufficient to use antenna-based gain calibration, which solves for the gain (amplitude and phase) of each telescope using closure relations. The instrumental polarization terms were measured by assuming the emission from the planet was unpolarized. The measured instrumental terms for this track are given in Table 5.4. The term LR cosine is used to refer to the coefficient corresponding to $\epsilon_{L_2} cos\phi_{L_2} + \epsilon_{R_1} cos\phi_{R_1}$ (see equation [4.3]). Stokes parameters for Neptune were calculated both with and without correction for the instrumental polarization. Maps were made of each Stokes parameters with the AIPS (Astronomical Imaging Processing Software, written by the National Radio Astronomical Observatory) task MX. The Q and U images were then combined to form the linear polarization. The uncorrected linear polarization was 1.9% of the peak in the total intensity and the peak in the linear polarization was offset from the peak by a few arcsec to the southeast. After the correction for instrumental polarization was applied (in MMA), the linear polarization of Neptune was mapped again. This residual instrumental polarization was 0.3% of the total intensity, which was within the noise level.

The IRAS 4A data were corrected with the instrumental polarization terms derived from Neptune. The data were then imaged in DIFMAP (M. Shepard, Caltech). The CLEAN algorithm (Hogbom, 1974) was used to deconvolve the synthesized beam from the image. The I image was CLEANed and phase self-calibrated. The CLEAN

	Instrumental polarization terms			
Baseline	RL cosine	RL sine	LR cosine	LR sine
1-2	-0.030	0.002	0.055	0.019
1-3	-0.005	0.032	0.089	0.014
1-4	0.009	-0.045	0.067	-0.005
1-5	-0.085	-0.023	0.005	-0.046
1-6	0.008	0.021	0.053	0.039
2-3	0.030	0.057	0.077	0.014
2-4	0.070	-0.025	0.049	-0.009
2-5	-0.020	-0.029	-0.004	-0.028
2-6	0.038	0.037	0.025	0.034
3-4	0.085	-0.053	0.072	0.034
3-5	0.010	-0.037	0.009	0.001
3-6	0.093	0.032	0.013	0.092
4-5	-0.001	-0.073	0.028	-0.073
4-6	0.067	0.004	0.075	-0.008
5-6	-0.007	-0.004	-0.001	-0.022

Table 5.4: Instrumental polarization calibration term coefficients for observations of Neptune (track 1718). See Chapter 4 for the derivation of the instrumental polarization terms.

box and phase corrections from this map were used when CLEANing the Q and U maps. Using the same CLEAN boxes constrains the CLEAN components for Q and U to be placed only where total intensity emission is present. The Q and U maps were imported into AIPS and combined to form L and ϕ_{pol}. The peak total intensity in the map was 213 mJy beam^{-1}. The peak in the linear polarization map was 8.7 mJy beam^{-1} and offset 2″ to the northeast of the total intensity peak. Images were also made without phase self-calibration and the polarization peak and offset were very similar to the images with self-calibration.

Several tests were performed to verify that the observed polarization was due to the source rather than instrumental effects. Images were made with a much smaller pixel size. This did not change the offset in the linear polarization. The 15 baselines were divided into two groups chosen to have similar *uv* coverage, and separate maps were made for each set of baselines for both Neptune (without the instrumental polarization correction) and IRAS 4A. For Neptune, the images of Q and U are different for the data sets. This is expected since the instrumental terms vary for each baseline. The maps for IRAS 4A are very similar, though there are slight shifts in the peak positions due to the increased noise. The data were also divided by parallactic angle. The range of parallactic angle as a function of hour angle for IRAS 4A is shown in Figure 5.5. Two data sets were formed, one with a parallactic angle range of –70 to –55° and one with a range of 55 to 70°. The data near transit, where the parallactic angle is changing very quickly, were not included. While there were small shifts in the peak positions of the polarized emission, both polarization images are shifted north from the total intensity peak. Dividing the data by parallactic angle is equivalent to dividing it in time and tests for slowly varying levels of instrumental polarization, which were not seen. All these tests provide further evidence that the observed polarization was due to intrinsic source polarization rather than instrumental effects and that the offset of the linearly polarized emission from the total intensity was real.

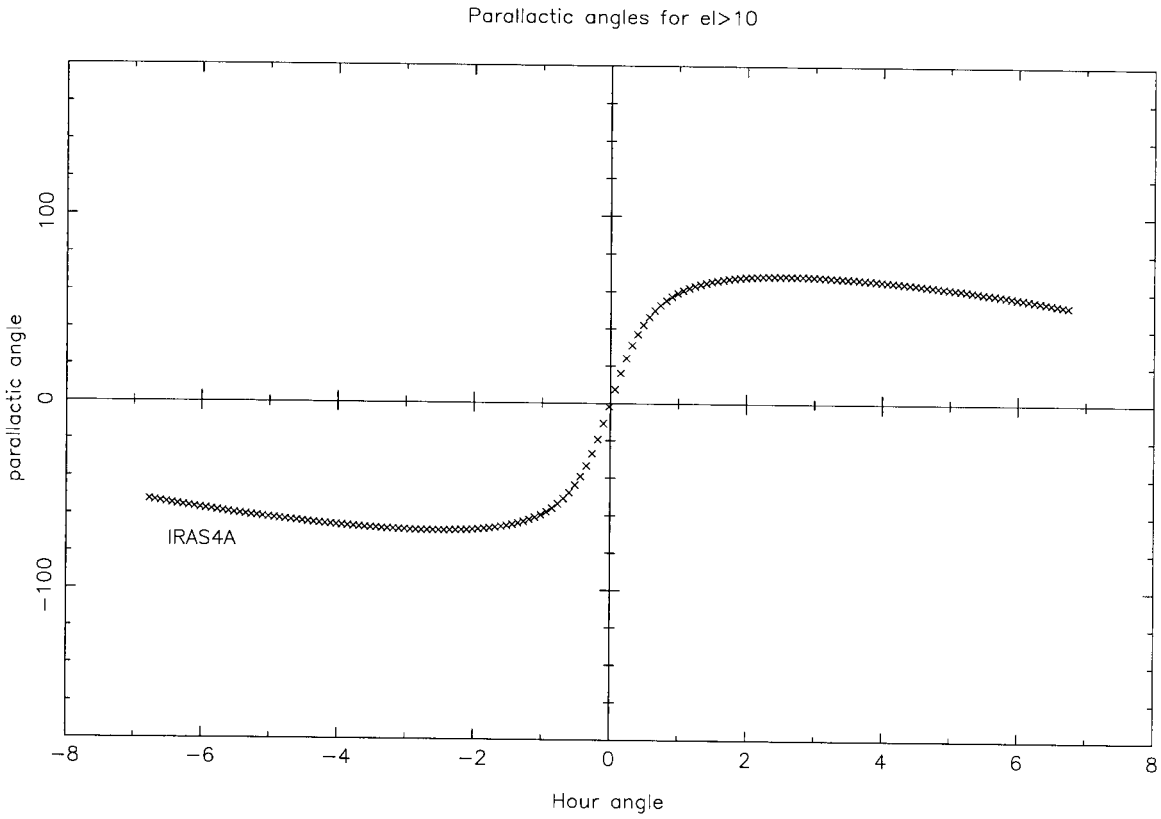

Figure 5.5: The parallactic angle as a function of hour angle for IRAS 4A.

Chapter 6 Results and discussion

6.1 Observational results

6.1.1 IRAS 4A

The young stellar object NGC 1333/IRAS 4A was observed during the 1994/95 and 1995/96 observing seasons. The resolution of the 4 tracks listed in Chapter 4, when combined with natural weighting, is $3\farcs7 \times 2\farcs8$ at a position angle of 74°. The peak total intensity was 217 mJy beam^{-1} and the total integrated flux was 270 $\pm$ 50 mJy, where the uncertainty is due to the flux calibration. An elliptical Gaussian was fit to the *uv* data (using modelfit in DIFMAP). The best fit had a total flux of 266 mJy, a FWHM size of $3\farcs2 \times 3\farcs2$ radius and was centered at RA(1950) $03^h26^m04.41^s$ and dec(1950) 31°03′13.3″ (0.″55 north and 0.″24 east of the field center).

A lower limit to the density can be estimated by assuming the continuum emission is optically thin. For thermal emission the mass is given by

$$M = \frac{FD^2}{\kappa B(T)}, \tag{6.1}$$

where F is the flux, D is the distance, κ is the mass opacity and $B(T)$ is the Planck function. For an opacity of 0.0095 cm^2 gm^{-1} and a temperature of 40 K, the derived mass is 0.2 $M_\odot$. The opacity and temperature values used are discussed in the following sections. For the source size from the Gaussian fit, a lower limit to the H_2 density probed by these observations is 2×10^8 cm^{-3}.

Figure 6.1 shows the linear polarization emission detected toward IRAS 4A plotted with the total intensity (a) and with polarization position angle vectors (b). A lower resolution image is given in Akeson et al. (1996). The peak linear polarization is

8.6 ± 1.4 mJy beam^{-1} (the rms errors here are due to the thermal noise and residual instrumental polarization) and is offset from the total intensity peak. The angle of the linear polarization at the peak is $-83° \pm 6°$, corresponding to a magnetic field direction of $7° \pm 6°$. The polarization position angle ranges from $-70°$ to $-86°$ across the polarized emission (with errors ranging from 10° to 6° depending on the signal strength). The average polarized flux, defined as the integrated linear polarization divided by the integrated total intensity is $4.4\% \pm 0.7\%$. This is somewhat higher than the $3.2\% \pm 0.3\%$ measured at 0.85 mm in a 14″ beam by Minchin et al. (1995), but agrees with the $4.6\% \pm 0.8\%$ measured by Tamura et al. (1995) at 1.1 mm in a 19″ beam. At the peak of the linearly polarized emission, the polarization percentage is $6\% \pm 1\%$.

The magnetic field directions implied by the polarization observations can be compared to other orientations in the morphology of IRAS 4A. The well-collimated outflow powered by IRAS 4A is directed almost north-south close to the source, but bends to a position angle of ~45° over larger scales (Blake et al., 1995) (Figure 5.1). Recent sub-millimeter observations by Lay et al. (1995) with the CSO-JCMT interferometer found that IRAS 4A contains a 1.″8 binary at a position angle of 130°, although they were unable to determine the absolute position. These directions are consistent with collapse of the core along the field lines, as the field roughly is parallel to directions seen in the molecular outflow. The magnetic field direction as implied from the single dish observations (Minchin et al., 1995; Tamura et al., 1995) is parallel to the direction of the outflow further from the source (~45°) while the field direction implied by our data is parallel to the outflow near the central source. However, these results are not incompatible as the higher frequency observations are more sensitive to the outer layers of the envelope, as the emission is more optically thick at shorter wavelengths. Also, the interferometer acts to filter any smooth component and is therefore missing some of the flux seen in the single dish observations. The different field angles from the single dish versus the interferometer data imply variations of the magnetic field direction between the outer regions of the envelope as seen by the

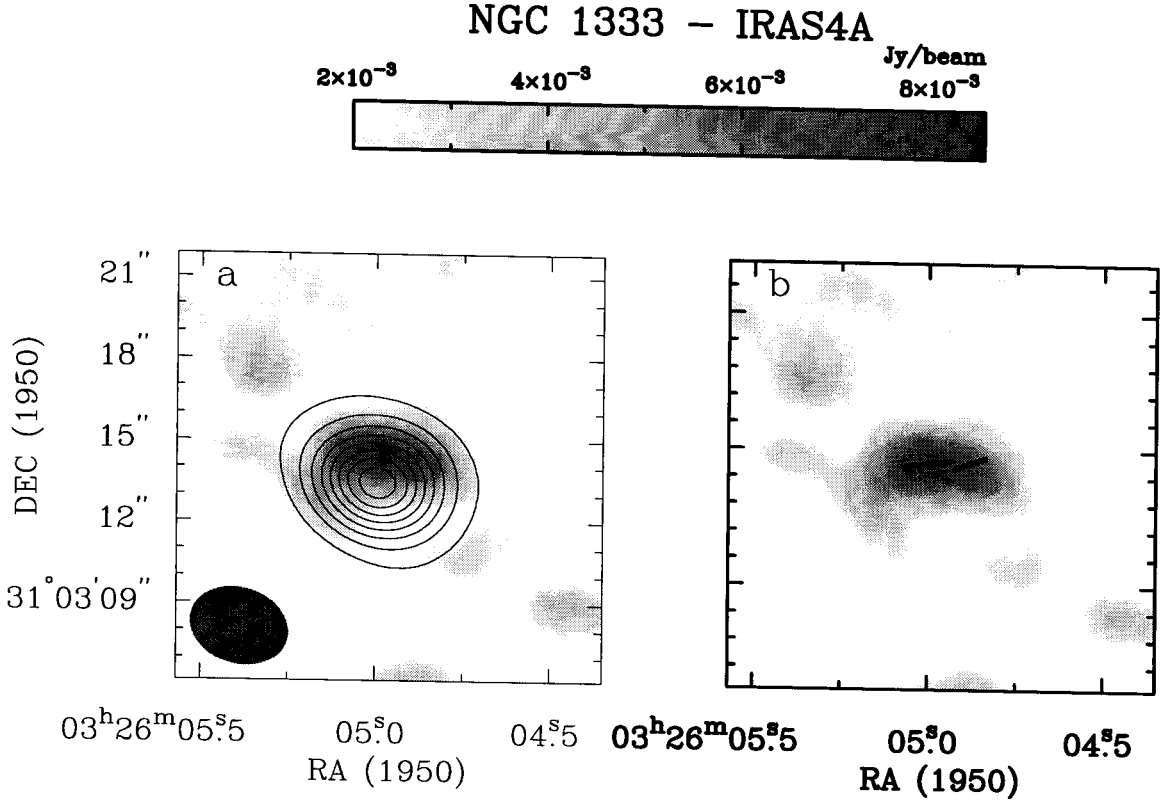

Figure 6.1: a) The linearly polarized emission (grey scale) plotted with the total intensity (contours). The contour levels are 25 mJy beam^{-1}. The beam is 3.″7 by 2.″8 at a position angle of 74°. b) The linearly polarized emission (grey scale) and two vectors of the polarization angle representing the range of angles seen in the data. The polarization vectors are separated by half a beam.

single dish observations and the size scale probed by the interferometer ($\sim$ 1000 AU).

The large scale magnetic field in Perseus has been studied with selective extinction observations by Turnshek et al. (1980) and Goodman et al. (1990). Both groups covered an area of several square degrees in the Perseus cloud and found magnetic field angle distributions with peaks near 70° and 145°. Observations of two velocity components toward this cloud (Loren, 1976) led both Turnshek et al. and Goodman et al. to infer the presence of two clouds along the line of sight to Perseus. Infrared extinction measurements toward the $\sim$1 parsec core of NGC 1333 indicated a local field direction of 125° (Tamura et al., 1988). None of the large scale field directions match the directions we measured for the field in the vicinity of IRAS 4A. This non-alignment suggests substantial structure of the magnetic field in the cloud core, as the optical and infrared observations are probing the magnetic field structure in the outer, less dense layers of the cloud, while the millimeter observations are sensitive only to the fields in the dense gas immediately surrounding the protostellar source. The NGC 1333 core contains 5 sources with known outflows and there is no alignment between these outflows (Liseau et al., 1988). This suggests that the parsec scale magnetic field did not determine the direction of collapse for these molecular cores. However, the small scale magnetic field may still be important within a single core as demonstrated by the alignment of the small scale field direction in IRAS 4A with directions seen in the outflow.

6.1.2 Radiative transfer models

An offset of the linearly polarized emission from the total intensity can be explained by a model in which the field has an hourglass morphology inclined toward the line of sight and the optical depth of the emission is $\gtrsim 1$ (Hildebrand, private communication). As illustrated in Figure 6.2, the field lines of the red-shifted lobe are nearly in the plane of the sky, while on the blue-shifted side they are inclined toward the line of sight. Therefore, there will be more polarized emission from envelope material on

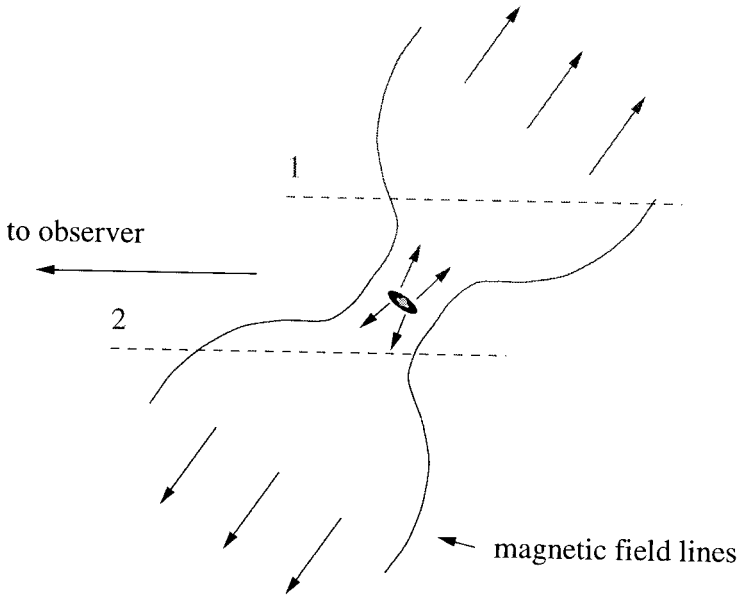

Figure 6.2: The basic geometry for the magnetic field structure in the radiative transfer model. The magnetic field at the front of the red-shifted lobe (1) is nearly in the plane of the sky, while the field sample through the blue lobe (2) is inclined toward the line of sight.

the red-shifted side. In order to investigate the effect of the magnetic field geometry and the envelope density/temperature structure on the observed linear polarization, I constructed models of the source and calculated the radiative transfer for the total intensity and the linear polarization. A representative model was then convolved with a Gaussian beam to match the resolution of the observations.

The model parameters are the density distribution, temperature distribution, magnetic field geometry and dust opacity. All parameters are azimuthally symmetric, but can vary as a function of radius. The magnetic field is parameterized to roughly match the hourglass geometries of theoretical models (Galli and Shu, 1993; Fiedler and Mouschovias, 1993). The goal of these models is not to distinguish between

competing theories, but to test the suitability of an hourglass field morphology in matching the data. Outside a given radius, R_o, the field is uniform. Inside R_o, the magnetic field angle Θ_B (measured from the mid-plane) for a point a distance r from the center and at an angle θ from the mid-plane is given by

$$\Theta_B = (1 - \left(\frac{r}{R_o}\right)^{\alpha})\theta + \left(\frac{r}{R_o}\right)^{\alpha} 90°, \quad \text{for} \quad r < R_o. \tag{6.2}$$

The exponent α controls how much the field is 'pinched' toward the center. For $\alpha = 0$ the magnetic field is uniform everywhere. The field geometry at the center of the object is shown in Figure 6.3 for three values of α and $R_o = 4''$, which corresponds to 1400 AU at a distance of 350 pc. In the models of Galli and Shu (1993), the magnetic field lines are in an hourglass morphology out to at least 2500 AU, depending on the age of the object. As most of the emission is centered within a 5″ radius, the value of R_o is not crucial as long as it is greater than 5″. A value of $R_o = 3000$ AU is used in the models discussed below.

A three dimensional grid is set up in the coordinate system of the object. The x-axis is in the plane of the sky, and the rotation of the object (to produce the desired inclination) is about the x-axis. The azimuthal symmetry is about the y-axis, and the radiative transfer calculations are performed along a line of sight through the object for the specified inclination angle. The radiative transfer equations used for the total intensity, I and the linear polarization, $\mathbf{L}$ (where $\mathbf{L}$=$\mathbf{Q}$+i$\mathbf{U}$) are

$$\frac{dI}{ds} = -\rho\kappa I + \rho\kappa B(T), \tag{6.3}$$

$$\frac{dL}{ds} = \frac{dI_{\|}}{ds} - \frac{dI_{\perp}}{ds}, \tag{6.4}$$

where B is the Planck function, ds is the length of the segment along the line of sight, and $I_{\|}$ and $I_{\perp}$ are the intensities in two orthogonal coordinates. The perpendicular direction is defined along the x-axis. Defining the opacity, κ in these orthogonal

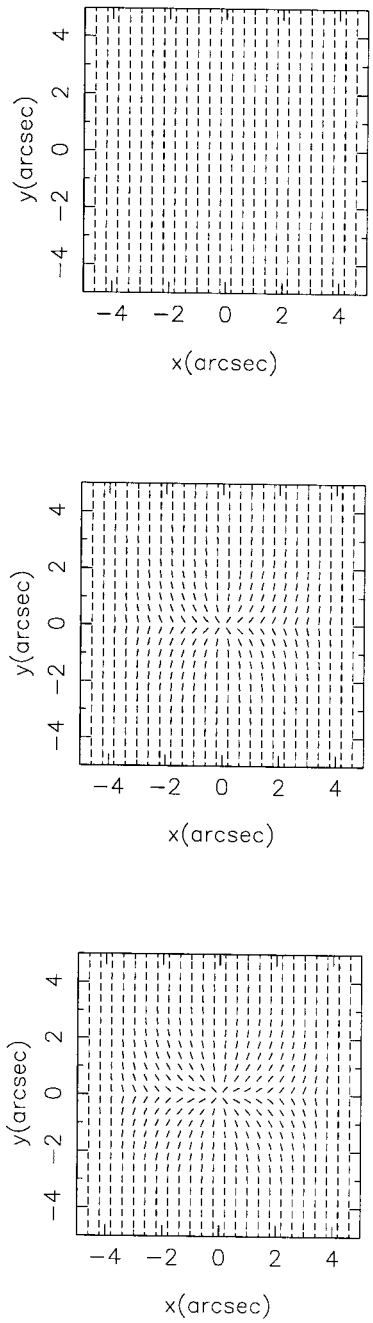

Figure 6.3: The magnetic field geometry for three values of the exponent parameter α. In the top section $\alpha = 0$, 0.5 in the middle and 1 in the bottom. The cut-off radius is 4″, which corresponds to 1400 AU at a distance of 350 pc.

coordinates,

$$\kappa = \kappa_{\|} + \kappa_{\perp}, \tag{6.5}$$

$$\Delta\kappa_{max} = \kappa_{\|} - \kappa_{\perp}, \tag{6.6}$$

equation [6.4] can be written as

$$\frac{dL}{ds} = -\frac{\rho\kappa}{2}L - \frac{\rho\Delta\kappa}{2}I + \rho\Delta\kappa B. \tag{6.7}$$

In this formalism, $\Delta\kappa_{max}$ represents the maximum allowed percentage of the linear polarization. The linearly polarized emission from any given cube can be decreased from this value if the magnetic field direction is not completely in the plane of the sky. The value of $\Delta\kappa$ used in equation [6.7] varies for each cube and is given by $\Delta\kappa_{max} * cos\phi$, where ϕ is the angle of the magnetic field direction with respect to the plane of the sky. Because the linear polarization has both a magnitude and a position angle, the summation of equation [6.7] over the line of sight is done for two orthogonal components of $\mathbf{L}$, where the angle ϕ_{pol} is 90° plus the angle of the magnetic field in the plane of the sky.

The radial profiles for the density and temperature distributions are described as

$$n = n_o(\frac{r}{r_{inner}})^{-p}, \tag{6.8}$$

$$T = T_o(\frac{r}{r_{inner}})^{-q}. \tag{6.9}$$

For an isothermal sphere $p = 2$, while a value of $p = 1.5$ corresponds to an infalling core. The Galli and Shu (1993) models of magnetized core collapse begin with a density profile of $p = 2$, though this exponent changes slightly during the collapse. Observations of IRAS 4A by Blake et al. (1995) were consistent with a value of $p = 1.9$. A value of $p = 2$ was used in the models discussed below. The reference density, n_o, is used to set the optical depth. The value of q depends on the dust properties and the density distribution. Observational results range from $q = 0.4$

for the dense warm core surrounding a luminous source (Butner et al., 1990) to $q = 0.5 - 0.75$ for a sample of T Tauri stars, some of which have massive disks (Beckwith and Sargent, 1993). A value of $q = 0.5$ was used in all models. The general results of the models are not highly sensitive to the exact values used for p and q. I have used $\kappa = 9.5 \times 10^{-3}$ cm^2 gm^{-1}, extrapolated from the Hildebrand (1983) value at 250 μm for $\kappa_\nu \propto \nu^1$. If the true opacity at 3 mm is higher, this will simply lower the reference density needed to produce a given optical depth.

In order to produce significant asymmetry in the polarized emission, the optical depth of the total intensity must be near unity or higher and the symmetry axis of the magnetic field must be inclined from the plane of the sky. A constraint on the inclination of the source is the high collimation of the molecular outflow, which indicates that it is not aligned along the line of sight. The line width observed in the outflow by Blake et al. (1995) of $\Delta v \sim 15$ km sec^{-1} indicates that the outflow does not lie in the plane on the sky. The general assumption for young stellar objects is that the optical depth in the outer disk and envelope is low at 3 mm. This is because of the very high column densities needed to produce high optical depths at this long wavelength. For an opacity $\kappa = 0.0095$ gm cm^{-3}, the H_2 column density must be 3×10^{25} cm^{-2} for an optical depth of one. Thus, models with optical depths near unity (rather than larger) are more plausible.

An additional constraint for the model is the presence of the 600 AU (1.″8) binary. The optical depth to the center of the envelope at 345 GHz must be sufficiently low such that the binary components are observable. The binary and the outflow may act to 'clear out' the inner regions of the envelope. In disk models, the circumbinary material is cleared out to a radius of twice the binary separation (Artymowicz and Lubow, 1994). Thus, the models are all constructed with a spherical hole in the center of the density distribution, which also decreases the optical depth to the center. Including an inner radius to the envelope also removes the computational difficulty of a singularity at the origin.

The observational constraints on the model are the total flux at 3 mm, the spher-

ical symmetry of the total intensity, and the offset and elongation of the polarized emission. The interferometer flux may be missing emission from structure on scales larger than $\sim$10″. This scale was determined by mapping Gaussian sources of various widths with the *uv* sampling of the data. As there is no single-dish observation of IRAS 4A at 3 mm, I have extrapolated a flux of 500 mJy from the 1.1 mm flux and spectral index of 2.1 from Sandell et al. (1991). The CSO-JCMT interferometer observations of Lay et al. (1995) detected only 10% of the single dish flux. While this percentage will increase at lower frequencies if the accretion disk has a higher optical depth than the envelope, I have approximated that all the 3 mm emission is from the envelope.

The reference temperature was determined by comparing the model total flux to the total flux for IRAS 4A as calculated above. For a density corresponding to an optical depth of 1, the reference temperature (at r_o = 500 AU) used was 20 K. The total flux in this model is 1 Jy. Given the uncertainty in calculating the total flux, a factor of 2 is not unreasonable.

A series of models with varying inclination and magnetic field geometries are shown in Figure 6.4 for two values of the optical depth. The resolution of the model images is set by the pixel size (0.″1). The axis of symmetry pointing away from the observer (i.e., the red-shifted outflow) is to the top of the plot. As the inclination angle is increased, the contrast in the intensity between the two sides increases. This contrast can also be increased with higher optical depths (panel b). The ratio of the polarized emission to the total intensity is set by the value of $\Delta\kappa_{max}$.

The distance between the peak of the polarized emission and the center of the source is dominated by the inner cutoff radius. The models have an inner cut-off radius of 500 AU, roughly twice the binary separation. Another effect on the shape of the envelope is the bipolar outflow, which must pass through the envelope. While this effect is not accounted for, the magnetic field should be parallel to the outflow. The symmetry of the total intensity indicates that the outflow does not disrupt the envelope significantly along the poles on scales resolved by the observations. For

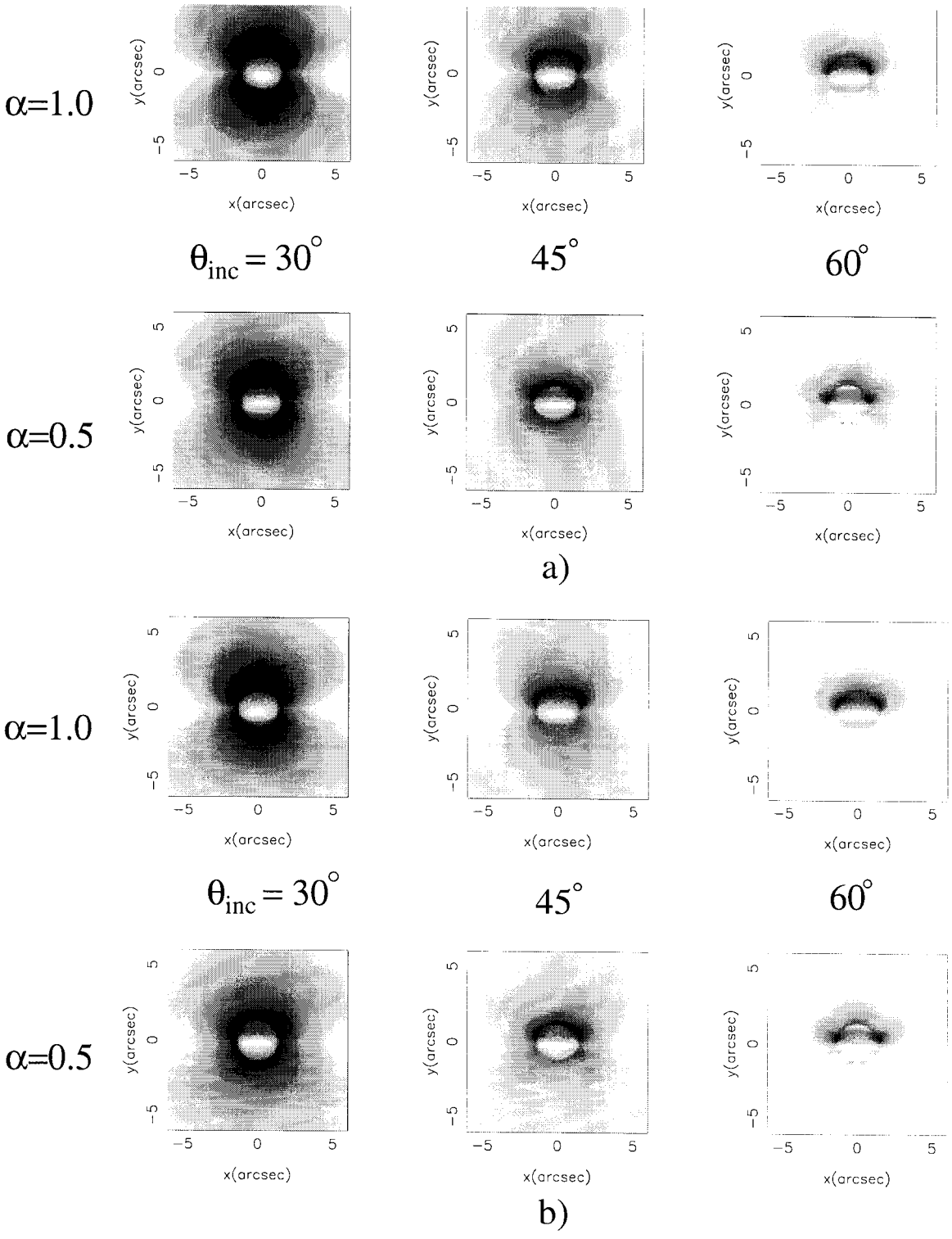

Figure 6.4: The polarized emission from a series of models with varying inclination and magnetic field parameter α (see equation [6.2]). The inner radius of the envelope is 500 AU. a) tau = 0.75 b) tau=1.0.

the magnetic field geometry described above, the range of inclination angles which roughly fit the data is 45° to 65° and the optical depth must be >0.7.

A model with 50° inclination, $\tau = 1$, inner radius of 500 AU and $\alpha = 1.0$ is presented in Figure 6.5. The temperature and density parameters are listed in Table 6.1. For this model, the visibilities have been multiplied by the transform of a 3″ Gaussian beam and restricted to the visibility range of the IRAS 4A data. The value of $\Delta\kappa_{max}$ necessary to match the observed average polarization is 8%. The model presented is representative of the range of inclination angles and optical depths that generally reproduce the observed linear polarization. Given the many parameters in the model which affect the polarized emission morphology (magnetic field structure, density and temperature structure), detailed fits were not made to the data.

Model parameter		
Density	n_o	3.2×10^9 cm^{-3}
	p	2
Temperature	T_o	20 K
	q	0.5
Inner radius		500 AU
Magnetic field morphology	α	1.0

Table 6.1: The parameters for the model presented in Figure 6.5. The reference values for the density and temperature are given for the inner radius of the envelope (500 AU).

This model reproduces several features seen in the data and demonstrates that an hourglass magnetic field morphology is consistent with the observations. The peak of the linear polarization is offset from the peak of the total intensity toward the side of the red-shifted outflow. While there is polarized emission on the blue-shifted side in the model, it would not have been detected in our observations given the rms noise level in the maps. The model polarized emission is extended in a direction perpendicular to the axis of the magnetic field. This extension is a natural feature of the hourglass geometry used (see Figure 6.4) and occurs despite the spherical symmetry

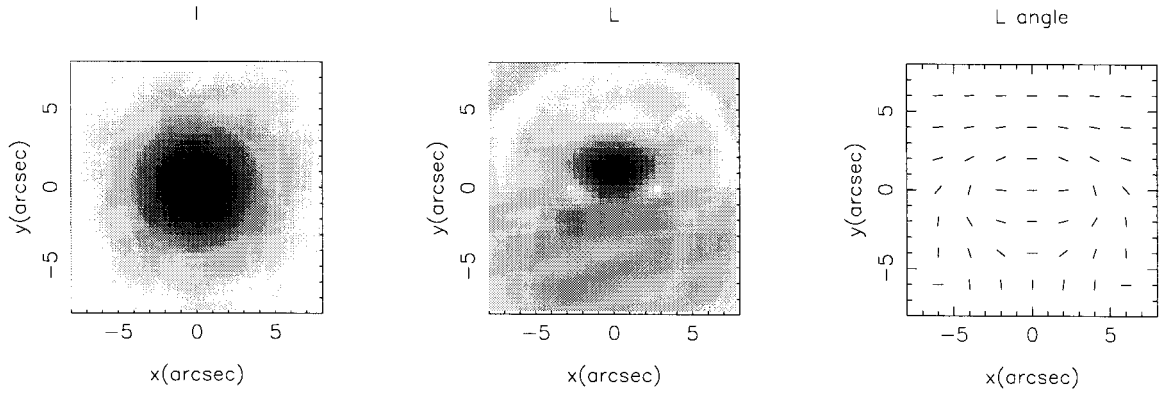

Figure 6.5: The total intensity (left), polarized intensity (middle) and polarization position angle (right) for the model described in the text. The envelope has an inner radius of 500 AU and the magnetic field symmetry axis is inclined 50° from the plane of the sky, with the red-shifted lobe to the top. The peak optical depth is one.

of the density and temperature profiles. The polarization position angle at the peak of the polarized emission is perpendicular to the outflow axis, as seen in the model. The value of $\Delta\kappa_{max} = 8\%$ necessary to match the observed average polarization is close to the maximum observed polarization (9%) in the regions surveyed by Hildebrand et al. (1995). A more detailed determination of the field structure at the edges of the emission is prevented by the lower signal-to-noise of these points. Higher resolution data, such as the 1″ resolution available at 1 mm, will provide more information about the structure of the magnetic field.

The main deficiency of this model is the need for high column densities (to produce the polarized emission offset) with low temperatures (to keep the continuum emission at the level observed). The reference temperature used in the models was 20 K at 500 AU. However, the effective temperature of 37 K derived by Sandell et al. (1991) is considerably higher. The peak brightness temperature of 7 K implies optically thin emission if the effective temperature is 37 K. This inconsistency could be explained by dense clumps in the envelope which are not completely filling the beam.

While the 3 mm emission from circumstellar envelopes is often assumed to be optically thin, it is not implausible that a dense envelope would have moderate optical

depth at 3 mm. The density at the inner radius of the envelope used in the above model is 2×10^9 cm^{-3}. In a fit to the infrared and sub-millimeter flux of IRAS 4A, Sandell et al. (1991) fit a spectral index of $S_\nu \propto \nu^{2.1}$ for wavelengths shorter than 1.1 mm and $S_\nu \propto \nu^{2.4}$ from 1.1 mm to 2 mm. They suggest that this spectral index is consistent with optically thick emission for wavelengths shorter than 1 mm. They estimated an average density of 9×10^9 cm^{-3} from their continuum observations.

As the polarized emission depends on the grain properties as well as the alignment efficiency, the magnetic field strength can not be directly determined from the observations. However, the conclusion that the magnetic field morphology is similar to those predicted for magnetically supported envelopes leads to some estimates of the field strength. In the Galli and Shu (1993) model the field strength at a density of 10^7 cm^{-3} is 1 mG, while in the Fiedler and Mouschovias (1993) model the field strength is 3 mG at a density of 10^9 cm^{-3}. Both groups used an initial field strength of 30 μG. If the envelope surrounding IRAS 4A is magnetically supported, the field strength can be estimated by equating the gravitational energy from the central source ($3/5\ GM^2/R$) to the magnetic energy ($1/3\ B^2R^3$). The mass of the central source is difficult to determine as it is not directly visible and much of the luminosity may be due to accretion. Estimating the central mass as 1 $M_\odot$ the magnetic field at a distance of 1000 AU is 3 mG, similar to the values from the models.

6.1.3 IRAS 16293

Images of the young binary system IRAS 16293-2422 were constructed from the tracks listed in Chapter 5. Combination of these four tracks with natural weighting yields maps with a resolution of $5\farcs3 \times 3\farcs1$ at a position angle of –19° (Figure 6.6). The total intensity is clearly extended along the position angle of the two binary components, though there is not a distinct second peak. The peak of the 3 mm continuum emission lies nearest the position of the northwestern source (1629B), consistent with previous observations. The total integrated emission is 550 ± 100 mJy, where the error is due

		Component A	Component B
Position	RA(1950)	16 29 21.05(0.02)	16 29 20.79(0.01)
	dec(1950)	-24 22 16.22(0.28)	-24 22 12.32 (0.11)
Size	major axis	6.15	3.09
	minor axis	2.46	2.04
	position angle	2.4	163
Flux	peak	115(9) mJy/beam	273(11) mJy/beam
	integrated	218(30) mJy	365(25) mJy
Radio position			
	RA(1950)	16 29 21.02	16 29 20.77
	dec(1950)	-24 22 15.70	-24 22 11.72

Table 6.2: The derived parameters for the Gaussian fit to the continuum emission. The errors given are those determined by the fitting routine which include the measured noise in the map, but do not include the systematic uncertainties in the flux calibration. The radio continuum positions from Wootten (1989) are given for comparison.

to the uncertainty in the flux calibration. The continuum emission was modeled as two Gaussian components using the AIPS task IMFIT. The results of the fit are given in Table 6.2. The residuals between the data and the model are less than 10 mJy in all pixels. 1629B is brighter and more compact than 1629A. The flux ratio observed agrees roughly with that seen by Mundy et al. (1992). The flux measured in a single dish beam of 60″ was 600 ± 120 mJy (Walker et al., 1986), thus the interferometer is recovering most or all of the flux.

The linear polarization detected toward IRAS 16293 is presented in Figure 6.6. The peak of the linear polarization is 6.2 ± 1.6 mJy beam^{-1} and is offset 1.″9 to the southeast of the peak of the total intensity, which is located at the position of 1629B. An estimate of the positional uncertainty of an emission peak due to noise was calculated by Reid et al. (1988) to be 0.45 θ/SNR, where θ is the FWHM of the source and SNR is the signal to noise ratio. For the polarized emission, the positional rms is 0.″5, and the offset from the peak of 1629B is greater than 3σ. The peak of the polarized emission is 2.1% ± 0.5% of the peak in the total intensity. The position

angle of the polarized emission at the peak is 44° ± 7°. A second, less significant peak (3σ) in the polarized emission is located ~2″ north of the total intensity peak and has a position angle of 10°± 9°. The integrated polarization emission is 3.7 mJy; however, this value is underestimated because of the blanking used in the calculation of the polarization map.

Although the polarized emission detected is weak, there are several indications that it is real source polarization rather than residual instrumental effects. Polarized emission can be seen at the same location and position angle in each of the two low resolution tracks. The data were divided into two ranges of parallactic angle and similar polarized emission was seen in both maps. For IRAS 16293, which has a declination of −24°, the parallactic angle changes almost linearly with hour angle and the range of parallactic angle in the data is ± 30°. Any errors in the instrumental polarization correction are multiplied by twice the parallactic angle before being mapped (equation [4.3]). Thus the phase of any constant gain offset (such as instrumental polarization) will be smeared over the track, and its amplitude will be reduced. The level of this reduction is difficult to estimate for this source, as the visibility amplitude changes with hour angle. The residual instrumental polarization level is estimated to be ~0.5% (see Chapter 4), and will be somewhat reduced from the parallactic angle effect described above. However, the polarized emission is at least 4 times the estimate for the residual instrumental polarization.

The magnetic field position angle implied at the peak polarization is 134° ± 7°. This angle agrees roughly with the Flett and Murray (1991) observation of 152° ± 11°at 0.8 mm with 11″ resolution, but not with the Tamura et al. (1993) measurement of 54° ± 5°at 1.1 mm with 19″ resolution. This large disagreement of the position angle at wavelengths varying from 3 to 0.8 mm is difficult to understand if all the data are correct. The formal error estimate for the polarization position angle uses a first order approximation of the errors in Q and U and the actual error will be much larger for low signal-to-noise detections. Thus, the position angle of the Flett and Murray observation, which is slightly less than 3σ, is not well determined.

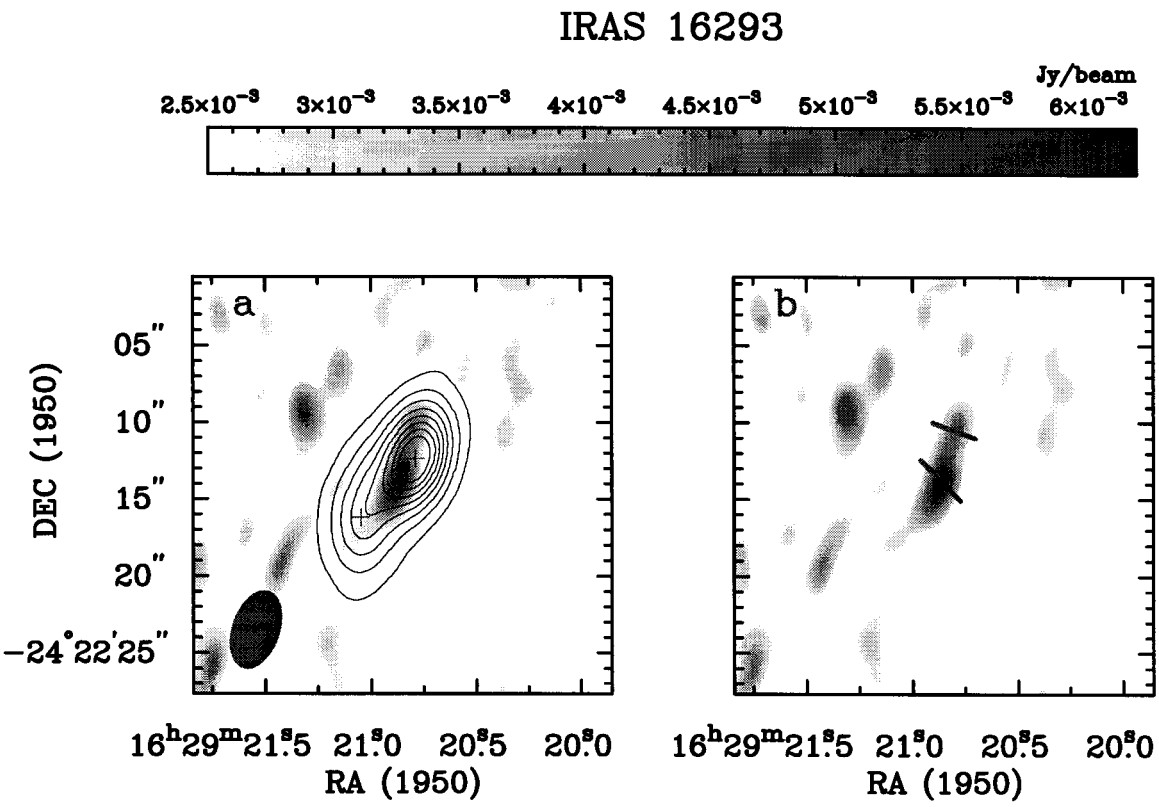

Figure 6.6: a) The linearly polarized emission (grey scale) plotted with the total intensity (contours). The contour levels are 30 mJy/beam. The beam is 5.″3 by 3.″1 at a position angle of −19°. b) The linearly polarized emission (grey scale) and vectors of the polarization angle for the two peaks in polarized emission.

Comparing the field direction as measured on larger scales to the nearly orthogonal measurements ($\sim$55° and $\sim$140°) for the millimeter and sub-millimeter emission may provide further information on this disagreement. The large scale magnetic field in Ophiuchus was analyzed by Goodman et al. (1990) using optical selective extinction observations. While the average position angle of the selective extinction (and therefore of the magnetic field) was 68° $\pm$ 40° over the entire dark cloud, the position angles measured in the vicinity of IRAS 16293 are not well ordered. In Figure 6.7 the polarization vectors for all the stars in the Vrba et al. (1976) sample within 1° of IRAS 16293 are plotted. These observations were included in the analysis of Goodman et al. (1990). While the large scale field as traced by the selective extinction appears very uniform northwest of the source, the polarization vectors to the southeast are not well ordered. Thus, the large scale fields near IRAS 16293 do not overwhelmingly favor either of the small scale field directions observed.

The magnetic field direction I observe in the envelope of IRAS 16293 can also be compared to the symmetry axes of the object. The minor axis of the circumbinary disk, as traced by $C^{18}O$ emission, is at a position angle of 60° (Mundy et al., 1990) (Figure 6.8). The CS emission from NE-SW outflow appears to emerge from 1629A at a position angle of $\sim$45° (Walker et al., 1993). The E-W lobes can not be traced directly into the circumbinary material, but Walker et al. (1993) suggest that 1629B powers this outflow. The line emission from the west red-shifted outflow lobe (the 1629B outflow) has a much steeper angle close to the source (Walker et al., 1990). The extended CO emission from the outflow lobe is oriented at roughly –45°, while the CS emission appears shell-like. At larger distances from the source (tens of arcsec), this lobe has a position angle closer to –90°(Figure 6.8). While the $-45°$ position is parallel to the magnetic field direction implied by the observations, the polarized emission is located on the side of 1629B that corresponds to the blue-shifted lobe.

As the general morphology of IRAS 16293 is considerably more complicated than that of IRAS 4A, no radiative transfer models were calculated. If the polarized emission is associated with the material surrounding 1629B, the offset of the linear

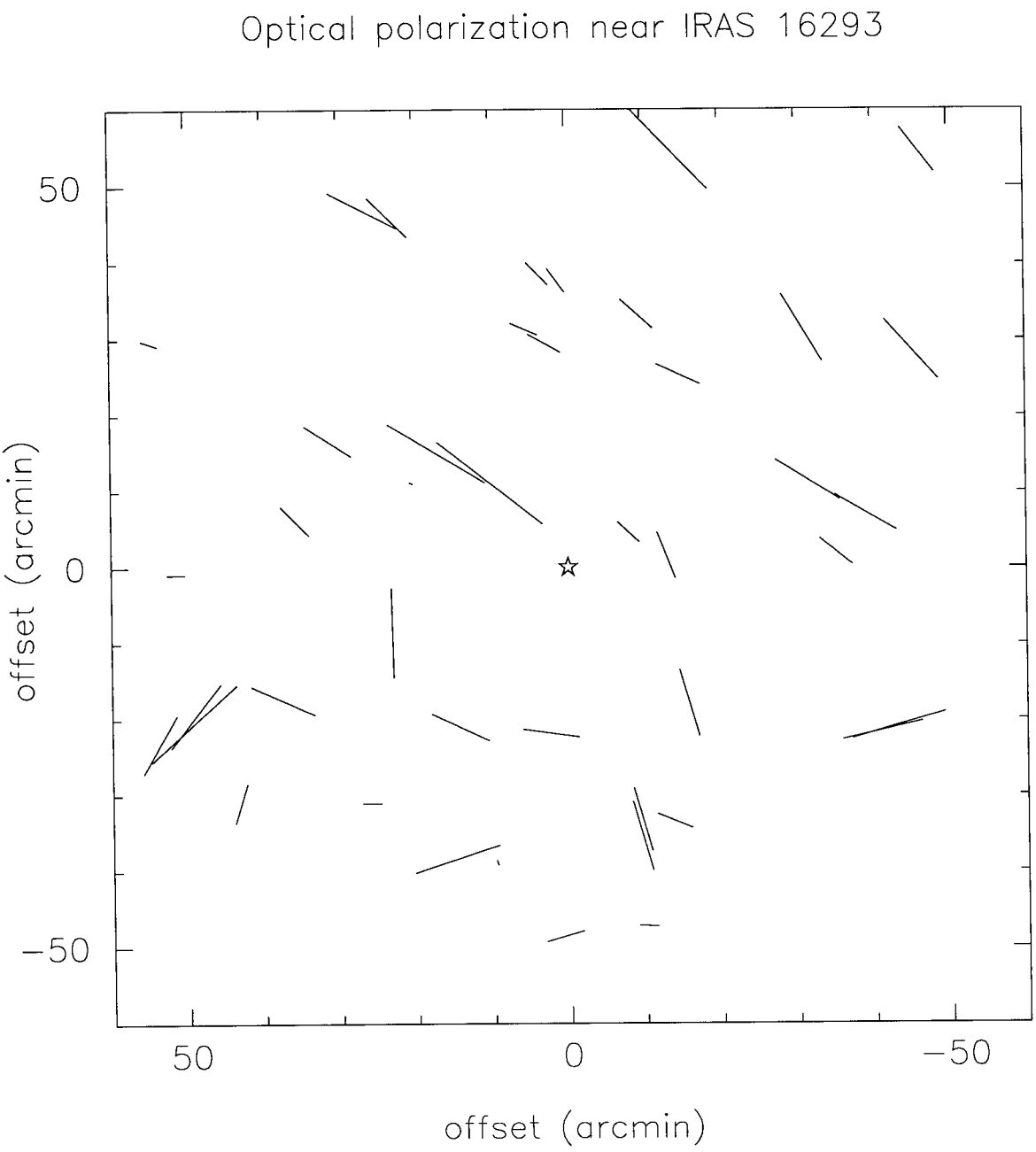

Figure 6.7: The optical polarization vectors for the stars in the Vrba, Strom and Strom (1976) survey within 1° of IRAS 16293. Recall that the magnetic field direction is parallel to the polarization vector. Only detections greater than 4 σ are plotted.

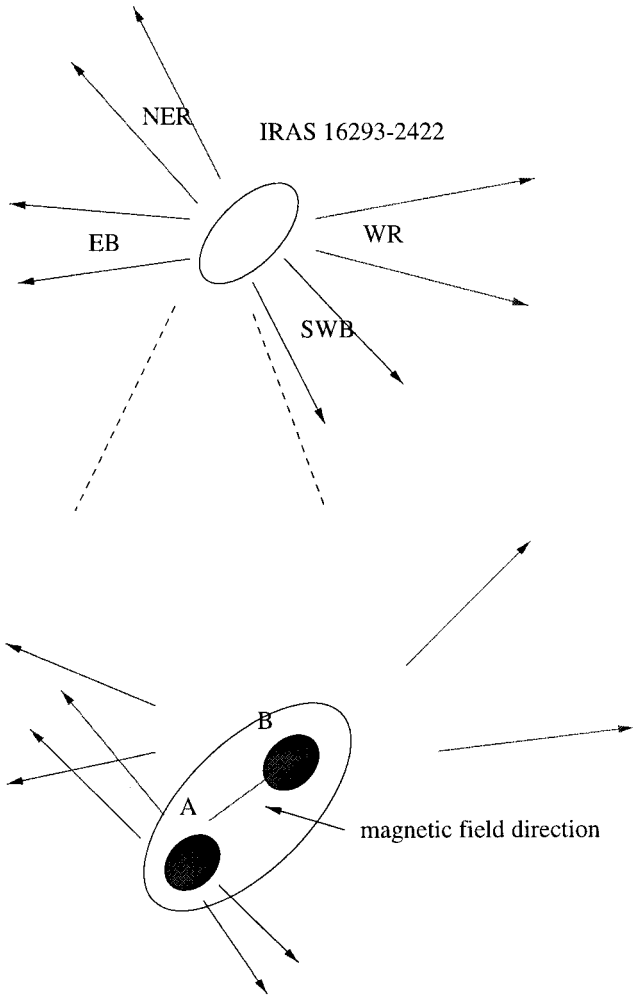

Figure 6.8: Cartoon representation of the four outflows (blue-shifted east: EB, blue-shifted south-west: SWB, red-shifted west: WR, and red-shifted north-east: NER) emanating from IRAS 16283 on both large and small scales. The accretion disks shown are not to scale. The magnetic field direction implied by the OVRO observations is also included.

polarization from the total intensity can not be explained with the same geometry as IRAS 4A, since it is the red-shifted side that lacks polarized emission. The magnetic field direction implied by the observations is parallel to the circumbinary disk, which means the magnetic field and the axis of rotation are perpendicular in the plane of the sky. The non-alignment of the two outflows powered by IRAS 16293 suggests significant field structure within the circumbinary disk if the field is along each outflow.

A toroidal field in a roughly edge-on disk would result in a magnetic field direction parallel to the major axis. Rotation of the circumbinary disk which surrounds IRAS 16293 could drag the field lines along, producing a toroidal component. At the position of each binary component, the field may be tangled in the accretion disk. Therefore, the observed polarized emission might represent the largest column density through the disk where the toroidal field dominates. However, this suggestion is highly speculative as coupling of the field to the material in the disk and magnetic reconnection should be taken into account. The models of core collapse in the presence of a magnetic field (Galli and Shu, 1993; Fiedler and Mouschovias, 1993) have not included rotation.

Theoretical constraints on the magnetic field structure in binary systems are lacking. While the collapse of molecular cores into binary systems have been theoretically modeled (see review by Bodenheimer et al. 1993), these studies have not included the effects of the magnetic field. The magnetic field geometry in a binary system will almost certainly be more complicated than that of a single star. While IRAS 4A is also a binary, the envelope appears to be common to both sources, and thus the binary nature of the source was used only to justify the inner radius of the envelope. However, the dust continuum emission from IRAS 16293 originates from two resolved components. Higher resolution and better signal to noise data are necessary to place further constraints on the magnetic field structure of IRAS 16293.

6.1.4 Orion IRc2

No polarized emission was detected in the observations toward Orion IRc2, which includes emission from the high mass young stellar object (source I) but is dominated by emission from the hot core. Maps of the polarized emission were made with both natural and uniform weighting and with tapers in the *uv* plane to eliminate the longest baselines. Natural weighting generally provides the best sensitivity to faint sources; however, the combination of high sidelobes (due to the nearly equatorial declination of the source) and north-south structure in the source caused the naturally weighted maps to have similar noise to the uniformly weighted maps. The continuum emission observed toward IRc2 with a resolution of 2.″7 by 2.″0 (uniform weighting) is presented in Figure 6.9. The location of source I and BN are marked by the asterisk and the triangle respectively. The main source of emission in the map is the hot core. The elongation of hot core emission in a NE-SW direction and a clump to the northwest agree with the 3 mm map of Wright et al. (1992). The peak intensity in the map is 310 mJy beam^{-1} and the integrated intensity in the hot core is 1.1 Jy. The measured rms noise in the Q and U maps for this weighting was 3.8 mJy beam^{-1}. An upper limit from the noise (3σ) of the polarized flux is 3.6% of the peak flux or 1.0% of the integrated flux. While there will be some contribution from free-free emission on large scales, the 100 GHz emission on arcsec scales is dominated by thermal dust emission (Wright et al., 1992).

To investigate the effect of decorrelation by phase noise, models were made which included phase noise at a level expected for the real observations. The atmospheric phase contribution was estimated by using the average phase from the 12 GHz phase monitor at OVRO during the Orion observations. These data were scaled to 105 GHz and for the appropriate baseline lengths using the scaling relations given in Lay (1996). A thermal noise of 60 mJy (rms) was also added to each integration. This thermal noise corresponds to a single sideband system temperature of 400 K in a one minute integration. The thermal noise was added to the real and imaginary components

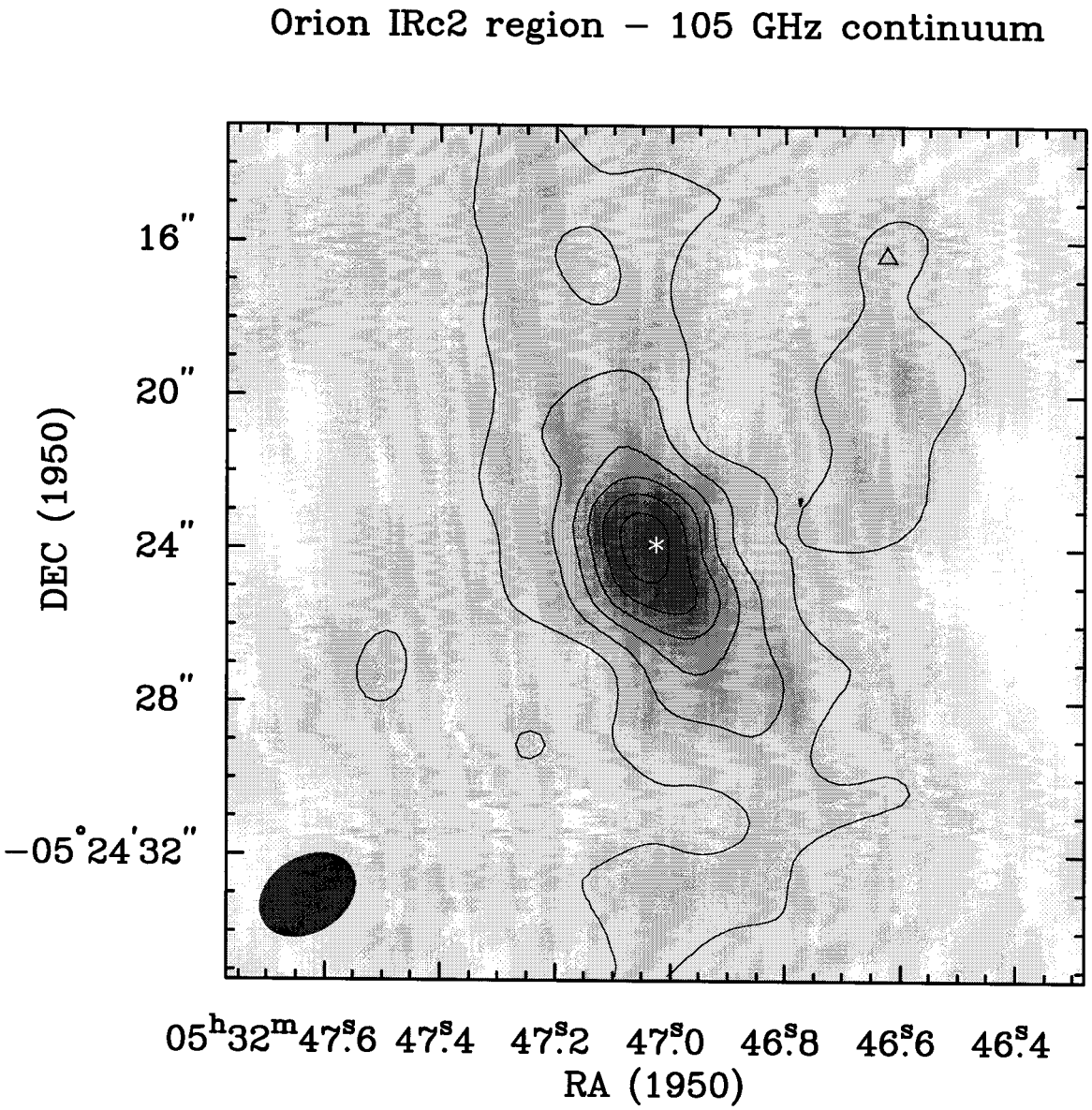

Figure 6.9: The 105.6 GHz continuum image for Orion IRc2. The map was made with uniform weighting (beam 2.″7 by 2.″0). The asterisk marks the location of source I/SiO masers and the triangle marks the position of BN. The contour levels are 50 mJy/beam.

separately, and the atmospheric phase noise was added only to the phase. Two models were calculated, one in which the polarized emission was a 12 mJy point source at the phase center (roughly 4% of the peak flux) and a second in which the total intensity of each visibility was multiplied by 4%. In the map of the point source model, the peak flux (with natural weighting) was 6 mJy beam^{-1}, which would have been $\sim 2\sigma$ in the real maps. The phase noise has reduced the amplitude by 50%. In the scaled emission model, the polarized signal is evident in maps using either uniform or natural weighting. As the shorter baselines will have less atmospheric phase noise (and therefore less decorrelation), the signal is even stronger in a map in which the longer baselines are given less weight.

The polarized flux from the scaled emission model is shown in Figure 6.10. The *uv* data have been weighted by a Gaussian taper with a FWHM of 45 kilo-lambda, which provides a resolution of $3\farcs1 \times 4\farcs2$. The peak polarization is 11 mJy beam^{-1} and the total polarized emission is 18 mJy. The 4% average polarization has been decorrelated to 2.5%. These models demonstrate that polarization at these levels (3–4%) would have been detected by the observations.

As discussed in Chapter 5, far-infrared and sub-millimeter surveys of the polarization in the Orion molecular cloud show a decreased polarization percentage toward Orion IRc2 (Leach et al., 1991; Schleuning et al., 1996) (Figure 5.4). If this effect was due entirely to field tangling, the polarization percentage should increase with smaller beam sizes. However, of the observations listed in Table 5.2, the two observations with the smallest beam sizes actually have a lower percentage polarization. If the polarization is due to a large scale component in the dust that is diluted by the flux from the hot core, then the polarized flux rather than the polarization percentage should be roughly constant near IRc2. However, the observations of Schleuning et al. (1996) show the peak of the polarized flux is located south of Orion IRc2.

The lack of polarization toward IRc2 can not be easily explained by a lack of magnetic fields. Zeeman splitting observations of HI lines over a $5'$ ($\sim$0.5 pc) area in the Orion molecular cloud revealed field strengths of 40 to 100 μG (Troland, 1990).

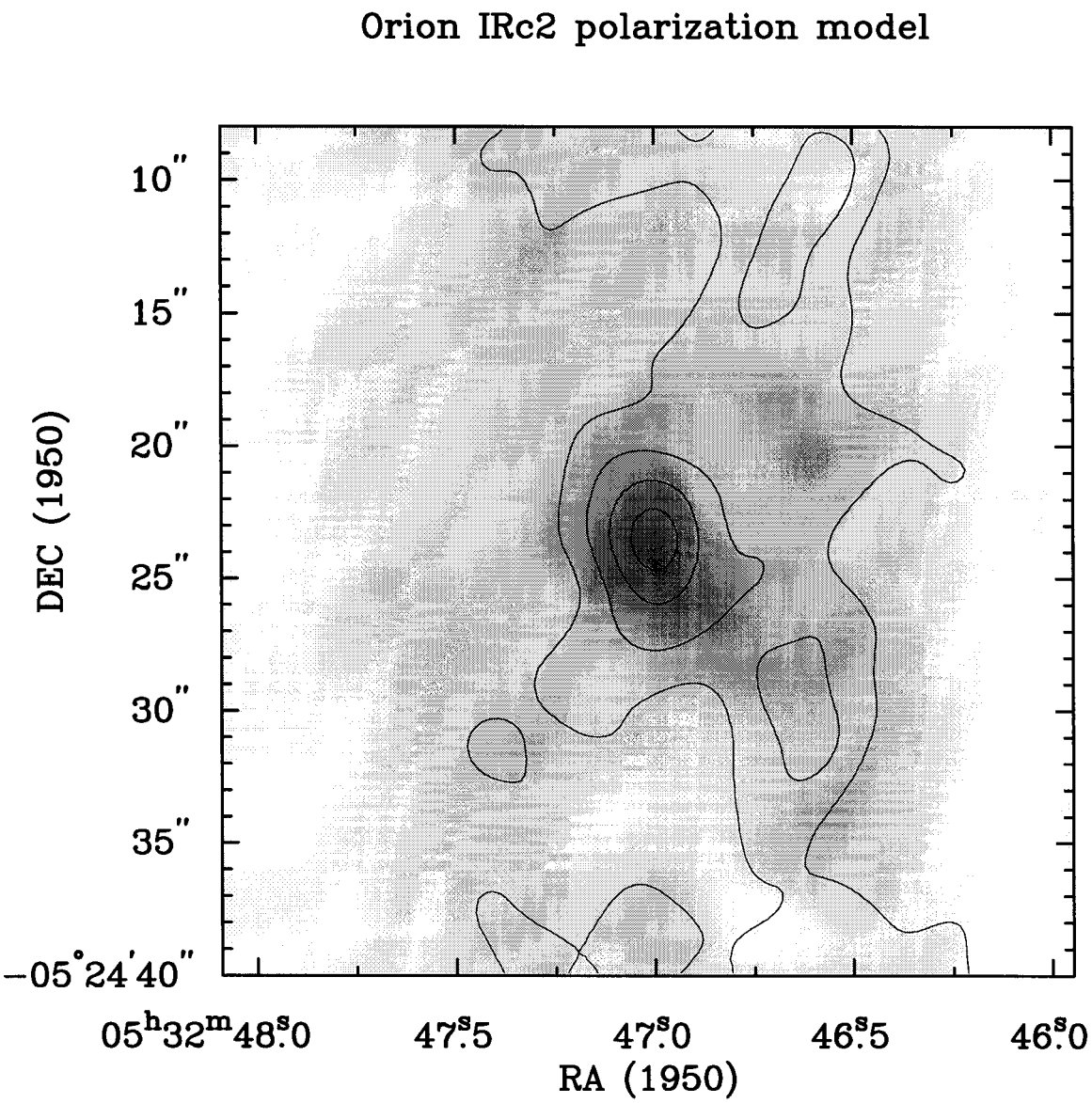

Figure 6.10: The model polarization for Orion IRc2. The polarization emission (contours) was taken to be 4% of the total intensity (grey scale) and the phase noise has been taken into account. The peak total intensity is 420 mJy beam^{-1} and the peak polarized emission is 11 mJy beam^{-1}. The contour levels are 2.5 mJy beam^{-1}. The map was made using a 45 kλ taper.

Both the OH and SiO maser emission are polarized (Figure 6.11). The magnetic field strength in the OH masing region ($\sim$10″ from source I) was estimated by Johnston et al. (1989) to be a few mG.

The magnetic field direction in this region can be estimated using the energetic bipolar outflow. The outflow direction toward source I can be estimated from the Plambeck et al. (1990) observations of the SiO masers. In their model the ring of masers is has a 45° inclination. If the magnetic field direction is parallel to the outflow, the polarized emission is only reduced by $\sqrt{2}$ from the value for the magnetic field direction in the plane of the sky. The lack of polarized emission is probably not due to a field direction parallel to the line of sight. A proposed explanation for the decrease in polarization percentage is discussed in the next section.

6.2 Implications for grain alignment

The original alignment process by paramagnetic relaxation as proposed by Davis and Greenstein (1951) is unable to explain dust grain alignment in the ISM without magnetic field strengths an order of magnitude larger than those observed. Proposed solutions to this difficulty are suprathermal rotation and superparamagnetic grains (§ 2.4). Evidence for and against these theories can be found in observational results.

Goodman et al. (1995) found that the polarization percentage in dark clouds did not scale with increasing extinction as predicted by alignment from paramagnetic extinction. They suggested that grains inside dark, dense clouds were less aligned than those on the edges. However, far-infrared and sub-millimeter observations of warm, dense clouds demonstrate that grains can be aligned in regions with column densities that would be optically thick in selective extinction observations (Hildebrand and Dragovan, 1995).

Alignment by paramagnetic relaxation of thermally rotating grains requires the dust temperature to be lower than the gas kinetic temperature. In the dark clouds observed by Goodman et al. (1995) the gas and grain temperatures are nearly equal

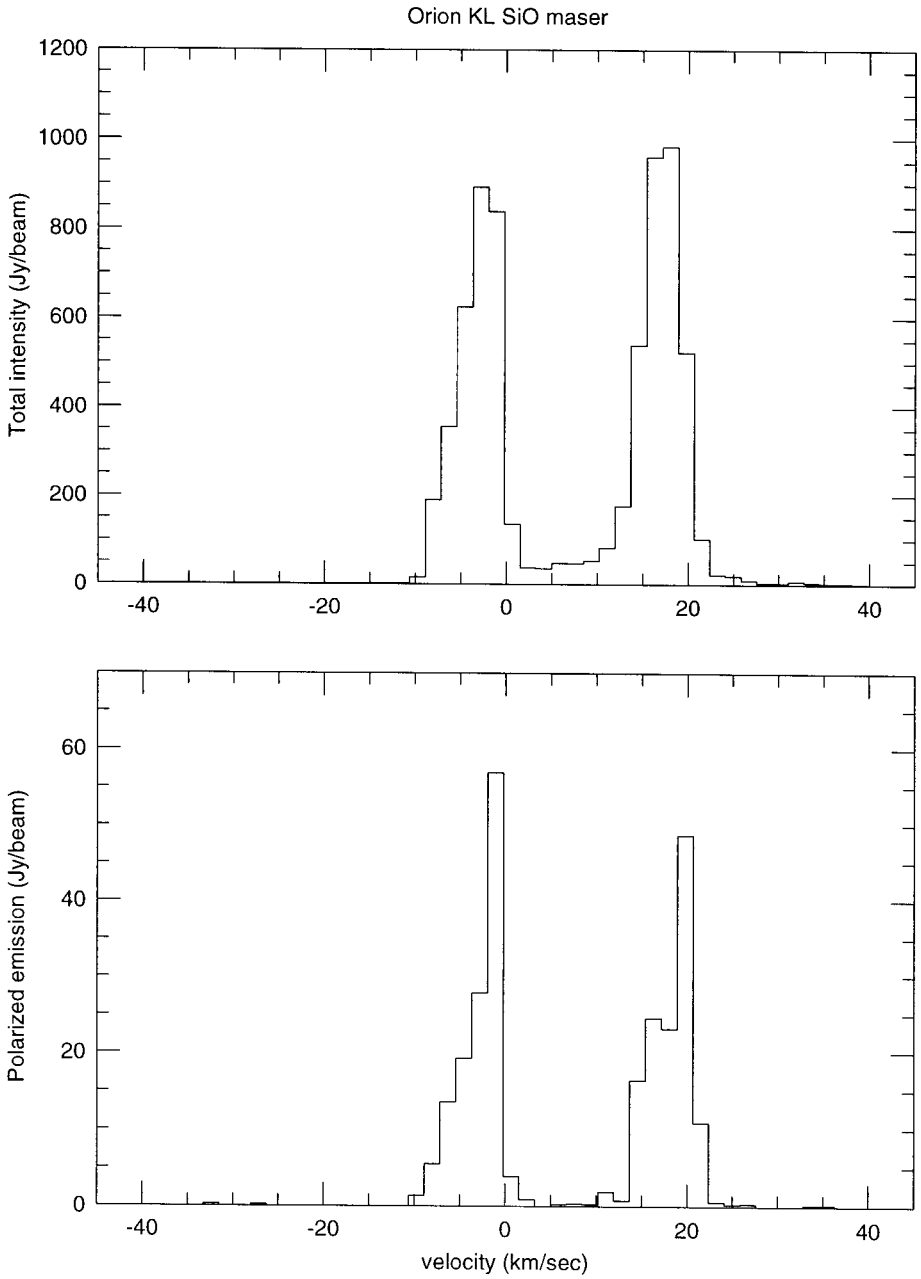

Figure 6.11: The total intensity (top) and polarized flux (bottom) of the 86 GHz SiO maser emission from Orion KL as observed at OVRO. The spectra have been Hanning smoothed. The fractional polarization ranges up to 14%.

(Lazarian et al., 1996). Calculations by Roberge (1996) require gas temperatures an order of magnitude higher than the dust temperature to reproduce the observed polarization percentages. The emission of radiation by dust grains is an efficient cooling process compared to line emission from gas. Thus, the grains can be cooler than the gas if they are not thermally coupled by collisions. This coupling occurs at densities greater than 10^4 cm^{-3} (Mathis et al., 1983). Thus, while the dust temperature may be significantly lower than the gas temperature in the diffuse ISM, this will not be true in dense cores.

There is observational support for superparamagnetism in aligned grains. Mathis (1986) found that large grains are more likely to be aligned than small grains. The size distribution of aligned grains versus the distribution of all grains was estimated by fitting the wavelength at which the maximum polarization (as measured from selective extinction) occurs. This is contrary to the prediction of paramagnetic alignment, in which small grains are easier to align. As Mathis suggested, if only the grains with superparamagnetic inclusions are aligned, then large grains are more likely to have an inclusion and are thus more likely to be aligned. However, superparamagnetic inclusions are not sufficient to produce alignment if the grain and gas temperatures are roughly equal.

Suprathermal rotation through preferential sites for H_2 formation may not work in dense environments. The ratio of atomic to molecular hydrogen density is proportional to the inverse of the total density (Spitzer, 1978), and will be low in dense cores. If the abundance of atomic hydrogen is less than 10^{-3}, the angular velocity of the grain due to H_2 formation is the same as the thermal angular velocity (Lazarian, 1995). Mantle formation in dense regions will decrease the lifetime of preferential H_2 formation sites on the grain and inhibit suprathermal rotation. Thus, suprathermal rotation through H_2 formation will not occur in dense cores and alignment of grains by paramagnetic relaxation is not efficient. This agrees with the conclusion of Goodman et al. (1995) that the grains in dark, dense cores are not well aligned.

6.2.1 Constraints from millimeter observations

My interferometric observations of IRAS 4A and IRAS 16293 have demonstrated that grains are still aligned at densities greater than 10^8 cm^{-3} in warm cores. For alignment by paramagnetic relaxation, the grain temperature must be less than the gas temperature. Sandell et al. (1991) measured the spectral energy distribution of IRAS 4A and derived an effective temperature of 37 K, which should apply to the dust. Blake et al. (1995) derived a gas kinetic temperature in the core of IRAS 4A of 20–40 K from observations of several molecular line species. For IRAS 16293, the dust temperature derived by Walker et al. (Walker et al., 1988) was 32 K, while the molecular line observations indicate the gas kinetic temperature is ~40 K (van Dishoeck et al., 1995). These measurements suggest that the dust and gas temperatures in the envelopes of IRAS 4A and IRAS 16293 are very similar, and thus efficient alignment by paramagnetic relaxation seems unlikely.

The alignment in the dense material surrounding IRAS 4A and IRAS 16293 can be explained if the grains are rotating suprathermally. However, spin-up by H_2 formation may not occur in dense gas as discussed above. Recently, alternate methods for suprathermal rotation of grains have been proposed. Purcell and Spitzer (1971) first proposed angular momentum transfer from cosmic rays to dust and Sorrell (1995) has proposed ejection of H_2 molecules from cosmic ray strikes as a spin-up mechanism. Draine and Weingartner (1996) have shown that an anisotropic radiation field can provide suprathermal rotation if the grain has an irregular shape. This rotation can be much longer lived than spin-up by H_2 formation as it depends on the global properties of the grains rather than the lifetime of individual H_2 formation sites. They also find that the angular velocity exceeds that predicted for H_2 formation. Possible support for this mechanism comes from their prediction that these radiative torques are not efficient for small grains (as the grain must be larger than the radiation wavelength) coupled with observational data which show that large grains tend to be better aligned (Mathis, 1986). Draine and Weingartner (1996) calculated the rotation of grains by

this mechanism in the M17 region using the temperature of the dust (45 K) to estimate the incident energy density. They concluded that grains larger than 0.2 μm would be suprathermally rotating under these conditions. As the dust temperatures in the low mass cores I observed are 30-40 K, the radiative flux produced by the protostar and the disk/star boundary may be sufficient to drive suprathermal rotation in the regions which are not opaque to optical and higher energy photons, but may not be effective at the distance from the central object at which millimeter polarization is observed. While this rotation mechanism will work in star formation regions which produce significant radiation fields, there will be no alignment in cold, dense cores, as seen in the observations of Goodman et al. (1995).

I have also considered the efficiency other alignment mechanisms under the conditions present in the dense envelopes observed. Dust grains can become aligned if a velocity difference exists between the gas and the grains. To estimate the magnitude of this effect in the regions observed here, I estimated the ambipolar diffusion time scale (equation [1.9]) and calculated the corresponding drift velocity for the size scale of the observed region. This velocity is 8×10^{-4} km sec^{-1} for IRAS 4A. Models of the collapse of a magnetized molecular core by Ciolek and Mouschovias (1993) calculated drift velocities near 0.05 km sec^{-1} for densities of order 10^{6-7} cm^{-3} and size scales of thousands of AU. The polarization levels calculated by Roberge et al. (1995) become significant ($> 1\%$) only for drift speeds above 0.2 km sec^{-1} even with the magnetic field in the plane of the sky. Anisotropic radiation pressure on the grains can also produce the necessary drift velocities in the dense gas. Using the 40 K blackbody temperature from the SED fit of IRAS 4A (Sandell et al., 1991), the radiation pressure is 2×10^{-8} dynes cm^{-2}, while the gas pressure for $n = 10^8$ cm^{-3} and $T = 40$ K is 5×10^{-7} dynes cm^{-2}. Thus, the isotropic pressure from the gas will dominate, and there will be no significant gas-grain velocity. Neither of these two mechanisms for producing gas-grain drift velocities is effective enough to produce grain alignment in IRAS 4A and IRAS 16293.

The molecular outflows powered by IRAS 4A and IRAS 16293 produce supersonic

gas velocities which could act to align the grains. Blake et al. (1995) observed high velocity wings at 10–15 km sec^{-1} in the CO outflow of IRAS 4A and similar velocities are seen toward IRAS 16293 (Walker et al., 1986). Calculations by Lazarian (1995) demonstrated that grains can be efficiently aligned by supersonic gas flows, but that the direction of alignment with the magnetic field depended on the grain shape (oblate or prolate) and the measure of anisotropy in the velocity flow. While the observed velocities are sufficient to align the grains, the polarization should then be localized to the regions of outflow only. If this mechanism is responsible for the alignment, the polarized emission seen toward IRAS 4A should be directed along the outflow axis rather than elongated perpendicular to it. If the magnetic field and the outflow are aligned, the grains may be pushed along the field lines by the outflow, reducing the velocity difference between the gas and the grains and the alignment efficiency.

While my observations of the Orion IRc2 region did not detect any polarized emission, the upper limit set (3%) suggests that the 'polarization hole' toward IRc2 is not due to small scale field tangling. The explanation for the low percentage polarization may simply be that the dust grains in the hot core are not aligned. The emission from the hot core arises from a very different range of temperature and density than the emission from gas several arcmin away. The hot core gas has a high kinetic temperature, $T \sim 200$K and density, $n > 10^6$ cm^{-3}, while the extended ridge has a temperature $T \sim 50$K and density $n \sim 10^5$ cm^{-3} (Blake et al., 1987).

The densities sampled by the far-infrared and sub-millimeter observations are high enough that the grain and gas temperatures are probably well coupled and paramagnetic relaxation of thermally rotating grains is unlikely to be efficient. However, the high UV flux due to the recent high mass star formation in this region may provide mechanisms for suprathermal rotation, either through H_2 formation or radiative spin-up. This may explain the high levels of polarization percentage observed in the extended ridge and farther from source I.

The hot core is subjected to extreme conditions, with $T_{gas} > 200$ K and a 10^5 $L_\odot$ source less than 1000 AU away (projected distance). This dust may be quite different

from the grains in cooler, dense regions. These effects could include more spherical grains from higher collision rates and different grain chemistry in the high kinetic temperatures. The high grain temperatures may prevent alignment of the largest moment of inertia with the axis of rotation if the grains are not suprathermally rotating. The high grain temperatures also mean that any spin-up process must be more efficient in order to increase the grain rotation to levels higher than the thermal rotation rate. I suggest that grains are not well aligned under these conditions, leading to a decrease in the polarized emission toward IRc2.

In conclusion, alignment by paramagnetic relaxation of thermally rotating grains is ruled out for the dense envelopes of IRAS 4A and IRAS 16293. Alignment by anisotropic flows (radiation or ambipolar diffusion) also seem unable to fit the data. Of the mechanisms discussed, magnetic alignment of suprathermally rotating grains may be the most plausible. Whatever mechanism is responsible, it must be fairly effective at densities $> 10^8$ cm^{-3} and temperatures of 30–40 K to account for the observed polarized emission.

Chapter 7 Future work

7.1 Observations and modeling

The millimeter polarization observations discussed in Chapter 6 demonstrate the usefulness of this technique for the study of magnetic field structure in star formation regions. Future observational plans include extending OVRO's polarization capabilities to the 1 mm receivers (§ 7.2).

The radiative transfer models calculated for IRAS 4A demonstrate how the polarization data can be used to place constraints on theoretical models of magnetic field structure in collapsing molecular cores and protostellar envelopes. The modeling of polarized emission will be expanded to include a wider range of magnetic field geometries and to be more tightly coupled to the various competing models. High resolution 1 mm data may allow us to distinguish between the magnetic field morphologies predicted by various star formation theories. The models will also be expanded to include the presence of binary components (such as in the case of IRAS 16293). Once theories of binary formation include magnetic fields, models will be calculated from these theories and compared to existing and future data.

We also plan to make observations of linearly polarized molecular line emission (§2.4) toward young stellar objects. As the molecular line emission is often brighter than the continuum emission in protostellar envelopes and disks, this technique may allow observations of the magnetic field structure toward objects which are too weak to detect by continuum polarization with the current receiver sensitivity.

The polarization properties of the OVRO mm-array need to be further characterized. The instrumental polarization on-axis has been measured using quasars and small (almost unresolved) planets, but the off-axis instrumental polarization has not been measured. The off-axis instrumental polarization can be determined by obser-

vations of a polarization calibrator offset in several positions from the field center. A much more precise and efficient method to characterize the off-axis polarization is to use polarization holography with the circularly polarized transmitter described in Chapter 3 as an artificial source. This measurement is crucial for polarization observations of very extended objects.

7.2 Reflecting polarizers at 1 mm

The reflecting polarizers built for the OVRO mm array were installed first for the 3 mm receivers because the system is easier to debug at this frequency: the polarizer tolerances are less stringent, the system temperatures are lower, the atmospheric phase fluctuations are smaller and the fluxes of the reference quasars are higher. However, for the protostellar sources discussed in this thesis, observations at 1 mm are desirable because the dust continuum opacity rises as ν^{β}, where $\beta = 0-2$ and the higher resolution provides measurements of the magnetic field on smaller scales. With the current maximum baseline lengths at OVRO of 200 meters, the maximum 1 mm resolution corresponds to $\sim$150 AU in nearby molecular clouds (Taurus, Ophiuchus). The increased sensitivity will allow observations of a larger number of sources such that the applicability of current theoretical models to a range young stellar object masses and ages can be tested.

The 1 mm polarizers (which are mechanically identical to the 3 mm ones) have been fabricated and assembled. As described in Chapter 3, a method for calibrating the polarizers in the lab is being developed. The 1 mm polarizers will be installed on the telescopes once this calibration has taken place. The current timetable for this is August, 1996, with installation on the telescopes in late August/early September. Testing and observations with these polarizers can begin in Fall, 1996.

7.3 Improving the sensitivity

Improved sensitivity in the polarization images is vital for improving our ability to study the magnetic field structure. This improvement can be realized by increasing the receiver sensitivity. As receiver noise temperatures decrease toward the quantum noise limit (see review by Carlstrom and Zmuidzinas, 1996), further gains can often be best achieved by dual polarization or sideband separation receivers.

7.3.1 Dual polarization receivers

The most efficient method of polarization observing is to receive two orthogonal polarizations simultaneously. Cross-correlating the four combinations of two polarizations completely describes the polarized emission, both circular and linear. By adding another channel, dual polarization receivers have $\sqrt{2}$ times the sensitivity of single polarization receivers. At millimeter wavelengths, the simplest dual polarization receiver consists of two linearly polarized receivers, with a wire grid polarizer to diplex the signal into the two channels. If observations of linear polarization are desired, the receiver linear polarizations can be converted to circular polarizations on the sky with a quarter-wave plate, such as the reflecting polarizers installed at OVRO.

Dual polarization receivers have been constructed for millimeter wavelengths and used for single-dish observations. For example, the MILLIPOL polarimeter was built for the NRAO 12 meter telescope (Clemens et al., 1990). The two channels are linearly polarized and both signals are passed through a half-wave plate which is rotated to reduce systematic errors. The instrumental polarization of this system was measured to be 0.2%.

7.3.2 Sideband separation receivers

Millimeter heterodyne receivers are generally double sideband (DSB) systems, which means they are sensitive to two frequency bands on the sky, referred to as the up-

per and lower sidebands. These two signals must be separated to obtain the single sideband (SSB) response. The undesired sideband can be filtered out before mixing, though this adds noise and is frequency specific. While these filters can be tuned, they have narrow bandwidths. Interferometers can use phase switching to enable signals correlated at each telescope to be separated in the post-receiver processing (generally in the correlator). However, the atmospheric noise is uncorrelated between the telescopes and can not be separated. In a sideband separation receiver the two sidebands (both signal and noise) are separated in the receiver.

The receiver noise temperature is a measure of the sensitivity and is defined as the physical temperature at a specified location that would produce the same power level in a noise-less receiver. A DSB receiver can have a double sideband response (both signal and noise from the two sidebands overlapped) or a single sideband response (signal from only one sideband, but noise from both). For a DSB receiver with balanced sideband gains, the SSB system temperature referred to outside the atmosphere is

$$T_{sys} = 2(T_{atm}(e^{\tau} - 1) + T_{rx}e^{\tau}), \tag{7.1}$$

where $T_{atm} = 295$ K is the temperature of the atmosphere and T_{rx} is the noise temperature of the receiver. For an inherently single sideband system (such as a sideband separation receiver or a filtered DSB receiver), the SSB system temperature is

$$T_{sys} = T_{atm}(e^{\tau} - 1) + 2T_{rx}e^{\tau}, \tag{7.2}$$

where the SSB receiver T_{rx} is the same as for the DSB receiver. For systems in which the atmosphere is the main source of noise, the single sideband receiver sensitivity is increased over a double sideband receiver with balanced sideband gains (Figure 7.1). As the atmosphere becomes the dominant noise component, the single sideband system has twice the sensitivity of the double sideband system and the integration time necessary to achieve the same signal-to-noise is four times less.

A prototype sideband separation receiver design and results were presented by

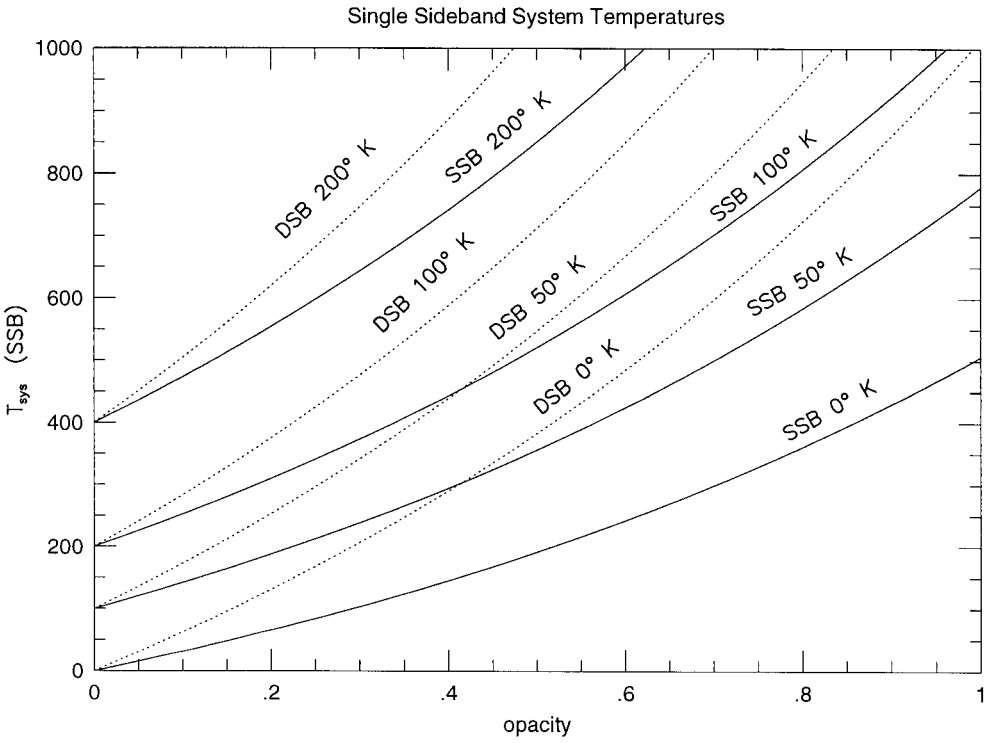

Figure 7.1: The single sideband system temperature referred to outside the atmosphere is shown as a function of atmospheric optical depth and the double (dashed line) and single sideband (solid line) receiver temperatures. The double sideband system has balanced sideband gains and the single sideband system has the same receiver noise temperature as the double sideband system.

Akeson et al. (1993). The prototype used waveguide components for convenience, though they are more lossy than other design methods. As illustrated in Figure 7.2, the incoming sky signal is received by a feedhorn and split by a Magic-'T', which divides the signal from the first port into two equal, in-phase output ports. The output ports also receive half of the power from the fourth port, which is terminated at 4 K. Reflections from the output ports are split between the feedhorn and the 4 K termination, minimizing cross talk between the mixer ports which would contaminate the separation. The local oscillator (LO) signal is injected after the Magic-'T' through two 20 dB cross guide couplers. A variable phase shifter in one of the LO paths introduces a 90° phase shift between the signal and LO at one mixer relative to the other. This causes a 90° phase shift in the downconverted output of one mixer relative to the output of the other mixer. The relative phase shift is in the opposite sense for the two downconverted sidebands.

The two intermediate frequency (IF) signals pass through a quadrature hybrid coupler, which combines signal from one input port with signal from the other input port shifted by 90°. This additional 90° phase shift combined with the 90° shift introduced by the LO, results in phase differences of 0° or ± 180° for the two sidebands in each of the two outputs, as shown by the vectors in Figure 7.2. Therefore, each output of the hybrid coupler consists of signals from only one of the sidebands, up to the level of separation.

To test the separation capability of the receiver, a second oscillator, matched to the input, served as an artificial source. The separation level depends on IF equal pathlengths and signal strengths. Accordingly, adjustable coaxial lines were used to compensate for the difference in IF pathlengths. With the individual amplitudes from the mixers equalized by adjusting the IF amplifiers, the separation exceeded 40 dB at the IF frequency where the signal amplitudes were equal. With the system set for equal signal amplitudes at a mid-IF frequency, the separation across the entire IF passband (500 MHz) was greater than 25 dB, which is limited by variations in the IF amplifier passbands. The separation levels measured would be sufficient to eliminate

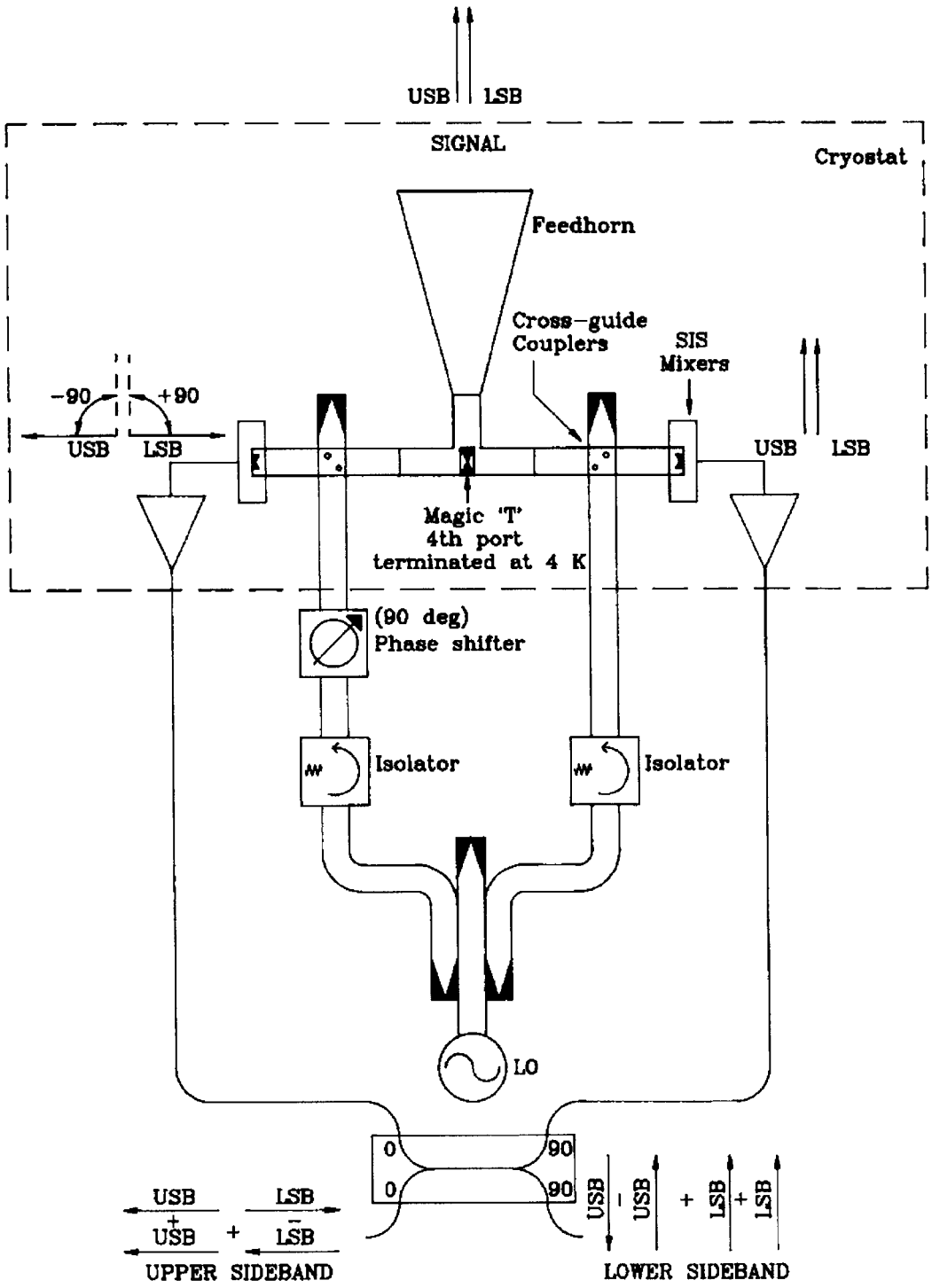

Figure 7.2: A schematic layout for the sideband separation receiver.

the noise from the opposite sideband. However, the lossy waveguide components make this design impractical for use in low noise receivers.

Many of the elements in the sideband separation receiver described above can be placed on one chip, greatly decreasing the losses and simplifying the design. A sideband separation mixer for 200–300 GHz has been designed and is being tested by Kerr and Pan (1996). The 'ultimate' receiver would have four output ports to accommodate both dual polarization and sideband separation. With a flexible correlator input, the output from this receiver could be either two orthogonal polarization states in two separated sidebands or the DSB response of all four polarization states, which for an interferometer, could then be separated in the correlator.

Chapter 8 Summary

This thesis describes the results of a project utilizing millimeter interferometric polarimetry to investigate the magnetic field structure in protostellar envelopes. Magnetic fields are widely believed to be a critical component in the dynamics of molecular clouds and in the star formation process. Most theories require magnetic fields for the removal of angular momentum and in the formation of energetic outflows. While theoretical models have included the effects of magnetic fields in the collapse of a molecular core to a protostar, observational constraints on appropriate size scales are lacking.

The appropriate methods for observing magnetic fields in molecular clouds include Zeeman splitting and emission or absorption due to magnetically aligned elongated dust grains. Zeeman splitting provides information on the magnetic field strength, but it is difficult to measure this effect in the molecules which trace dense molecular cores. Optical and near-infrared selective extinction observations have been used to determine the structure of the magnetic field over tens of parsecs in the diffuse regions of molecular clouds. However, this method can not probe the extremely dense regions where star formation is currently taking place. These aligned grains emit polarized radiation at far-infrared to millimeter wavelengths. Imaging this emission directly traces the magnetic field structure even in very dense regions. Interferometry is necessary to achieve resolution on the size scales appropriate to protostellar envelopes, disks and outflows.

To enable polarization observations, adjustable reflecting polarizers were constructed and installed on the six telescopes of the Owens Valley Radio Observatory millimeter array. The polarizer consists of a grid of parallel 25 μm gold-plated tungsten wires spaced 125 μm apart placed in front of a flat mirror. The angle of the grid relative to the linear polarization of the receiver and the spacing between the

grid and the reflecting mirror are both adjustable. Thus the linear polarization of the receiver can be converted to any other polarization on the sky. For observations of linearly polarized emission, the polarizers are configured as quarter wave plates and the circular polarizations are cross correlated to produce the four Stokes parameters. As only one polarization can be measured on each antenna, a set of 64 polarization states was constructed to time multiplex between the four polarization states on all baselines. The instrumental polarization is measured with observations of a polarized point source (quasar) or an unpolarized source (Neptune).

Observations were made toward NGC 1333/IRAS 4A, IRAS 16293-2422, Orion KL/IRc2 and L1551-IRS5. Linearly polarized emission was detected in the first two sources. The low mass sources chosen (all sources except Orion) are all highly embedded with dense extended structures surrounding the central source. These massive structures may correspond to the magnetically supported envelopes predicted by theoretical modeling and make these objects ideal environments in which to probe the magnetic field structure.

Located in the Perseus molecular cloud at a distance of 350 parsec, the NGC 1333 region contains several young stellar objects including IRAS 4A. This object is part of a wide (30″) binary system and powers a well collimated bipolar molecular outflow. The central source has been resolved into a 1.″8 binary at 345 GHz. The peak linear polarization detected is 8.6 ± 1.4 mJy beam^{-1} and is offset to the north of the peak in the total intensity. The magnetic field direction at the peak of the polarized emission is $7° \pm 6°$. The range of magnetic field angles in the polarized emission is 4° to 20°. The bipolar outflow is directed roughly north-south near IRAS 4A but bends to nearly 45° far from the central source. Thus, the magnetic field direction implied by the interferometric observations is parallel to the outflow on small scales. The magnetic field direction does not match the direction seen on parsec scales as measured by optical and infrared selective extinction. This suggests substantial structure in the magnetic field between molecular cloud and individual object scales.

By calculating radiative transfer models, I have shown that the offset and elonga-

tion of the polarized emission in IRAS 4A is consistent with an hourglass morphology of the magnetic field and optically thick emission from the envelope. On the red-shifted side of the envelope the field lines are nearly in the plane of the sky, while on the blue-shifted side they are inclined towards the line of sight. Thus, more polarized emission is observed from the red-shifted side. While the limited polarization data is insufficient to determine exact model parameters, an inclination of 50° from the plane of the sky and a peak optical depth near unity reproduce several features of the data. The offset of the linearly polarized emission from the total intensity is mainly determined by the inner radius of the envelope, which was set by the binary separation. The elongation of the polarized emission perpendicular to the magnetic field axis was also reproduced in the model and is an intrinsic feature of the hourglass magnetic field morphology used.

The young stellar object IRAS 16293 is in the Ophiuchus molecular cloud at a distance of 160 parsec. The source is a binary with a 5″ separation. Both components are surrounded by several $M_\odot$ of circumbinary material. The polarized emission is 6.2 ± 1.6 mJy beam^{-1} and the peak is located between the two binary components but closer to 1629B (the brighter of the two at 3 mm). The magnetic field direction at the peak of the polarized emission is $134° \pm 7°$. This angle is parallel to the position angle of the binary. Four separate outflow lobes emanate from IRAS 16293 and it has been suggested that each of the binary components powers a bipolar outflow. The outflow associated with 1629B has a position angle of roughly $-90°$ far from the source, but the red lobe appears to be directed $-45°$ near to the source. This direction is roughly parallel to the small scale magnetic field direction implied in the millimeter data. The magnetic field direction corresponds to a toroidal field in the circumbinary disk. This field configuration could be created if the field was frozen into the matter that collapsed to form the rotating circumbinary disk. Theories of binary star formation incorporating magnetic fields and higher resolution data are necessary to understand the magnetic field structure of IRAS 16293.

While no polarized emission was detected toward Orion KL/IRc2, the limits set

are significant. Far-infrared and submillimeter polarization surveys with beam sizes 20–30″ show that the polarization is as large as 9% at some locations, but decreases toward the position of IRc2, a high mass young stellar object. The millimeter interferometric observations are dominated by emission from the hot core. The upper limit on the linearly polarized emission with 3″ resolution is ∼3%. This implies that the 'polarization hole' observed in the surveys is not due to the field line tangling on scales of ∼1000 AU.

Various mechanisms for the alignment of grains have been discussed. Alignment of grains by paramagnetic relaxation requires the internal temperature of the grains to be significantly lower than the gas kinetic temperature. This condition is unlikely to be met in the dense regions observed in this project. Mechanical alignment by ambipolar diffusion is not efficient enough and a mechanism for suprathermal rotation of warm grains in dense regions may be necessary to explain the observations.

Reflecting polarizers have also been constructed for the 1 mm system at OVRO and will be installed in August, 1996. Observations at 1 mm of young stellar objects are desirable as the dust opacity increases as ν^{0-2} and the maximum resolution at 1 mm (1″) corresponds to ∼150 AU at the distance to the nearest regions of low mass star formation. Future plans also include observations of molecular line polarization. The observations described here demonstrate the power and potential of millimeter interferometric polarimetry in the investigation of the magnetic field structure in the environments of young stellar objects. Increased resolution and sensitivity in the polarization images will provide detailed information on the magnetic field structure and further constrain the theoretical models.

Bibliography

Akeson, R., Carlstrom, J., Phillips, J., and Woody, D., 1996, *Astrophys. J., Lett.* **456**, 45

Akeson, R., Carlstrom, J., Woody, D., Kawamura, J., Kerr, A., Pan, S., and Wan, K., 1993, in B. Hadley (ed.), *Fourth International Symposium on Space Terahertz Technology*, p. 12

Andre, P., Ward-Thompson, D., and Barsony, M., 1993, *Astrophys. J.* **406**, 122

Arquilla, R. and Goldsmith, P., 1986, *Astrophys. J.* **303**, 356

Artymowicz, P. and Lubow, S., 1994, *Astrophys. J.* **421**, 651

Bachiller, R. and Gomez-Gonzalez, J., 1992, *Annual Reviews Astron. Astrophy.* **3**, 257

Bastien, P. and Menard, F., 1988, *Astrophys. J.* **326**, 334

Beckwith, S. V. W. and Sargent, A. I., 1993, in E. Levy and J. Levine (eds.), *Planets and Protostars III*, p. 521

Blake, G., Sandell, G., van Disoeck, E., Grosbeck, T., Mundy, L., and Aspin, C., 1995, *Astrophys. J.* **441**, 689

Blake, G., Sutton, E., Masson, C., and Phillips, T., 1987, *Astrophys. J.* **315**, 621

Butner, H., Evans, N., Harvey, P., Mundy, L., Natta, A., and Randich, M., 1990, *Astrophys. J.* **364**, 164

Carlstrom, J. and Zmuidzinas, J., 1996, in W. Stone (ed.), *Reviews of Radio Science*

Cernis, K., 1990, *Astrophys. Space. Sci.* **166**, 315

Ciolek, G. and Mouschovias, T., 1993, *Astrophys. J.* **418**, 774

Ciolek, G. and Mouschovias, T., 1995, *Astrophys. J.* **454**, 194

Clemens, D., Leach, R., Barvainis, R., and Kane, B., 1990, *Publ. Astron. Soc. Pac.* **102**, 1064

Conway, R. and Kronberg, P., 1969, *Mon. Not. R. Astron. Soc.* **142**, 11

Crutcher, R., Troland, T., Lazareff, B., and Kazes, I., 1996, *Astrophys. J.* **456**, 217

Crutcher, R. M., Troland, T. H., Goodman, A. A., Heiles, C., Kazes, I., and Myers, P. C., 1993, *Astrophys. J.* **407**, 175

Davis, L. and Greenstein, J., 1951, *Astrophys. J.* **114**, 206

Dragovan, M., 1986, *Astrophys. J.* **308**, 270

Draine, B. and Weingartner, J., 1996, *Astrophys. J.* **470**, in press

Estalella, R., Anglada, G., Rodriguez, L., and Garay, G., 1991, *Astrophys. J.* **371**, 626

Fiedler, R. A. and Mouschovias, T., 1993, *Astrophys. J.* **415**, 680

Flett, A. and Murray, A., 1991, *Mon. Not. R. Astron. Soc.* **249**, 4

Galli, D. and Shu, F. H., 1993, *Astrophys. J.* **417**, 220

Genzel, R. and Stutzki, J., 1989, *Annual Reviews Astron. Astrophys.* **27**, 41

Gold, T., 1952, *Mon. Not. R. Astron. Soc.* **112**, 215

Goldreich, P. and Kylafis, N., 1981, *Astrophys. J., Lett.* **243**, 75

Goodman, A., Benson, P., Fuller, G., and Myers, P., 1993, *Astrophys. J.* **406**, 528

Goodman, A. A., Bastien, P., Myers, P. C., and Menard, F., 1990, *Astrophys. J.* **359**, 363

Goodman, A. A. and Whittet, D. C. B., 1995, *Astrophys. J., Lett.* **455**, 181

Greenberg, J., 1978, in J. McDonnell (ed.), *Cosmic Dust*, p. 221

Hall, J., 1949, *Science* **109**, 166

Harwit, M., 1970, *Nature* **226**, 61

Haschick, A., Moran, J., Rodriguez, L., Burke, B., Greenfield, P., and Garcia-Barreto, J., 1980, *Astrophys. J.* **237**, 26

Hasegawa, T. and Herbst, E., 1993, *Mon. Not. R. Astron. Soc.* **263**, 589

Heiles, C., 1986, in D. Hollenbach and H. Thronson (eds.), *Interstellar Processes*, p. 171

Heiles, C., Goodman, A. A., McKee, C. F., and Zweibel, E. G., 1993, in E. Levy and J. Levine (eds.), *Protostars and Planets III*, p. 279

Herbig, G. and Jones, B., 1983, *Astron. J.* **88**, 1040

Hildebrand, R. and Dragovan, M., 1995, *Astrophys. J.* **450**, 663

Hildebrand, R. H., 1983, *Q. J. R. Astron. Soc.* **24**, 267

Hildebrand, R. H., 1988, *Q. J. R. Astron. Soc.* **29**, 327

Hiltner, W., 1949, *Science* **109**, 165

Hogbom, J., 1974, *Astrophys. J., Suppl. Ser.* **15**, 417

Jennings, R., Cameron, D., Cudlip, W., and Hirst, C., 1987, *Mon. Not. R. Astron. Soc.* **226**, 461

Johnston, K., Migenes, V., and Norris, R., 1989, *Astrophys. J.* **341**, 847

Jones, R. and Spitzer, L., 1967, *Astrophys. J.* **147**, 943

Keene, J. and Masson, C., 1990, *Astrophys. J.* **355**, 635

Kerr, A. and Pan, S., 1996, in B. Hadley (ed.), *Seventh International Symposium on Space Terahertz Technology*, p. 1

Konigl, A. and Ruden, S. P., 1993, in E. Levy and J. Levine (eds.), *Planets and Protostars III*, p. 641

Larson, R., 1981, *Mon. Not. R. Astron. Soc.* **194**, 809

Lay, O., 1996, *Astron. Astrophys.* in press

Lay, O., Carlstrom, J., Hills, R., and Phillips, T., 1995, *Astrophys. J., Lett.* **452**, 73

Lay, O., Carlstrom, R. H. J., and Phillips, T., 1994, *Astrophys. J., Lett.* **434**, 75

Lazarian, A., 1995, *Astrophys. J.* **451**, 660

Lazarian, A., Goodman, A., and Myers, P., 1996, *preprint*

Leach, R., Clemens, D., Kane, B., and Barvainis, R., 1991, *Astrophys. J.* **370**, 257

Leahy, P. and Fernini, I., 1989, *VLA Scientific Memorandom No. 161, Correction Schemes for Polarized Intensity*

Leitch-Devlin, M. and Williams, D., 1985, *Mon. Not. R. Astron. Soc.* **213**, 295

Lis, D., Goldsmith, P., Dickman, R., Predmore, C., Omont, A., and Cernicharo, J., 1988, *Astrophys. J.* **328**, 304

Liseau, R., Sandell, G., and Knee, L., 1988, *Astron. Astrophys.* **192**, 153

Loren, R., 1976, *Astrophys. J.* **206**, 466

Martin, P. G., 1995, *Astrophys. J., Lett.* **445**, 63

Mathis, J. S., 1986, *Astrophys. J.* **308**, 281

Mathis, J. S., Mezger, P., and Panagia, N., 1983, *Astron. Astrophys.* **128**, 212

McKee, C. F., 1989, *Astrophys. J.* **345**, 782

McKee, C. F., Zweibel, E. G., Goodman, A. A., and Heiles, C., 1993, in E. Levy and J. Levine (eds.), *Protostars and Planets III*, p. 327

Menten, K. and Reid, M., 1995, *Astrophys. J., Lett.* **445**, 157

Mestel, L. and Spitzer, L., 1956, *Mon. Not. R. Astron. Soc.* **116**, 503

Minchin, N., Sandell, G., and Murray, A., 1995, *Astron. Astrophys.* **293**, 61

Mouschovias, T., 1995, in A. Ferrara, C. McKee, and P. Shapiro (eds.), *The physics of the interstellar medium and intergalactic medium*, p. 184

Mouschovias, T. and Spitzer, L., 1976, *Astrophys. J.* **210**, 326

Mouschovias, T. C., 1976, *Astrophys. J.* **207**, 141

Mundy, L., Wilking, B., and Myers, S., 1986, *Astrophys. J., Lett.* **311**, 75

Mundy, L., Wootten, A., Wilking, B., Blake, G., and Sargent, A., 1992, *Astrophys. J.* **385**, 306

Mundy, L., Wootten, H., and Wilking, B., 1990, *Astrophys. J.* **352**, 159

Myers, P. C., Fuller, G. A., Goodman, A. A., and Benson, P. J., 1991, *Astrophys. J.* **376**, 561

Myers, P. C. and Goodman, A. A., 1988, *Astrophys. J., Lett.* **326**, 27

Novak, G., Gonatas, D., Hildebrand, R., Platt, S., and Dragovan, M., 1989, *Astrophys. J.* **345**, 802

Novak, G., Predmore, C., and Goldsmith, P., 1990, *Astrophys. J.* **355**, 166

Perley, R., Schwab, F., and Bridle, A., 1989, *Synthesis Imaging in Radio Astronomy*, ASP conference series

Plambeck, R., Wright, M., and Carlstrom, J., 1990, *Astrophys. J., Lett.* **348**, 65

Plambeck, R., Wright, M., Mundy, L., and Looney, L., 1995, *Astrophys. J., Lett.* **455**, 189

Prigent, C., Abba, P., and Cheudin, M., 1988, *Inter. Journal of IR and MM Waves* **9**, 477

Purcell, E., 1979, *Astrophys. J.* **214**, 404

Purcell, E. and Spitzer, L., 1971, *Astrophys. J.* **167**, 31

Reid, M., Schneps, M., Moran, J., Gwinn, C., Genzel, R., Downes, D., and Ronnang, B., 1988, *Astrophys. J.* **330**, 809

Roberge, W., 1996, in W. Roberge and D. Whittet (eds.), *Polarimetry of the Interstellar Medium*, p. 401

Roberge, W. G., Hanany, S., and Messinger, D. W., 1995, *Astrophys. J.* **453**, 238

Sandell, G., Aspin, C., Duncan, W., Russell, A., Robson, E., and Hough, J., 1991, *Astrophys. J., Lett.* **376**, 17

Sargent, A., Beckwith, S., Keene, J., and Masson, C., 1988, *Astrophys. J.* **333**, 936

Schleuning, D., Dowell, C., and Platt, S., 1996, in W. Roberge and D. Whittet (eds.), *Polarimetry of the Interstellar Medium*

Scoville, N., Carlstrom, J., Chandler, C., Phillips, J., Scott, S., Tilanus, R., and Wang, Z., 1993, *Publ. Astron. Soc. Pac.* **105**, 1482

Shapiro, J. and Bloemhof, E., 1990, *Inter. Journal of IR and MM Waves* **11**, 973

Shu, F. H., 1977, *Astrophys. J.* **214**, 488

Shu, F. H., Adams, F. C., and Lizano, S., 1987, *Annual Reviews Astron. Astrophy.* **25**, 23

Simmons, J. and Stewart, B., 1985, *Astron. Astrophys.* **142**, 100

Sorrell, W., 1995, *Mon. Not. R. Astron. Soc.* **273**, 169

Spitzer, L., 1978, *Physical Processes in the Interstellar Medium*, John Wiley & Sons

Spitzer, L. and McGlynn, T., 1979, *Astrophys. J.* **231**, 417

Strom, S., Strom, K., and Edwards, S., 1987, in R. Pudritz and M. Fich (eds.), *Galactic and Extragalactic Star Formation*, p. 53

Tamura, M., Hayashi, S., Yamashita, T., Duncan, W., and Hough, J., 1993, *Astrophys. J., Lett.* **404**, 21

Tamura, M., Hough, J., and Hayashi, S., 1995, *Astrophys. J.* **448**, 346

Tamura, M., Yamashita, T., Sato, S., Nagata, T., and Gatley, I., 1988, *Mon. Not. R. Astron. Soc.* **231**, 445

Tereby, S., Shu, F., and Cassen, P., 1984, *Astrophys. J.* **286**, 529

Troland, T. H., 1990, in *IAU symp 140*, Vol. 140, p. 293

Turnshek, D., Turnshek, D., and Craine, E., 1980, *Astron. J.* **85**, 1638

Umebayashi, T. and Nakano, T., 1990, *Mon. Not. R. Astron. Soc.* **243**, 103

van Dishoeck, E., Blake, G., Jansen, D., and Grosbeck, T., 1995, *Astrophys. J.* **447**, 760

Vrba, F., Strom, S., and Strom, K., 1976, *Astron. J.* **81**, 958

Walker, C., Carlstrom, J., and Bieging, J., 1993, *Astrophys. J.* **402**, 655

Walker, C., Carlstrom, J., Bieging, J., Lada, C., and Young, E., 1990, *Astrophys. J.* **364**, 173

Walker, C., Lada, C., Young, E., and Margulis, M., 1986, *Astrophys. J., Lett.* **309**, 47

Walker, C., Lada, C., Young, E., and Margulis, M., 1988, *Astrophys. J.* **332**, 335

Wannier, P., Scoville, N., and Barvainis, R., 1983, *Astrophys. J.* **267**, 126

Weiler, K. and de Pater, I., 1980, *Astron. Astrophys.* **91**, 41

Wickramasinghe, N., 1973, *Light scattering functions for small particles, with applications in astronomy*, John Wiley & Sons

Wootten, A., 1989, *Astrophys. J.* **337**, 858

Wright, M., Sandell, G., Wilner, D., and Plambeck, R., 1992, *Astrophys. J.* **393**, 225

Appendix A MMA polarization data reduction

A.1 Introduction

This manual covers how to reduce polarization data taken at the OVRO mm array. I have assumed that you already know about normal calibration techniques (gain, passband and flux) and are generally familiar with the structure of mma. If not, please read the mma cookbook first (available at http://www.ovro.caltech.edu). The polarization forms are grouped together under **utilities** → **polarization**, except for the plotting, which is under **plot** → **polarization**. The polarization routines are only available in a separate version of mma that is accessed by typing **mmapol** at the unix prompt. This version of mma is exactly the same as the regular version, except all the polarization routines are included. The names of the polarization routines are given in Table 1.

Polarization observations at OVRO are taken with the polarizers set in right and left circular polarization mode. As the telescopes have only one receiver, each baseline measures one cross-correlation per integration. The polarizers are switched between right and left circular to allow observations of all four correlations on all baselines. In this way, all four possible combinations of circular polarization are measured throughout the track, but never simultaneously. Because circular correlations are observed, any circular polarization intrinsic to the source can not be measured very accurately. In fact, most of the data reduction assumes that the source circular polarization is 0 (which is a valid assumption for the millimeter continuum from almost all astronomical sources).

In addition to the normal calibrations, polarization data must be corrected for the

instrumental polarization introduced by the telescopes and polarizers. Instrumental polarization is the amount of the unwanted polarization present (i.e., left circular if the polarizer is set for right circular). The instrumental polarization terms must be measured separately by observing a calibration source. The instrumental polarization terms are then stored in a table to be applied to other sources.

A.2 General procedure

1. Create table
2. Gain and passband calibration
   - set **combine polarization = yes** on gain form
   - set **pol** = % on apply form
3. Flux calibrate (if a planet was observed)
   - select RR/LL in filter when deriving scale factors
4. Unscramble switching cycle
5. Calculate IP terms (if calibration source)
6. Remove instrumental polarization
7. Calculate Stokes parameters (or correct parallactic angle)
8. Write fits file

A.3 Details of polarization routines

2. `Gain and passband calibration.` The gain calibration routine will combine the data from the RR and LL correlations on each baseline if **combine polarization = yes** on the derive gain calibration form. Unless you strongly suspect

that the phase calibrator has significant (at least several percent) circular polarization, you should combine the polarizations. The routine that derives the passband calibration does not check for polarizations, so you must set this in the filter. The easiest way is to go to the **global** form and enter the phrase **where pol in ("rr","ll")** under **filter string**. Remember to remove this restriction when applying the passband correction.

4. `Unscramble switching cycle.` Because only 1 polarization is measured on each telescope, a switching pattern is used during the track. The integrations must be rearranged into groups of 4 (RR,LL,RL,LR). The baseline and time are averaged for each group. The unscrambling routine will work best if all 6 telescopes are present in the track, so do not delete entire telescopes until after this has been run.

   Go to the **decoding** form (under **utilities** → **polarization**). Set the filter and hit **unscramble**. The decoding pattern should be set to **64-state**. After the unscramble routine has been run, all four integrations in each set will have the same **int** number in the database, but different **inh#** indices. You can confirm that **unscramble** has run properly by plotting the continuum data with the polarization plotting routine. Go to **plot** → **polarization**, select **integration** for the **x-axis** and hit **continuum**. The plot is divided into three panels, one for RR and LL together and separate plots for RL and LR. If **unscramble** has run properly, the RR and LL amplitude and phases are plotted on top of each other and in groups of four.

5. `Calculate the instrumental polarization.` Sources appropriate for measuring the instrumental polarization are bright quasars (3C279 is bright and polarized), mostly unresolved planets (Neptune) and linearly polarized maser lines. The best measurements of the instrumental polarization terms are achieved using an unpolarized source (i.e., Neptune). Only the continuum channel can be used to measure the instrumental polarization, so if you are using maser

data, the channels must be added together and placed in the continuum channel. Gain calibrate the track with the polarization calibrator as usual, being especially careful about the phase. The calibrated amplitudes must be flat and the average phase on each baseline for the IP calibrator source should be 0. If necessary, do a second gain calibration using the IP source and low order polynomials. This second gain calibration is almost always necessary for planets. Heavily resolved baselines should be divided by the visibility before using a planet in amplitude calibration.

Go to the instrumental polarization form. Enter the source to be used under **calibrator source**. If you are using a planet, the source polarization can immediately be set to 0. Toggle **set pol** to yes and **L** to 0. Otherwise, leave **set pol** to no. Make sure **interactive** is set to **yes** and hit **derive IP**. You will now see plots of the real and imaginary components for each baseline and each polarization (RR,LL,RL,LR) and the least-squares fit. The RR and LL are fit to a constant and the RL and LR are fit to function of the parallactic angle. Obviously bad points can be flagged by placing the cursor on them and typing **f**. Flagged points are plotted in purple. RR and LL points with real components less than 0 are automatically flagged. At least 16 points in each correlation must be included (not flagged) for the fit to proceed. After all baselines are fit, the IP terms are printed out to the window in which **mmapol** was started and to a file called **cross-pol.out**. For planets, the IP terms can be saved the first time through the program (**save error soln** to **yes**). If using a linearly polarized source the first run through the program is used to find the source linear polarization (which is written to cross-pol.out). Then, toggle **set pol: yes** and enter the fractional source linear polarization under **L:** and the polarization position angle under **phase:**. Change **save error soln** to **yes** and run through the plots again.

The instrumental polarization terms are stored in two tables in the database

that can be accessed with the **dwb** program (data workbench). The table **IPE** contains a list of all stored IP solutions, including the calibrator source, date and frequency. This table can be used to determine which **soln#** to use when correcting for the instrumental polarization (see step 6). The IBL table stores the individual terms, four from each baseline.

6. `Correct the Instrumental Polarization.` The instrumental polarization is removed from the source using its total intensity and the previously measured IP terms. You must specify the source under **calibrator source** or in the filter. The easiest way to specify which IP terms to use is **IP solution: specify soln** or **closest time**. If using **specify solution** enter the solution number and use 0 for the frequency. The smoothing time should be set to 10 to 30 minutes depending on how quickly the total intensity changes on the resolved baselines - shorter smoothing times are necessary for more resolved sources. Now hit **apply corrections**. The plots contain the uncorrected data, corrected data and the IP term for each RL and LR correlation and each baseline. The program will run much faster if the plots are turned off.

7. `Calculate Stokes parameters.` The Stokes parameters (I,Q,U,V) are calculated from the unscrambled circular polarizations. The program replaces the circular correlations in the current table with the calculated Stokes parameters and deletes all unused integrations. You can either copy the data into a new table or replace the data in the current table with the Stokes parameters. If you use **copy table**, the new table becomes your active table and you can hit **Stokes** immediately.

   If you choose to export your data as circular correlations rather than Stokes parameters, you should correct for the parallactic angle term in the RL and LR correlations. Mapping routines in AIPS and DIFMAP expect this correction to have been performed. Go to **utilities** → **polarization** → **parallactic angle**. Set **save new phases** to **yes** and set any filter parameters. The plots display

both old and new phases (remember only the RL and LR phases will change), but the program will run much more quickly without the plotting.

8. `Write FITS file`. Use the same form as for regular tables. All polarizations are written to one FITS file. After the source is selected, all the polarizations present in the track will be listed. You only have to click yes on any one of these and all the polarizations will be written. This FITS file can then be read into AIPS, DIFMAP or any other mapping routine that accepts UV data.

   In the current version of the FITS routine, tables that are combinations of more than one track (union tables) are not handled properly. Thus, tracks should be combined by writing a single FITS file for each track and using the AIPS task DBCON. Also, data written by the polarization version of the FITS routine are not in TB (time-baseline) order. If using DIFMAP, the data must first be sorted in AIPS (task UVSRT).

routine name	purpose
unsf.f	unscramble switching cycle
ipf.f	calculate instrumental polarization terms
cipf.f	correct for instrumental polarization terms
stkf.f	calculate Stokes parameters
wfif.f	write FITS file
parf.f	plot/correct parallactic angle
ppl1f.f	plot continuum polarization data
ppl2f.f	plot spectrometer polarization data

Table A.1: Fortran routine names for mma polarization software.